UNIVERSITY OF CALIFORNIA,
IRVINE

Size-Effect Strengthened Metamaterials: Multi-Scale Modeling and Fabrication Processes

DISSERTATION

submitted in partial satisfaction of the requirements
for the degree of

DOCTOR OF PHILOSOPHY

in Materials Science and Engineering

by

Cameron Mikel Crook

Dissertation Committee:
Professor Lorenzo Valdevit, Chair
Professor Daniel Mumm
Distinguished Professor Diran Apelian

2023

DEDICATION

To

my family and friends

TABLE OF CONTENTS

LIST OF FIGURES

LIST OF TABLES

Page

ACKNOWLEDGEMENTS

I would like to thank Professor Lorenzo Valdevit. Lorenzo, I have truly enjoyed my PhD experience and the opportunity to explore and learn in a multitude of different disciplines. Thank you for your guidance and allowing me to drive my research direction. I'd also like to thank the members of the committee, Professor Daniel Mumm, and Professor Diran Apelian for their co-advisement in the early portions of my graduate career as well as the other members of my qualifying committee Professor Tim Rupert, and Professor Mohammad Javad Abdolhosseini Qomi for their valuable feedback and input on my work.

I also want to thank Dr. Jens Bauer for his mentorship and friendship during his tenure in the lab as well as Dr. Tommaso Baldacchini, Dr. Toshihiro Aoki and Dr. Dima Fishman for their gracious help and insights. I'd like to thank my lab mates Raphael Thiraux and Dr. Anna Guell Izard for the many great coffee break discussions and experimental adventures along the way.

I would like to gracefully acknowledge the economic support from U.S. Army Research Laboratory (contract #W911NF-15-2-0024) via a subcontract from Worcester Polytechnic Institute and the UC Lab Fees Research Program Fellowship (Application ID L21GF3677) which allowed me to perform research in-residence at Lawrence Livermore National Laboratory. Thank you to Dr. Chris Spadaccini, Caitlyn Krikorian, Dr. Kevin Paulsen, Dr. Brian Giera, Dr. Congwang Ye and Dr. Michael Homel for their amazing support and insights and who made my experience at Lawrence Livermore National Laboratory exceptionally interesting and exciting.

I'd also like to thank my wife, Estelle Bonnaire, for her compassion and understanding during my long nights studying and experimenting. Lastly, I'd like to thank all my friends and family who have supported me during this endeavor.

Chapter 2 and Appendices A-E in this dissertation are a reprint of the material as it appears in Crook et al., "Plate-nanolattices at the theoretical limit of stiffness and strength", *Nature communications*, published 2020, used with permission from Springer Nature*s*. The co-authors listed in this publication are Jens Bauer, Anna Guell Izard, Cristine Santos de Oliveira, Juliana Martins de Souza e Silva, Jonathan B. Berger, and Lorenzo Valdevit.

Chapters 3 and 4 were performed under the auspices of the U.S. Department of Energy by Lawrence Livermore National Laboratory under Contract DE-AC52-07NA27344. These chapters were prepared as an account of work sponsored by an agency of the United States government. Neither the United States government nor Lawrence Livermore National Security, LLC, nor any of their employees makes any warranty, expressed or implied, or assumes any legal liability or responsibility for the accuracy, completeness, or usefulness of any information, apparatus, product, or process disclosed, or represents that its use would not infringe privately owned rights. Reference herein to any specific commercial product, process, or service by trade name, trademark, manufacturer, or otherwise does not necessarily constitute or imply its endorsement, recommendation, or favoring by the United States government or Lawrence Livermore National Security, LLC. The views and opinions of authors expressed herein do not necessarily state or reflect those of the United States government or Lawrence Livermore National Security, LLC, and shall not be used for advertising or product endorsement purposes.

VITA

Cameron Mikel Crook

Education:

PhD in Materials Science and Engineering 2023
University of California, Irvine
MS in Materials Science and Engineering 2018
University of California, Irvine
BS in Robotics and Mechanical Engineering 2017
Worcester Polytechnic Institute

Awards:

- UC Lab Fees Research Program Fellowship 2021-2023
- POWDERMET NSF Travel Grant 2019
- WPI Dean's List 2015-2017

Teaching Experience:

University of California, Irvine
- CHEM 206 Laboratory Skills – Teaching Assistant 2019

List of Publications:

Journal Articles:

- **Crook, C.**, Saeidi, A., Mumm, D., and Valdevit, L. "A Holistic Analysis of the Bulk Modulus of Key Amorphous and Crystalline Aluminum Oxide, Hydroxide, and Oxyhydroxide Phase using *Ab Initio* Calculations", *Physical Review Letters*, (Submitted)
- **Crook, C.**, Bauer, J., Izard, A.G., de Oliveira, C.S., e Silva, J.M.S., Berger, J.B. and Valdevit, L. "Plate-Nanolattices at the Theoretical Limit of Stiffness and Strength", *Nature Communications*, 2020
- Bauer, J., Kraus, J.A., **Crook, C.**, Rimoli, J.J. and Valdevit, L. "Tensegrity Metamaterials: Towards Failure Resistant Engineering Systems through Deformation Delocalization", *Advanced Materials*, 2020
- Bauer, J., **Crook C.**, Izard, A.G., Eckel, Z.C., Ruvalcaba, N., Schaedler, T.A. and Valdevit, L. "Additive Manufacturing of Ductile, Ultrastrong Polymer-Derived Nanoceramics", *Matter*, 2019
- Izard, A.G., Bauer, J., **Crook C.** and Valdevit, L. "Ultrahigh Energy Absorption Multifunctional Spinodal Nanoarchitectures", *Small*, 2019
- Lienhard J., **Crook, C.**, Zahiri Azar, M., Hassani, M., Mumm, D.R., Veysset, D., Apelian, D., Nelson, K.A., Champagne V., Nardi, A., Schuh C.A., and Valdevit, L. "Surface Oxide and Hydroxide Effects on Aluminum Microparticle Impact Bonding", *Acta Materialia*, 2020
- Kazantseva, A.V., Chernykh, E.A., **Crook, C.**, Garcia, E.P., Fishman, D.A., Potma, E.O., Valdevit, L., Kharintsev, S.S., Baldacchini, T. "Nanoscale investigation of two-photon polymerized microstructures with tip-enhanced Raman spectroscopy", *Journal of Physics: Photonics*, 2021

List of Presentations

Oral Presentations:

- *Modeling Size-Effects in Closed-Cell Brittle Foams Under Large Deformations.* 13th US National MPM Workshop, September 2022, Austin, TX.
- *Unraveling the Roles of Thickness, Crystallinity and Composition of Powder Passivation Layers in Cold Spray of Aluminum.* TMS February 2022, Anaheim, CA.

- *Characterization of Oxide Layer in Aluminum Powders for Cold Spray.* Cold Spray Action Team (CSAT), June 2018, Worcester, MA.
- *Closed Cell Structures at the Hashin-Shtrikman Upper Bound.* Materials Research Society (MRS) Fall Conference, November 2018, Boston, MA.
- *Investigation of Compositional and Structural Evolution of Passive Passivation Layers to Absorbed Water on Cold Spray Aluminum Powders.* POWDERMET, June 2019, Phoenix, AZ.
- *Additively Manufactured Plate-Based Ceramic Nanoarchitected Materials.* American Society of Mechanical Engineers (ASME) International Design Engineering Technical Conferences (IDETC), August 2019, Anaheim, CA.
- *Closed-Cell Nanoarchitectures at the Theoretical Limit of Stiffness and Strength.* American Society of Mechanical Engineers (ASME) International Mechanical Engineering Congress & Exposition (IMECE), November 2019, Salt Lake City, UT.

ABSTRACT OF THE DISSERTATION

Size-Effect Strengthened Metamaterials: Multi-Scale Modeling and Fabrication Processes

By

Cameron Mikel Crook

Doctor of Philosophy in Materials Science and Engineering

University of California, Irvine, 2023

Professor Lorenzo Valdevit, Chair

While the exploitation of size effects on the mechanical performance of nanoarchitected materials is a well-established design paradigm, to date practical implementations have been limited to very selective topologies, material systems, processing techniques and size regimes. Widespread adoption of this approach will require substantial progress in topology optimization, multi-scale modeling and scalable nanomanufacturing. This thesis advances the field of optimal design of size-effect strengthened materials by developing three novel capabilities.

Firstly, two-photon polymerization direct laser writing (TPP-DLW) and pyrolysis were used to fabricate plate-nanolattices for the first time. While architected materials are typically fabricated as polymeric structures via TPP-DLW, we found the viscoelastic properties of the polymer interfered with accurate comparisons against the upper bounds on stiffness and strength for an isotropic voided material. Thus, the polymeric structures were converted to pyrolytic carbon with strong linear elastic behavior for which the plate-lattice topology was confirmed to achieve the bounds in both stiffness and strength. Moreover, the combination of an optimal plate-lattice topology with size-effect strengthened pyrolytic carbon resulted in the highest specific strength architected material ever reported (at the time of publishing).

Although the plate-nanolattices possessed exceptional mechanical properties, there is no suitable additive manufacturing process capable of fabricating larger material volumes for practical use. By contrast, syntactic foams, i.e., closed-cell foams composed of hollow particles that form spherical nonoverlapping

voids, are amenable to self-assembly and may have comparable specific strengths and stiffnesses to state-of-the-art plate-nanolattices if fabricated with a ceramic constituent material and hollow microparticles. Unfortunately, there is no current scalable process to produce highly controlled hollow particles in the quantity, dispersity and sizes required to fabricate these foams. Therefore, a process to fabricate hollow template-free ceramic particles is introduced here to enable future self-assembled size-effect strengthened syntactic ceramic foams, wherein the hollow ceramic particles become the porogen allowing exceptional control over the final pore size distribution. In addition to demonstrating tunability of the particle size and wall thickness, the process also included special considerations for scalability and extensibility to other material systems.

Lastly, a multi-scale computational procedure is developed to model the mechanical response and progressive failure mechanisms of size-effect strengthened ceramic syntactic foams, which may be produced in a scalable fashion using the particle porogens introduced previously. The computational approach includes a novel flaw field which may be generated for arbitrary porosity, and an accompanying material model which accounts for Weibull variability in the strength of brittle ceramics as well as increases in strength arising from reductions in the characteristic dimensions of geometric features. This model is developed in the framework of the material point method, constituting the first demonstration of a simulation incorporating large deformation, contact and fracture mechanics to investigate the strength and failure mechanisms of syntactic foams under uniaxial tension and compression.

This thesis lays the groundwork for the design and scalable fabrication of size-effect strengthened materials for real-world applications requiring extreme strength and minimal weight. While the focus of this work is on ceramics, many of the results are general and applicable to nanoarchitected materials made of any constituent in which size-effects and topology influence strength.

1. Introduction

Metamaterials, i.e., materials engineered to exhibit properties unavailable in monolithic systems, have been the focus of immense study in the past two decades, as a platform to combine otherwise mutually exclusive properties. Metamaterials combine the properties of a constituent material with those of specialized architectures to form an effective material which is superior to its individual parts. Hence, they are also termed architected materials, and their applications span from electromagnetics to acoustics, heat transfer, and structural systems. Notable examples include optical cloaks with negative refractive indexes[1], thermoelectric devices with high electrical conductivity and low thermal conductivity[2], negative Poisson's ratio materials[3], zero or negative thermal expansion coefficient materials[4], recoverable energy absorbent materials[5] and size-effect strengthened materials[6]. The focus of this work is on the last category, a special subset of structural metamaterials that exhibit increased strength from exploitation of small-scale features. While an optimal architecture is key to maximizing the properties of size-effect strengthened materials, the enhancement in strength crucially relies on manipulating the defects and mechanisms of failure in the constituent material.

Despite the ubiquity of polymers, their use as structural materials is often limited by their susceptibility to creep, especially at elevated temperatures. Thus, most structural applications use metals and ceramics. Orowan[7] and Frenkel[8] estimated the theoretical cleavage and shear strengths, respectively, for a hypothetical crystalline material. Orowan initially considered the cleavage strength as the maximal stress to separate two planes of atoms with spacing a_0 as shown in Figure 1.1a, where the stress, σ, as a function of displacement is dictated by the strength and stiffness of the atomic bonds. This function is approximated by a sinusoidal function as:

$$\sigma = K \sin\left(\frac{2\pi}{2d}(a - a_0)\right) \tag{1.1}$$

where K is the initially unknown stress constant, a is the displacement and $2d$ is the period. Differentiating Equation (1.1) and solving for K at $a = a_0$ yields:

$$K = \frac{Ed}{\pi a_0} \tag{1.2}$$

By equating the energy associated with cleaving the two planes of atoms and the formation of two new surfaces with surface energy γ, the theoretical strength of cleavage can be expressed as:

$$\sigma_{max} = \sqrt{\frac{E\gamma}{a_0}} \tag{1.3}$$

Similarly, the theoretical shear strength to plastically, or permanently, deform two atomic rows (see Figure 1.1b) is computed by assuming a sinusoidal function of shear stress as:

$$\tau = \tau_{max} \sin\left(\frac{2\pi}{b} x\right) \tag{1.4}$$

where b is the interparticle spacing within a row of atoms and τ_{max} is the maximum shear stress. For small displacements, we can apply Hooke's law, defined as:

$$\tau = G\gamma = \frac{Gx}{a_0} \tag{1.5}$$

where G is the shear modulus and γ is the shear strain. Combining Equations (1.4) and (1.5), applying the small angle approximation and assuming a_0 and b are close to unity, the theoretical shear strength is obtained as:

$$\tau_{max} = \frac{G}{2\pi} \tag{1.6}$$

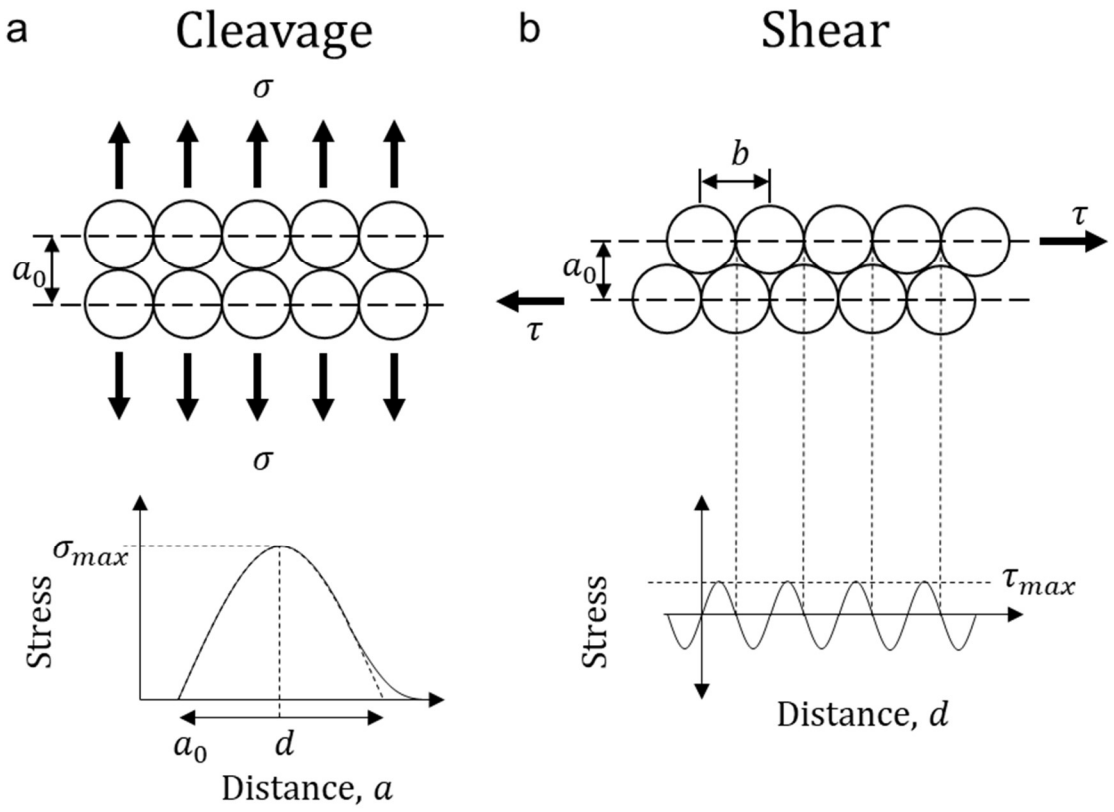

Figure 1.1. *Schematic of failure in a crystal by cleavage (a) and shear (b).*

In practice, these bounds are often further simplified as $E/30 - E/10$, where E is the Young's modulus of the material[9].

Although we observe that metals exhibit ductile failure from plastic yielding, the observed experimental strengths are far below the theoretical shear strength. In single crystalline metals, like the original

description of sliding atomic planes, plastic work is confined to slip planes or crystallographic planes of atoms in which plastic deformation is localized. This is clearly seen in the indentation of single crystal metal micropillars (see Figure 1.2). Any crystal will contain multiple slip planes specific to its symmetry, each with a critical resolved shear stress for which plastic deformation will occur when exceeded.

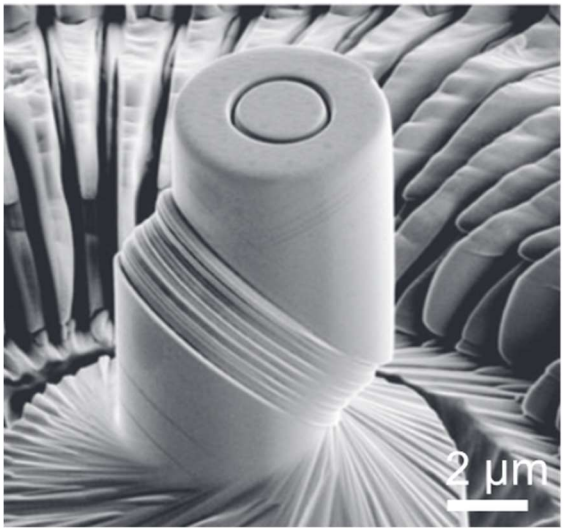

Figure 1.2. *Characteristic slip along crystallographic planes of a single crystal Ni micropillar*[10].

In macroscopic materials, this phenomenon is less obvious because most are polycrystalline, composed of many individual crystals called grains, which are misoriented with respect to one another. Nonetheless, slip occurs by progressive movement of linear defects (i.e., missing rows of atoms) called dislocations along these slip planes, at stresses well below the theoretical strength. In contrast, dislocation motion in ceramics is nearly impossible due to the ionic and covalent nature of bonds, except at high temperatures where diffusion is significant. This is also responsible for the asymmetric tensile/compressive strength of ceramics, where failure commonly originates when intrinsic cracks introduced during processing propagate. As such, ceramics tend to fail in a brittle manner. According to linear elastic fracture mechanics (LEFM), the relation between the size of the largest crack, d_c, and fracture strength, σ_f, at which a crack will propagate is given in Griffith theory[11] by:

$$\sigma_f = \frac{K_{IC}}{Y\sqrt{\pi d_c}} \tag{1.7}$$

where K_{IC} is the intrinsic fracture toughness of the material and Y is a nondimensional parameter related to the geometry of the specimen. As d_c decreases, the stress required to propagate the crack increases, until the stress reaches the theoretical strength of the material.

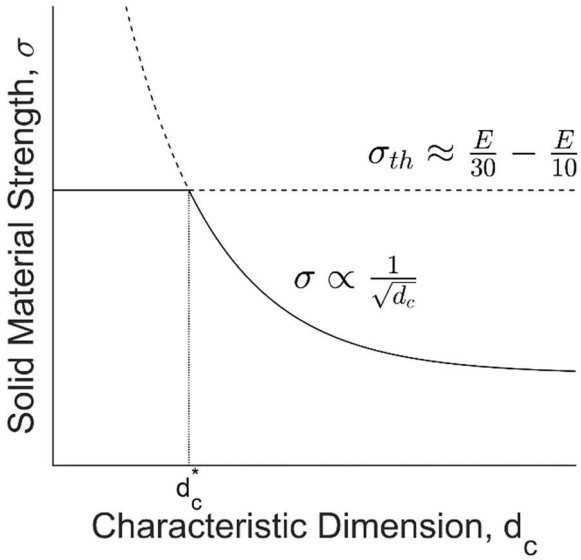

Figure 1.3. *Size effect in brittle ceramic material with maximum flaw size, d_c, and theoretical strength σ_{th}.*

In most situations, the component (or sample) size is much larger than the size of the largest flaw contained therein, which is determined by the fabrication process and is generally a fairly weak function of sample size. However, if the size of the component (or sample) is reduced to a dimension comparable to the largest flaw size, further sample size reduction will inevitably reduce the flaw size as well. The result is a scenario where the sample strength increases proportionally to $1/\sqrt{d}$, a very strong size effect, as shown in Figure 1.3. This constitutes the "smaller is stronger" paradigm, whereby a reduction in defect populations from reduced sample dimensions grants small scale structures much higher strength than their bulk

counterparts. Recent efforts have attempted to capitalize on this phenomenon by architecting materials with topological features below d_c^*, demonstrating metamaterials with enhanced ductility[12], extended elastic limits, and strengths rivaling state-of-the-art engineering alloys[13]. A strength-density property chart, or Ashby chart, is shown Figure 1.4a, where the highest compressive strengths are obtained in metamaterials with the smallest architectural features.

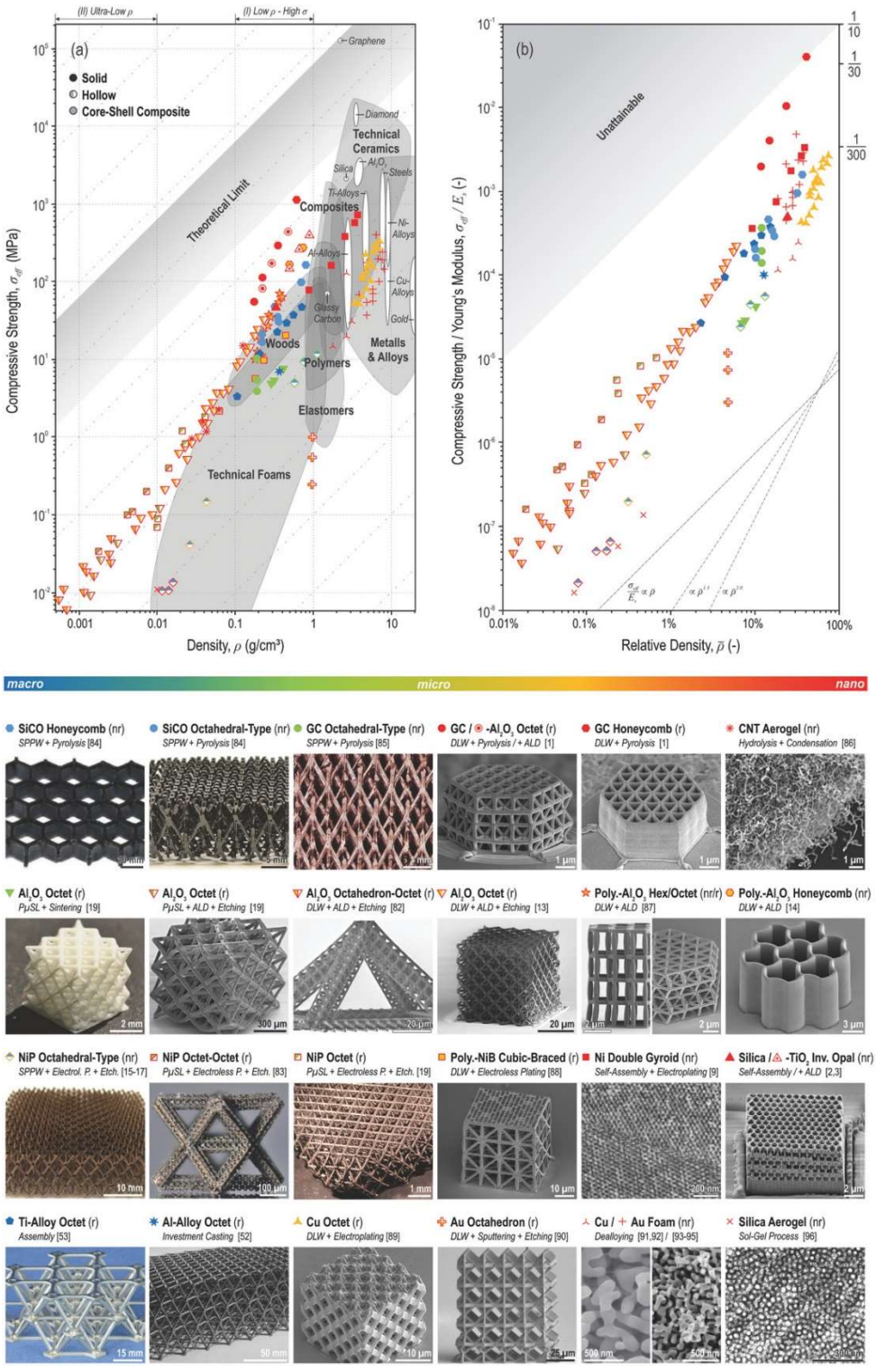

Figure 1.4. *Compressive strength–density materials property chart of different nano-, micro-, and macrolattices as well as stochastic nanoporous and commercial bulk materials copied from Bauer et al.[13]. Lattices with the smallest feature sizes (colored red) have the highest compressive strengths.*

Combining a small-scale architecture with low relative density, e.g., the solid volume fraction, allows nano-architected materials to obtain specific strengths that are unachievable in even the most advanced engineering alloys. Notable examples of these types of metamaterials include pyrolytic carbon nanolattices[6,14], NiP hierarchical octet trusses[15], alumina octet trusses[16], nickel double gyroids[17], silica-titania inverse opals[18,19], and gold foams[20–22]. However, all these demonstrations are of suboptimal architectures with significant knockdowns to stiffness and strength, leaving a notable opportunity for significant improvement in mechanical properties, even for the same constituent materials. At low relative densities, the mechanical properties, generally stiffness and strength, are well characterized by the relation $\bar{P} = C\bar{\rho}^n$ where $\bar{P}$, C, $\bar{\rho}$, and n are the relative mechanical property (i.e., normalized by the value of the solid constituent material), a scalar knockdown factor, the relative density and the scaling exponent, respectively[23]. The parameters C and n depend on the voided topology. In general, there is a strong correlation between the stiffness and strength of an architecture, i.e., stiffer structures are also typically stronger. However, the strength is dictated by the failure mechanism, e.g., plastic or elastic bulking, plastic yielding, or fracture which depend on the topology, aspect ratio of structural features, interconnectivity, and constituent material.

Typical stochastic foams, both open and closed-cell, tend to exhibit bending-dominated behavior, whereby ligaments locally bend upon application of external loads, resulting in inferior properties. Open cell foams, though among the lightest producible structures, are extremely compliant due to their stochastic slender ligaments which undergo bending during deformation, resulting in $n \approx 2$[24]. In particular, the triangular cross sections of ligaments have low bending stiffness and result in a significant knockdown to strength and stiffness. Closed-cell foams offer only modest improvements, since material still predominantly lies along cell edges and entrapped gas does not contribute to significant stiffening. Furthermore, impingement of adjacent pore boundaries leads to distortion of spherical pores into bending susceptible polyhedral cells.

In contrast, two of the most well-known periodic architectures, the octet[25] and isotropic[26] trusses, exhibit stretching-dominated behavior, i.e. their members undergo primarily uniaxial tension or compression upon external loading, resulting in $n \approx 1$. Unfortunately, even neglecting nodal knockdowns on stiffness, truss lattices are theoretically incapable of reaching the isotropic Hashin-Shtrikman (HS) upper bound[27] on stiffness, defined as:

$$\frac{E_{HSU}}{E_s} = \frac{2\bar{\rho}(5\nu - 7)}{13\bar{\rho} + 12\nu - 2\bar{\rho}\nu - 15\bar{\rho}\nu^2 + 15\nu^2 - 27} \tag{1.8}$$

In Chapter 2, we demonstrate the efficacy of a combined size-effect strengthened material and a new optimal plate-lattice topology. Cubic+octet plate-nanolattices are fabricated by two-photon polymerization direct laser writing (TPP-DLW) and subsequently pyrolyzed to pyrolytic carbon. Special fabrication considerations were applied to ensure isotropic linear elastic constituent material properties such that the plate-lattice topology was confirmed to reach the Hashin-Shtrikman and Suquet upper bounds for stiffness and strength of an isotropic voided material, respectively. At the time of publishing, these lattices constituted the highest specific strength architected material. However, the imperfection sensitivity to warping and pre-buckling of plate features was associated with a knockdown factor which led to the convergence of low-density properties with traditional truss-based lattices. Moreover, the fabrication process is not amenable to scale-up.

Ideally, a size-effect strengthened metamaterial would possess a topology which is readily manufactured at scale. At present, no additive manufacturing process is capable of producing large material volumes with features below 1 μm, where the size-effect is most visible for many important ceramic materials[28,29]. Therefore, a self-assembled topology which minimizes knockdowns in strength is needed. Recently, syntactic foams, i.e., foams assembled from hollow particles, also called cenospheres, in a matrix, have drawn interest because the hollow particles allow fine control over the final relative density, pore size

and dispersity (see Figure 1.5). This makes them amenable to scalable manufacturing while minimizing strength penalties.

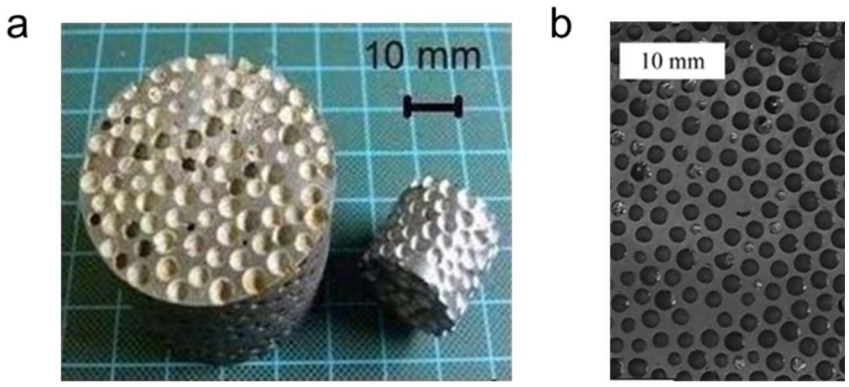

Figure 1.5. *Examples of metallic syntactic foams made by melt infiltration[30] (a) and powder metallurgy[31] (b).*

At present, syntactic foams are manufacturable either by powder metallurgy, wherein cenospheres are sintered with fully dense powder, or melt casting, i.e., infiltration of a melt into densely packed cenospheres, or casting of a cenosphere-loaded epoxy. In the former two cases, the cenospheres are typically fabricated from a polymer template, coated by either spray drying or sol-gel processing, followed by polymer burn-out; as a result, the spheres are sintered to form hollow particles several hundred microns to a few millimeters in diameter, with wall thicknesses typically about ten percent of the diameter. Mechanical properties are largely dictated by the interface between the cenospheres and the matrix, which arise from differences in processing, microstructure, and/or materials. Furthermore, syntactic foams made by melt casting are prone to inter-cenosphere voids, where the high surface tension of the melt prevents infiltration, limiting the minimum acceptable cenosphere size of melt cast syntactic foams[32]. Likewise, remaining porosity in powder metallurgy syntactic foams also strongly limits mechanical properties[33]. Though epoxy-based syntactic foams utilizing glass microballoons are commercially available, epoxy is a poor structural material due to its compliance, low operating temperatures and creep behavior. While we would reasonably expect the properties of a ceramic syntactic foam made from hollow microparticles and thin walls to have

exceptional mechanical properties, there is presently no process suitable for producing hollow ceramic microparticles of the scale and quantity required. Therefore, a template-free process to fabricate hollow ceramic microparticles is introduced in Chapter 3, involving the creation of a stable sol, i.e., a suspension of colloidal particles, which when combined with suitable secondary chemical agents and dispersed in an emulsion can be gelled via a thermal trigger. During gelation, a physical blowing agent forms the internal pore leading to hollow particles with tunable wall thicknesses and size. Although only alumina particles were demonstrated here, a major advantage of this approach is the potential extension to other interesting oxide materials, which might have applications outside of syntactic foams. Most importantly this approach is scalable.

In Chapter 4, computational methods are employed to model the strength of these syntactic ceramic foams and examine the design space associated with pore size and dispersity. First, a thorough review of the literature relating to the strength of alumina ceramics was performed and normalized for variations in testing procedures and statistics. Subsequently, a computational procedure to compute a flaw field describing the characteristic geometric size at any point in an arbitrarily voided domain is developed. Thereafter a framework to capture the stochastic strength and size-effects of brittle ceramic materials is developed and implemented in the material point method, incorporating large deformations, implicit contact, and fracture.

The most notable contributions of this thesis to the field of materials science and engineering are summarized as follows:

(1) For the first time, pyrolytic carbon plate-based nanolattices were fabricated using two-photon polymerization direct laser writing and pyrolysis, experimentally demonstrating that plate-lattices reach the theoretical upper bounds for isotropic stiffness and strength and recording the highest specific strength architected material as of publication of the article.

(2) A template-free sol-gel emulsion evaporation process was developed to fabricate hollow alumina microparticles with tunable wall thickness. This process encompasses the preparation of a stable sol capable of being dispersed into an emulsion whose droplets are transformable into hollow particles by means of

thermally triggered sol gelation and vaporization of a physical blowing agent that forms a hollow internal core. These particles have direct application relevance as the porogens required to fabricate size-effect strengthened syntactic foams.

(3) For the first time, a model was developed to computationally investigate brittle ceramic foams subject to size-effect strengthening (covering 7 orders of magnitude in ligament size), which incorporated the material point method to capture large deformations, contact, and fracture.

2. Plate-Nanolattices at the Theoretical Limit of Stiffness and Strength

2.1. Abstract

Though beam-based lattices have dominated mechanical metamaterials for the past two decades, low structural efficiency limits their performance to fractions of the Hashin-Shtrikman and Suquet upper bounds, i.e., the theoretical stiffness and strength limits of any isotropic cellular topology, respectively. While plate-based designs are predicted to reach the upper bounds, experimental verification has remained elusive due to significant manufacturing challenges. Here, we present a new class of nanolattices, constructed from closed-cell plate-architectures. Carbon plate-nanolattices are fabricated via two-photon lithography and pyrolysis and shown to reach the Hashin-Shtrikman and Suquet upper bounds, via *in situ* mechanical compression, nano-computed tomography, and micro-Raman spectroscopy. Demonstrating specific strengths surpassing those of bulk diamond and average performance improvements up to 639% over the best beam-nanolattices, this study provides detailed experimental evidence of plate architectures as a superior mechanical metamaterial topology.

2.2. Introduction

The Hashin-Shtrikman (HS) and Suquet upper bounds represent the theoretical topological stiffness and strength limits of isotropic cellular solids. The effective Young's modulus (E_{HSU}) and yield strength ($\sigma_{y,SU}$) of a material at those theoretical limits are expressible as[13,27,34]:

$$\frac{E_{HSU}}{E_s} = \frac{2\bar{\rho}(5\nu - 7)}{13\bar{\rho} + 12\nu - 2\bar{\rho}\nu - 15\bar{\rho}\nu^2 + 15\nu^2 - 27} \tag{2.1}$$

$$\frac{\sigma_{y,SU}}{\sigma_{y,s}} = \frac{2\bar{\rho}}{\sqrt{4 + \frac{11}{3}(1 - \bar{\rho})}} \tag{2.2}$$

where E_s, $\sigma_{y,s}$ and ν represent the Young's modulus, yield strength and Poisson's ratio of the constituent material, respectively, and $\bar{\rho}$ is the relative density of the cellular material, i.e., the volume fraction of the solid constituent.

Over the past decade, nanolattices[13,35,36] successfully utilized ultra-strong constituent materials which approach the theoretical material strength limit; however, lattice topologies were largely limited to inefficient beam-geometries. Mechanical size effects enable nanostructures, including pyrolytic carbon octet lattices[6], nickel double gyroids[17], silica inverse opals[18,37]and gold foams[20–22] to exceed their corresponding monolithic bulk solids in strength[13]; however, their non-optimal open-cell topologies exhibit maximal performances well below the Hashin-Shtrikman and Suquet upper bounds. The discussion on mechanical efficiency of cellular materials has classically focused on the difference between stretching- or bending-dominated behavior (e.g. whether lattice elements predominantly undergo uniaxial tension/compression or bending under macroscopically applied stresses, respectively), with the former being stronger and stiffer[38]. Although octet truss and isotropic truss lattices are stretching-dominated, ideal analytical models, even neglecting their nodal knockdowns, show that their stiffness and strength are limited to half the upper bounds, with the octet truss also being anisotropic[13,25,39]. In practice, stress concentrations at nodes and nodal bending further reduce their actual performance[40], to around 25% and 20% of the HS and Suquet upper bounds, respectively. Moreover, geometric manufacturing imperfections, particularly for complex and thin features, may impose further knockdowns[41]. In fact, no open-cell topology is capable of reaching the stiffness or strength[26,42] upper bounds, and while honeycombs are

mechanically efficient, their response is vastly anisotropic, restricting their use to cores of sandwich structures[43].

Recently, closed-cell architectures, consisting of plates arranged corresponding to the closest packed planes of crystal structures, have computationally been predicted to reach the HS and Suquet upper bounds[42,44,45]; however, their manufacturing complexity has thus far prevented any experimental validation. The simplest such topology is the cubic+octet (CO) plate-lattice, also known as the simple cubic + face centered cubic configuration (SC-FCC), characterized by a cubic-plate unit cell embedded in an octet-plate unit cell. CO plate-lattices in theory reach the HS upper bound approaching 0% relative density and remain within 90% of the bound[42,44] at higher $\bar{\rho}$. For any given loading direction, plate-lattices have higher structural efficiency, i.e. they store strain energy more uniformly between members, and have a higher volume fraction of members favorably oriented in the loading direction, compared to a corresponding beam-lattice[42]. Moreover, the three-dimensional intersections of plates prevent the formation of kinematic mechanisms, thus ensuring the plate-lattice topology is always stretching-dominated, which may not be true in a corresponding beam topology. However, these advantages come at the cost of dramatically increased fabrication complexity. The closed-cell topologies of three-dimensional plate-lattices make most conventional fabrication routes, like assembly techniques[40,43], impractical, and leave additive manufacturing (AM) as the only suitable approach. Nevertheless, removing raw materials enclosed within cells remains challenging. Furthermore, synthesis of a highly voided plate-lattice generally requires printing features both near the resolution and maximum build volume limits. For example, a 10% relative density CO plate-lattice requires wall features over 100 times thinner than the unit cell size, and even in fairly high-$\bar{\rho}$ plate-lattices, thin wall features are susceptible to warping. While the above challenges are a general obstacle to the application of plate-lattices, they especially complicate synthesis approaches at the nanoscale where size effects are exploitable.

In this paper, we demonstrate the first plate-nanolattices. These plate-nanolattices are the only materials to experimentally achieve the Hashin-Shtrikman and Suquet upper bounds for isotropic elastic stiffness and

strength, respectively. We manufactured structures with cubic+octet design from pyrolytic carbon via two-photon-polymerization direct laser writing (TPP-DLW) and subsequent pyrolysis. Several critical fabrication challenges were overcome, including removal of excess raw material pockets, design of printing strategies to ensure homogeneous material properties for plates of different orientations and thicknesses, and management/optimization of shrinkage during pyrolysis. Structures were characterized via micro-Raman spectroscopy, nano-computed tomography (nano-CT) and *in situ* mechanical compression. Approaching the theoretical limits in both the topology and constituent material properties, our plate-nanolattices demonstrate an average stiffness and strength improvement of up to 522% and 639% at a given relative density, respectively, compared to pyrolytic carbon octet-truss[6,14,46] and isotropic truss[14] nanolattices, the most advanced mechanical metamaterials reported to date. Our plate-nanolattices have the highest specific stiffness of any reported architected material and outperform all known bulk materials in compressive strength at their given densities. Reaching specific strengths of 3.75 GPa g^{-1} cm^3, they are the only cellular materials to surpass certain diamond systems[47]. Our study clearly shows a tremendous performance improvement to be gained from plate-based topologies compared to state-of-the-art beam-based designs and provides crucial fabrication insights to enable additive manufacturing of high-performance plate-lattice materials.

2.3. Methods

I. Fabrication

Polymeric plate-nanolattices with 5 x 5 x 5 unit cells were fabricated by two-photon-polymerization direct laser writing (TPP-DLW), with the photoresist IP-DIP (Nanoscribe GmbH) on silicon substrates, using a Photonic Professional GT (Nanoscribe GmbH) DLW system. Vertical cubic walls were composed of six 100 nm hatched lines, printed with a laser average power of 12 mW. Horizontal cubic and octet walls

were composed of single in-plane voxel lines, printed with laser average powers of 15.25 and 16 mW, respectively. Both octet and vertical cubic walls had 50 nm slicing distances. All walls were printed at a scan speed of 5000 μm/s. To accommodate otherwise detrimental shrinkage during pyrolysis, structures were printed on multiline coiled springs attached to the top of 340 nm-hatched and 680 nm-sliced support pillars of aspect ratio 0.85. Pillars were printed at a scan speed of 20000 um/s and an average laser power of 30 mW. Springs were printed at 100 um/s and an average laser power of 7.5 mW. Development was performed in a PGMEA bath for 40 minutes, whereby introduced plate face holes allowed infiltration of the virtually closed-cell structures with the solvent and removal of enclosed excess raw material. A subsequent 20-minute isopropanol (IPA) bath was applied to remove residual PGMEA. The polymeric structures were dried in an Autosamdri 931 critical point dryer (Tousimis Research Corp. Inc.) to avoid collapse of the structures by surface tension during evaporation of the solvent. All structures were subsequently pyrolyzed at 900°C for 1 hour in vacuum[6], with a maximum ramp rate of 3°C/min. During pyrolysis, lattices linearly shrank 78-80%. Separately, individual lattices were printed atop 0.76 mm-diameter tungsten pins and pyrolyzed for imaging by nano-computed tomography. Pillars with 6 μm-diameters and aspect ratios of 3, printed with the same writing parameters of the vertical walls, were fabricated to be representative of the constituent material properties.

II. Mechanical Characterization

Relative densities were determined using Solidworks 2018 (Dassault Systèmes SE) and cubic+octet plate-lattice models, including holes, with the SEM measured dimensions of the diagonally-cross-sectioned polymer calibration structures (Figure A.3c). The relative density is assumed to not change significantly, given consistent and isotropic shrinkage during pyrolysis[6]. Lattice dimensions were optically measured from high-resolution SEM using a FEI Magellan 400XHR (Thermo Fisher Scientific Inc.). All lattices were mechanically tested under uniaxial compression on an Alemnis Nanoindenter (Alemnis AG) equipped with

a 100 μm diamond flat punch tip inside a FEI Quanta 3D FEG (Thermo Fisher Scientific Inc.) dual beam (SEM/FIB), using a constant strain rate of 0.001 s^{-1}. Front-view *in situ* SEM videos were used to correct raw load displacement curves for the compliance of the substrate and support pillars via an in-house digital image correlation (DIC) algorithm. An unload-reload cycle was introduced at strains between 4 and 10%, depending on the relative density of the sample, to ensure suspended structures were fully seated on the support pillar surface while avoiding excessive strain-induced sample damage; subsequently, all structures were loaded to failure. Young's moduli were extracted from the maximal slope of linear elastic regimes of the first unloading segment, and yield strengths were determined from the 0.2% yield offset of the engineering stress-strain plots. The compressive strength was measured from the maximal stress before densification. Constituent material properties were measured from *in situ* pillar compression tests under the same conditions as the plate-nanolattices (Figure B.1).

III. Microstructural Characterization

Raman spectra were acquired from baked polymeric and pyrolyzed carbon structures (Figure A.3a, Figure A.3d, and Figure A.5) using an inVia (Renishaw plc) confocal Raman microscope with a 50x objective, operated at an excitation wavelength of 532 nm, with a laser intensity of 10% and an exposure time of 1s over 20 acquisitions. The degree of conversion (DC) was extrapolated from Raman spectra taken of individual polymeric cubic+octet unit cells, pillars printed under the same conditions as the vertical walls, single-voxel horizontal sheets, and octet plate-nanolattice unit cells. DC values were calculated using

$$DC = 1 - \left(\frac{I_{C=C}/I_{C=O}}{I'_{C=C}/I'_{C=O}} \right) \tag{2.3}$$

with $I_{C=C}$ and $I_{C=O}$ the integrated intensities of carbon-carbon and carbon-oxygen double bond peaks (1635 cm^{-1} and 1730 cm^{-1}, respectively) in the polymerized resin, and $I'_{C=C}$ and $I'_{C=O}$ the integrated intensities of

the same peaks in the unpolymerized resin[48] (Table A.1). The relative degree of graphitization (DG) of pyrolyzed CO plate lattices and pillars was measured via R2 parameter, defined as

$$R2 = \frac{I_{D1}}{I_G + I_{D1} + I_{D2}} \tag{2.4}$$

where I_G (1580 cm^{-1}), I_{D1} (1360 cm^{-1}), and I_{D2} (1620 cm^{-1}) are the integrated intensities of the graphite, first-order defect 1, and first-order defect 2 infrared (IR) bands, respectively, as well as via the half-width-half-maximum (HWHM) of the D1 spectral band[49] (Figure A.5 and Table A.2).

IV. Nano-Computed Tomography (Nano-CT)

Samples were scanned in a Xradia Ultra 810 (Carl Zeiss AG) operating with a rotating chromium anode X-ray source with 5.4 keV beam energy, using the phase-contrast imaging mode where the un-diffracted X-ray beam is phase-shifted by $3\pi/2$ using a gold phase-ring positioned near the back focal plane of the zone plate. A total of 901 projections were obtained over 180°, with exposure time and detector binning depending on the sample and field of view (Table A.3). Using the software XMReconstructor (Carl Zeiss AG), the image reconstruction was performed by a filtered back-projection algorithm, the projections were re-aligned for movement compensation using the adaptable movement compensation (AMC) measurements performed before and after the imaging experiment, and the rotation center was adjusted before obtaining the image stacks datasets. The datasets were processed using the software Avizo v. 9.4.0 (Thermo Fisher Scientific Inc.), being first de-noised using its windowed version of the non-local means filter applied in 3D with a search window of 21 voxels, voxel neighborhood of 5 voxels and 1.0 similarity factor, run once for the large field of view (LFOV) 30% and 40% sample datasets and twice for the high resolution (HRES) 60% sample dataset. The segmentation of the image was performed using the watershed algorithm, using marker seeds selected through contrast thresholding, and outside/inside of the carbon cell

markers selected via the contrast-based tri-dimensional selection propagation using the magic wand tool, given that phase contrast gives similar grey levels for the inside and the outside of the carbon cell. Spurious selections due to streaking or thin walls missing from the selection were manually corrected along the sample using the same magic wand tool. The models were subsequently generated from the resulting binary stack using the generate surface module using constrained smoothing 3, which uses an adapted Gaussian filter to smooth voxel edges without losing thin regions in the process, and this surface was re-meshed using the Avizo re-mesh option with high regularity[50], 100% size and fixed contours. The re-meshed surface was then exported as an STL file.

V. Finite Element Analysis

Models of ideal cubic+octet plate-lattices with and without face holes were constructed in Solidworks 2018 (Dassault Systèmes SE) with SEM-measured wall and hole dimensions of the fabricated polymeric structures. Finite element analysis was performed in ABAQUS (Dassault Systèmes SE) for relative densities of approximately 25%, 30%, 40%, 50% and 60%. Results were determined to be within 1% from a mesh sensitivity study. At mid and low relative densities, computed mechanical properties of shell and solid models do not differ noticeably (Figure C.2). Simulations comparing ideal and imperfect, pre-deformed models as well as eigenmode analyses to calculate buckling strengths were carried out in ANSYS 16.2 (Ansys Inc.) with shell models (shell181) with an element size of 2.5% of the unit cell size. Pre-deformations of imperfect models were applied as a percentage of the vertical wall buckling eigenmode of perfect models with zeroed macroscopic displacement. The degree of deformation was adjusted by fitting the computed and experimentally measured average stiffnesses. In all simulations, constituent material properties were representative of nanoscale pyrolytic carbon, with the average yield strength of 2.5 GPa measured from the pyrolytic carbon micro-pillars, the literature reported 62 GPa[51] Young's modulus and a Poisson's ratio $\nu = 0.17$[52]. An additional set of calculations was performed with $\nu = 0.3$, to facilitate

comparison with literature values[44], and to assess the effects of Poisson's ratio on mechanical performance. All models were subject to periodic boundary conditions in the form of uniform macroscopic strains[44,53].

2.4. Results and Discussion

While manufacturing constraints have limited nanoarchitected materials to open-cell designs, like beam-lattices, we demonstrate fabricability of virtually closed-cell plate-nanolattices with dramatically improved mechanical properties over beam-nanolattices (Figure 2.1 and Appendix A). TPP-DLW and subsequent pyrolysis at 900°C were applied to create pyrolytic carbon plate-nanolattices with cubic+octet design. Relative densities of 25-60% were obtained by scaling the unit cell sizes while maintaining constant wall thicknesses of t_c= 260 nm and t_o= 150 nm of the cubic and octet plates, respectively. The ratio $t_c/t_o = \sqrt{3}$ corresponds to full isotropy at $\bar{\rho}$ = 40%[44], which is the approximate center of our examined $\bar{\rho}$ range. Given constraints on the overall build volume, all plate-nanolattices were printed at the resolution limit of the TPP-DLW process, to achieve the above wall thicknesses and relative density range. This necessitated individual printing strategies for plates of different orientations to ensure octet and horizontal and vertical cubic walls had the desired thicknesses, despite the ellipsoidal voxel shape of TPP-DLW[54] (Figure A.2). Introducing small holes with diameters of 100-160 nm at the center of the plate faces allowed infiltration with a developer and removal of unpolymerized resin after the TPP-DLW step despite the closed-cell topology. Nano-CT scans confirmed that the pyrolytic carbon structures were completely voided and free from residual excess material (Figure A.6, Figure A.7, and Figure A.8). Final pyrolytic carbon structures with $\bar{\rho}$ > 37.5% had near ideal, undistorted topologies. With decreasing $\bar{\rho}$, deformations occurred during pyrolysis and became more prominent at the lowest relative densities. However, nano-CT scans revealed that most deformations were limited to the specimen surfaces.

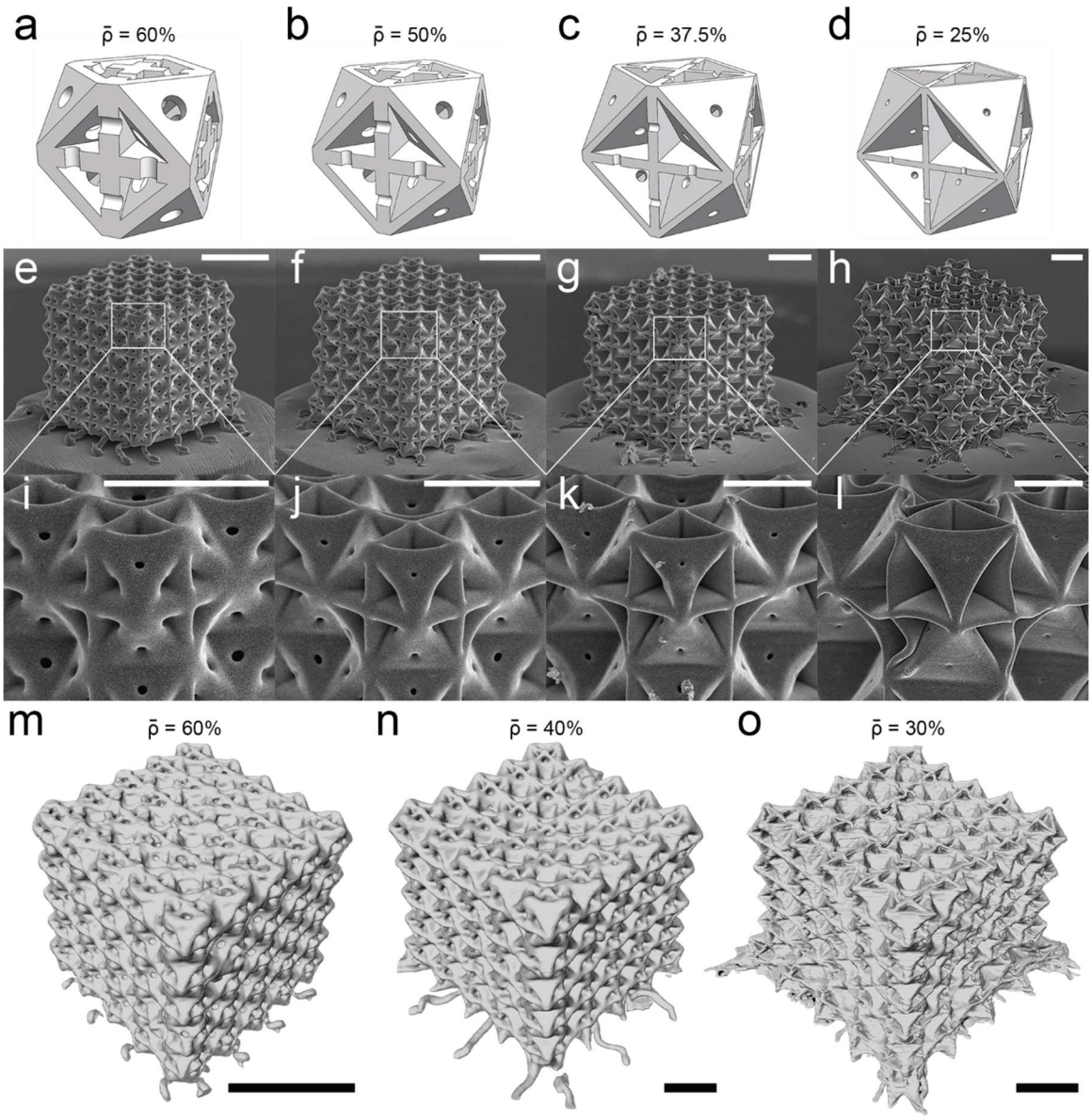

Figure 2.1. *Two-photon polymerization direct laser writing (TPP-DLW) and subsequent pyrolysis creates nearly geometric defect free carbon cubic+octet plate-nanolattices. Optimized TPP-DLW-printing strategies and nanometer-sized face-holes facilitate undistorted, virtually closed-cell plate-nanolattices. Deformations occurring at the lowest relative densities ($\bar{\rho}$) are localized to the surfaces of the structures. Unit cell models (a-b), isometric (e-h) and closeup (i-l) SEM micrographs, and nano-CT scan reconstructions (m-o) for different relative densities. Scale bars are 5 µm (e-h, m-o) and 2 µm (i-l).*

Finite element analysis showed that holes in the plate faces, introduced due to manufacturing constraints, do not significantly reduce the elastic properties of the plate-lattices nor induce any significant

anisotropy (Figure 2). As in the manufactured structures, the hole size was held constant for all modeled relative densities. Although a small performance knockdown emerged at higher $\bar{\rho}$, where the ratio of hole size-to-unit cell size was greatest, the stiffnesses with respect to the ideal models without holes did not fall below 96% and 93% for relative densities of 40 and 60%, respectively. All structures essentially remained isotropic despite the presence of holes, as the Zener anisotropy ratio was approximately 98% for relative densities 25-45% and around 95% at $\bar{\rho}$ = 60%. Additionally, variation of the Poisson's ratio of the constituent material between 0.17 and 0.3 had no significant effect (Figure C.1). In previous work, face holes were also reported not to significantly affect the yield strength of plate-lattices[42]. We numerically showed the same applies to the buckling strength (see Figure C.2).

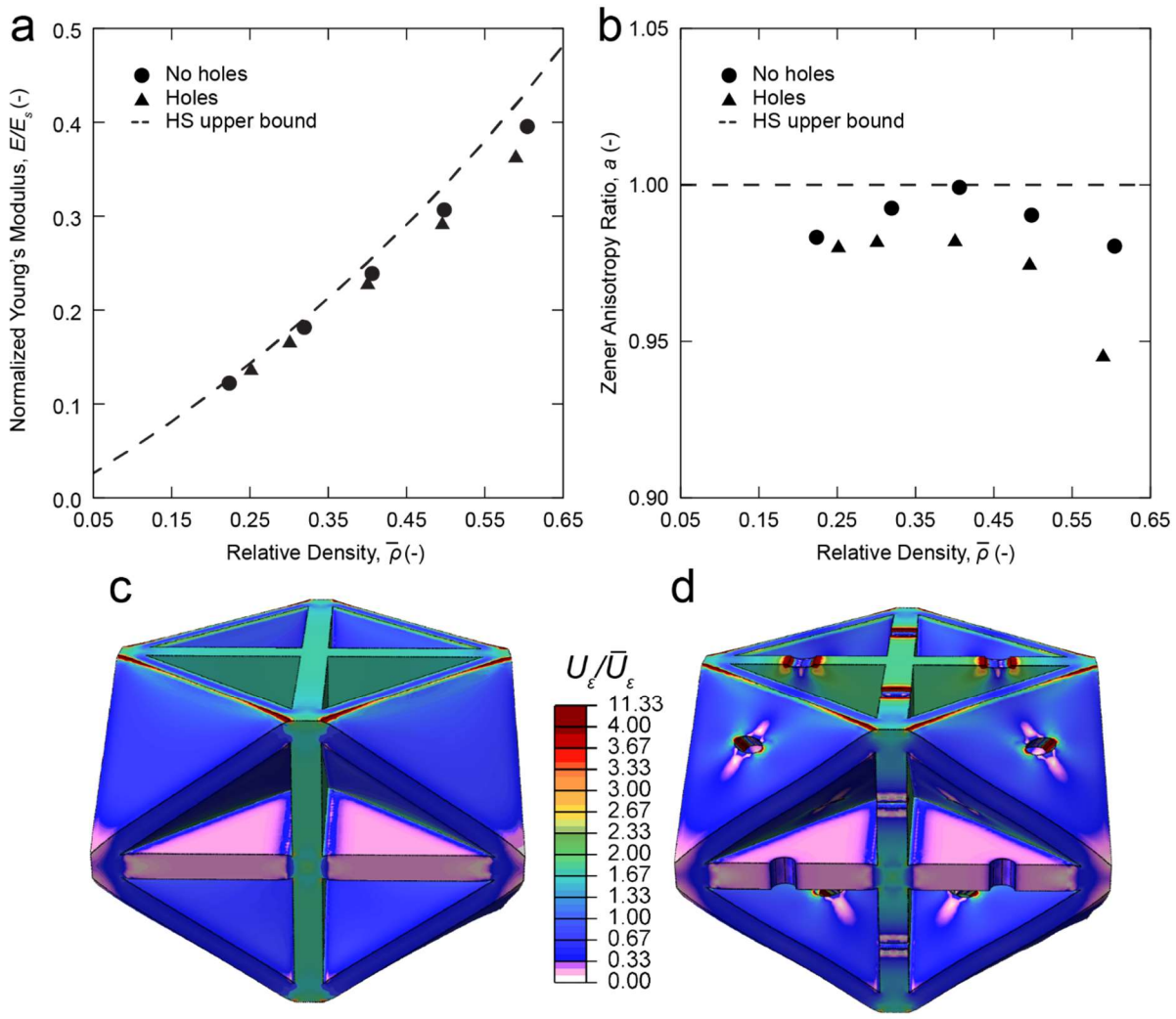

Figure 2.2. *Finite element analyses of cubic+octet plate-lattice performance show that face-holes produce only a minimal knockdown effect and do not contribute strongly to anisotropy. Effective Young's modulus (E) normalized by the constituent material's Young's modulus, E_s (a) and Zener anisotropy ratio, a (b), with and without holes, the dashed lines are the Hashin-Shtrikman (HS) upper bound. Simulated models of 40% relative density (c-d) show that holes do not significantly change the strain energy distribution (U_ε), here normalized by the average strain energy ($\bar{U}_\varepsilon$), while introducing local stress concentrations.*

CO plate-nanolattices with relative densities between 25% and 57.5% were *in situ* mechanically tested under uniaxial compression, using a nanoindentation system equipped with a flat punch tip. Figure 3 shows all recorded compressive stress-strain curves with curves of exemplary relative densities of 57.5%, 50%, 37.5%, and 25%. Nonlinear behavior at small strains is attributed to slight misalignment between the

structures and the indenter. A loading-unloading cycle between 4 and 10% strain was used to ensure accurate stiffness measurement, with the specimens fully seated on their supporting structures. At high relative densities, we found elastic-plastic behavior with effective stiffnesses up to 21.6 GPa, followed by brittle fracture at stresses as high as 3 GPa. Yield strains remained constant at ~5%, while failure strains, predominantly elastic, gradually decreased with decreasing relative density (Figure B.2). Near $\bar{\rho}$ = 37.5%, the deformation behavior transitioned to a more progressive failure (Figure 3c-d) and stiffness and strength gradually decreased to approximately 5.9 GPa and 0.5 GPa respectively, at $\bar{\rho}$ = 25%.

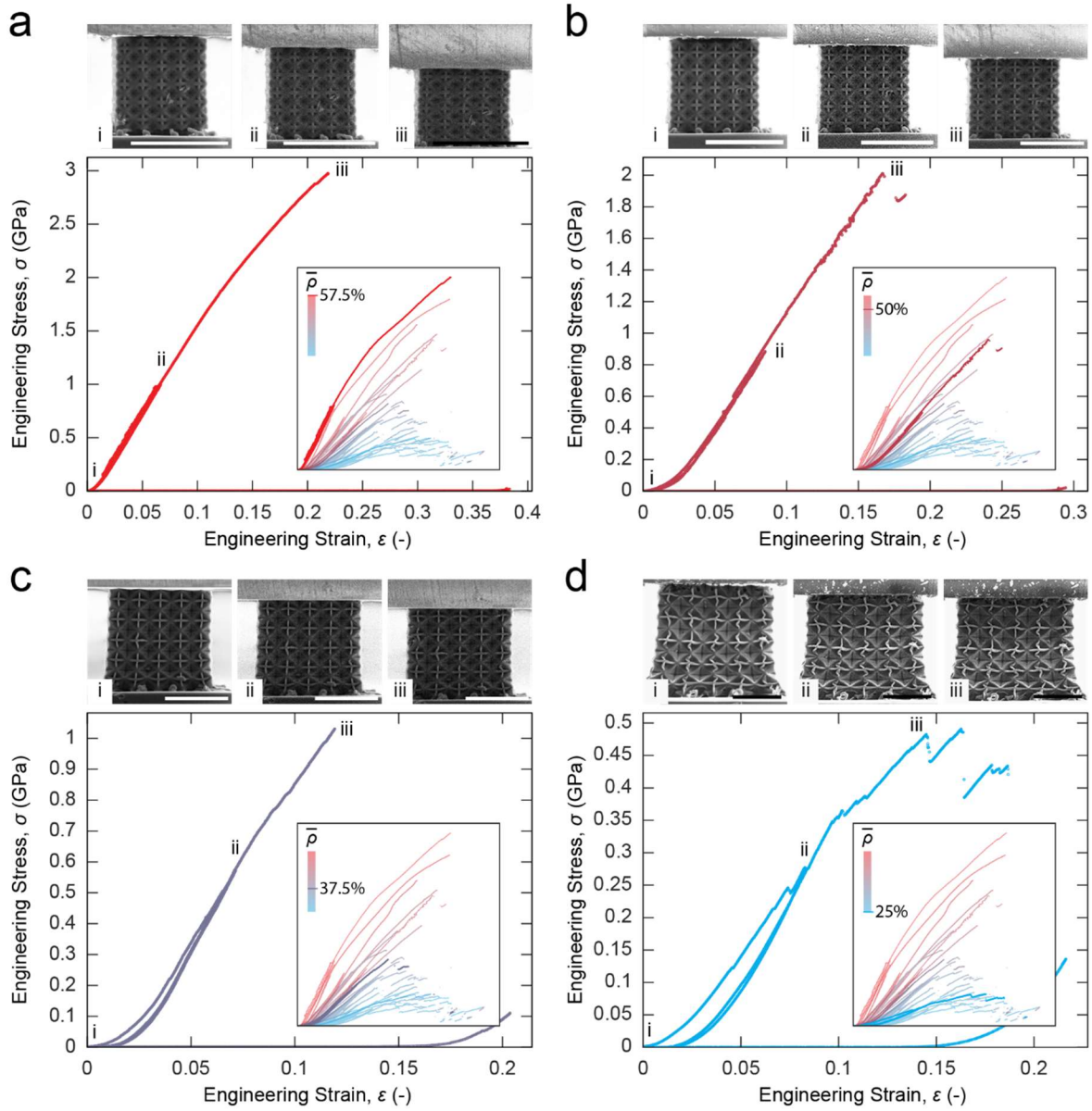

Figure 2.3. *Compression experiments of pyrolytic carbon cubic+octet plate-nanolattices with different relative densities ($\bar{\rho}$). Stress-strain curves of specimens with $\bar{\rho}$ from 57.5% to 25% (a-d) accompanied by front facing in situ SEM images at labeled locations (i, ii, and iii) and comparison to all relative densities, show a transition from brittle fracture to progressive deformation behavior around 37.5% relative density. Scale bars are 10 μm.*

Figure 2.4 shows the stiffness and yield strength results of all tested CO plate-nanolattices. The lines represent the Hashin-Shtrikman and Suquet upper bounds for different constituent material Young's moduli and yield strengths, whereby the shaded regions provide confidence intervals on the bounds given

uncertainties on the material properties of nano-/microscale pyrolytic carbon. For stiffness, the lower and upper limits of the shaded region correspond to constituent Young's moduli of 41 GPa and 62 GPa, as measured from compression of pyrolytic carbon micro-pillars printed using the same process parameters as for the vertical cubic wall (Figure B.1) and the highest reported value for nanoscale pyrolytic carbon[51], respectively. Likewise, for the yield strength the applicable bound range is given by the minimum and maximum yield strengths measured from our micro-pillars, 2.2 and 2.7 GPa, respectively, which are in good agreement with literature data on the tensile and compressive strength of nanoscale pyrolytic carbon[55,56].

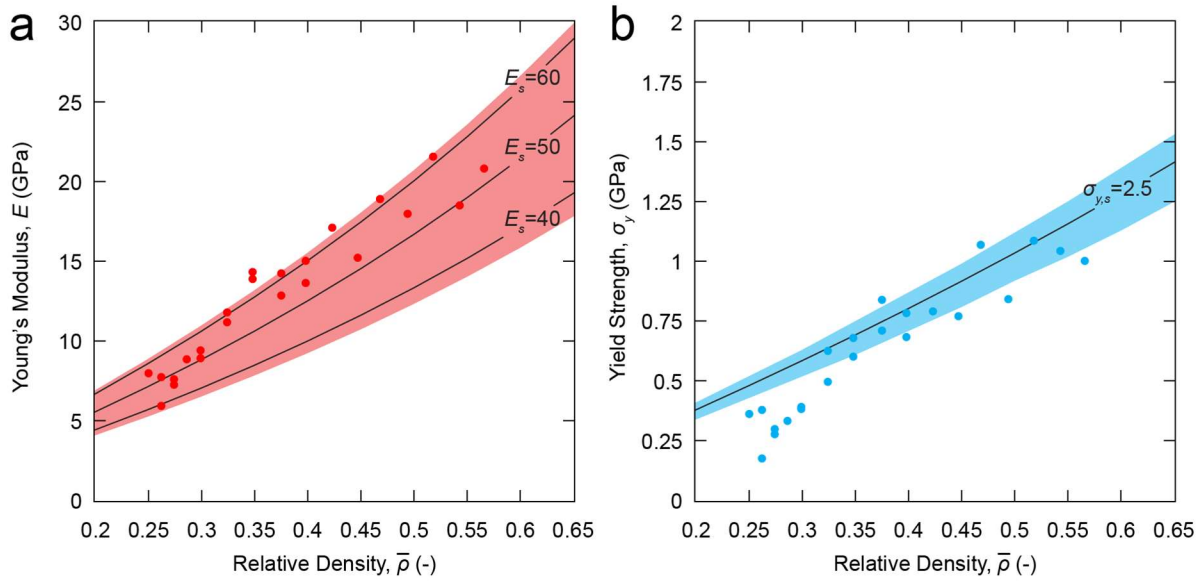

Figure 2.4. *Pyrolytic carbon cubic+octet plate-nanolattices reach both the Hashin-Shtrikman and Suquet upper bounds of an isotropic cellular material for stiffness and strength, respectively. Stiffness (a) and yield strength (b) versus relative density plots show most data points within the shaded upper bound regions, which are given by the constituent property range of pyrolytic carbon. Lines indicate upper bound functions for various constituent materials properties.*

Our CO plate-nanolattices experimentally reach both the Hashin-Shtrikman and Suquet upper bounds of an isotropic cellular material. Our most pristine structures, $\bar{\rho} \geq 37.5\%$, lie at the upper limit of the shaded stiffness region of Figure 4a. For yield strength, the highest-density structures predominantly lie

in the shaded region of Figure 4b, achieving the Suquet bound; the lowest relative density structures ($\bar{\rho} < 37.5\%$) mostly lie below the bound region.

Consistent with the observed transition from linear-elastic to progressive failure and reduced mechanical properties around $\bar{\rho} = 37.5\%$, we identified two characteristic scaling relations of the measured strength and stiffness with the relative density (Table B.1). The effective stiffness of cellular materials (E) can be related to the relative density ($\bar{\rho}$), as $E \propto \bar{\rho}^{b}$[23], with the scaling exponent (b). The effective yield strength (σ_y) can be described as $\sigma_y \propto \bar{\rho}^{c}$ with the scaling exponent (c). Least square fitting of our results with the above scaling relations gave $b = 1.05$ and $c = 0.85$ for $\bar{\rho} \geq 37.5\%$, and $b = 2.22$ and $c = 2.78$ for $\bar{\rho} < 37.5\%$. Near-linear scaling of both stiffness and strength with $\bar{\rho}$, for $\bar{\rho} \geq 37.5\%$, generally indicates efficient stretching-dominated behavior[44]. While scaling and deformation behavior correlation becomes less accurate above $\bar{\rho} = 30\%$[23], the observed shift to reduced scalings around $\bar{\rho} = 37.5\%$ still reveals two distinct deformation regimes with different degrees of efficiency in terms of strength and stiffness.

Figure 5a compares the stiffnesses of pyrolytic carbon plate-nanolattices and cubic+octet finite element models with ideal and pre-deformed unit cells. For $\bar{\rho} \geq 37.5\%$, experiments and ideal finite element results excellently agree, with the computed stiffnesses coinciding with the measured stiffness-$\bar{\rho}$-scaling. The experimentally observed steepening in stiffness scaling for $\bar{\rho} = 37.5\%$ is well captured by simulations with increasing pre-deformations, with magnitudes in agreement with experimental observations. Figure 5b compares the measured yield and compressive strength to the computed elastic buckling strength of ideal models. The shaded region is bounded by the first eigenmode occurring in the octet walls and the vertical wall buckling mode most visible in the experiments. The computed buckling strength notably exceeds the measured yield strength in the high-$\bar{\rho}$ regime and well correlates with the measured yield strength reduction below $\bar{\rho} = 37.5\%$, indicating a transition from yielding to elastic buckling near that relative density. Across the entire $\bar{\rho}$ range the measured compressive strength trends with the computed buckling failure. Given that pyrolytic carbon only shows a modest change in stiffness between

elastic and plastic deformation, the elastic buckling simulations provide a reasonable approximation for the plastic buckling strength, suggesting that high-$\bar{\rho}$ plate-nanolattices fail by plastic buckling following initial yielding. As yield and buckling strength deviate with increasing $\bar{\rho}$, prolonged post-yield deformation results in increasing failure strain with increasing $\bar{\rho}$ (Figure B.2).

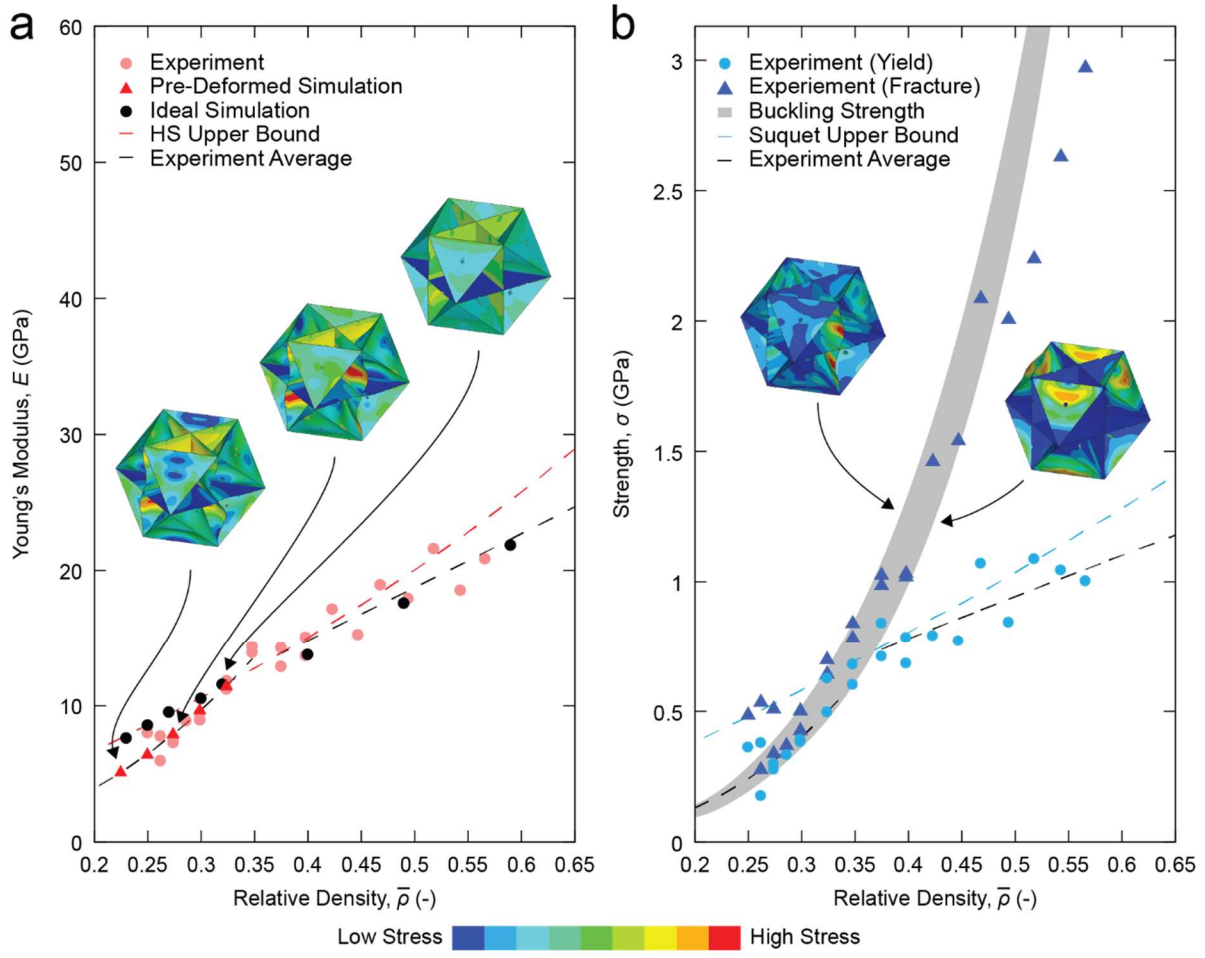

Figure 2.5. *The reduction in experimentally measured stiffness is closely matched by simulations of pre-deformed models (a) and the reduction in yield strength correlates with the buckling strength below* $\bar{\rho} = 37.5\%$ *(b). The first and vertical wall buckling modes of ideal shell element plate-lattices bound the bottom and top of the shaded buckling strength region, respectively. Above* $\bar{\rho} = 37.5\%$*, the compressive strength is limited by post yield-buckling.*

With average compressive strength and stiffness improvements up to 639% and 522%, respectively, compared to the best beam-nanolattices[6,14], our plate-nanolattices are the only reported materials to lie at the theoretical compressive strength limits and the first architected material to exceed synthetic macroscale cellular materials, like ceramic foams[47], in stiffness, thus representing the strongest and stiffest existing architected materials to date. Figure 6 compares the compressive strength and stiffness data from this work with those of other architected and bulk materials[6,14,16–18,20–22,37,40,57–69]. The theoretical limits[6,13,14] are taken as regions bounded by a linear scaling of graphene (the strongest and stiffest known material, albeit in two dimensions and at the nanoscale) and bulk diamond (the strongest and stiffest bulk material at the macroscale). With densities below 0.792 g/cm^3, and compressive strengths up to 3 GPa, our plate-nanolattices achieve specific strengths up to approximately 3.75 GPa g^{-1} cm^3, which surpass all known bulk metallic, polymeric and composite materials, and all technical ceramics, including certain diamond systems[47]. With stiffnesses up to 21.6 GPa, our plate-nanolattices are the stiffest architected material reported to date. Compared to pyrolytic carbon octet truss and isotropic truss nanolattices[14] of the same relative density range, the average improvement is between 137% and 522% for stiffness and between 89% and 639% for strength, at densities of 0.792 and 0.349 g/cm^3, respectively. Considering only the best performing pyrolytic carbon beam-nanolattices, we retain a 100% improvement in strength and a 33%-89% improvement in stiffness. For additional comparison, normalized Ashby charts of stiffness and strength show that the cubic+octet topology of our plate-nanolattices clearly outperforms both beam and shell architectures (Figure B.3).

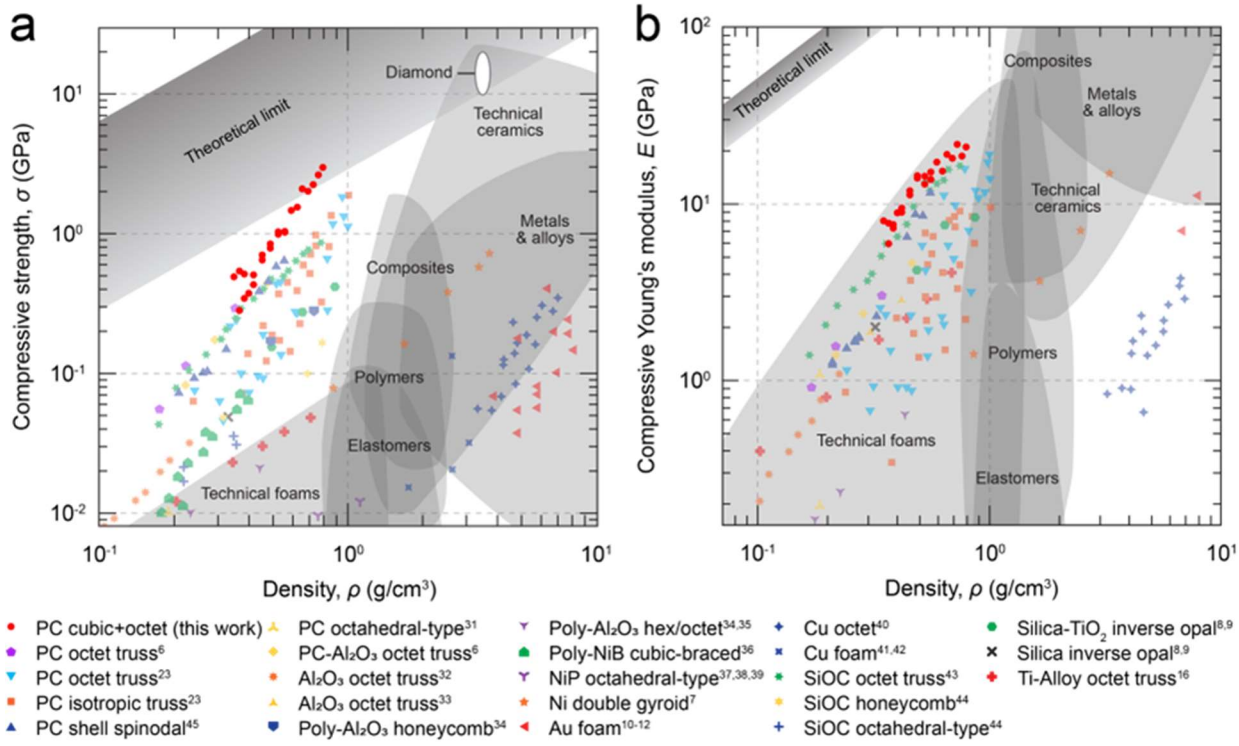

Figure 2.6. *Pyrolytic carbon (PC) cubic+octet plate-nanolattices are the strongest and the stiffest existing materials for their respective densities. Compressive strength (a) and stiffness (b) Ashby maps. The stronger and weaker theoretical limits assume an arbitrary ideal topology with the best possible scaling of one, for two different constituent materials: graphene, the strongest known material at any scale, and diamond, the strongest known bulk material at the macroscale. With up to 639% and 522% average strength and stiffness improvements compared to the most efficient beam-nanolattices, cubic+octet plate-nanolattices are the only architected materials to surpass the bulk theoretical strength limit and to reach specific stiffnesses comparable to those of the best performing technical foams.*

Synthesis of nanolattices from mechanically strong and stiff ceramics or metals requires sophisticated multi-step processes that are complicated to apply to closed-cell topologies and have so far mostly been limited to non-optimal beam-lattice designs. High-resolution 3D additive manufacturing processes are generally limited to viscoelastic polymers, but demonstration of nanolattice performance at the Hashin-Shtrikman upper bound requires linear elastic material properties[26,44] like those of ceramics and metals (Appendix E). Ceramic and metallic nanolattices are manufacturable by conversion[13] from polymer templates such as those printed by TPP-DLW. However, closed-cell designs impose process

restrictions, complicating the adoption of atomic-layer-deposited ceramics[61,66] as well as electroless[62] and electro-plated[63] metals, even for the synthesis of composites[6,61,62] where templates are not removed. Pyrolysis is the only alternative, and requires structures to be fabricated such that they survive extreme linear shrinkage of up to 90%[6].

Here, we overcame several critical manufacturing challenges, leading to fabrication of highly efficient virtually closed-cell ceramic plate-topologies (Appendix A). As with most additive manufacturing techniques, TPP-DLW-printing of fully enclosed cellular geometries results in trapped excess liquid monomer and/or rupture of thin membranes during post-print development. We show that nanometer-size pores are sufficient to eliminate residual monomer from assemblies of even tens of micrometer-size cells, while retaining mechanical performance on par with fully closed-cell topologies. In contrast to TPP-DLW-derived beam-nanolattices, plate-nanolattices cannot simply be printed from individual line features in one three-dimensional trajectory pattern. To address this challenge, we developed an orientation-specific layer-by-layer hatching strategy (Figure A.2) to combine the highest surface quality with smallest possible wall thicknesses, and fully exploited size-dependent strengthening of the constituent material. Material properties of hatched TPP-DLW-derived structures are highly sensitive to printing parameters[70]; thus, carefully selected combinations of laser average power, scan speed and hatching distances were adopted herein to ensure identical constituent properties throughout our nanoarchitected material (Figure A.3). To demonstrate property uniformity, for each plate orientation, micro-Raman spectroscopy measured nearly identical degree of conversion (DC) of pre-pyrolysis polymeric structures and nearly identical degree of graphitization (DG) for all pyrolytic carbon structures (Figure A.3 and Figure A.5 and Table A.1 and Table A.2). While pyrolysis of TPP-DLW printed beam-lattices has been demonstrated, the much larger ratio of unit cell dimensions to feature size in plate-lattices drastically complicates this conversion by pyrolysis, e.g. the overall size of our CO plate-nanolattices is ~3 times larger than that of same-$\bar{\rho}$ octet beam-lattices[6,14] with comparable feature sizes. Given structures with larger surface areas tend to shrink more during pyrolysis, support pillars were coarsely hatched to introduce controlled porosity to lessen the

shrinkage mismatch between the large surface area cubic+octet plate-nanolattices and the monolithic support pillars.

Despite the variability in the properties of pyrolytic carbon at small scales, our cubic+octet plate-nanolattices clearly reside within the bound bands of Figure 4. Size effects strongly increase both strength and stiffness of pyrolytic carbon, with decreasing characteristic length[51,55,71]. In the range of 1 μm and 5 nm, Young's moduli around 40 GPa[55] and 62 GPa[51] are reported, respectively; the former agrees well with our 6 μm-diameter micro-pillar compression results (Figure B.1). Consequently, the Young's moduli of the constituent material in our plate-nanolattices, with wall thicknesses of 150-260 nm, are expected to lie within the above upper and lower limits. Nonlinear least square fitting of the stiffnesses of our most pristine specimens ($\bar{\rho} \geq 37.5\%$) with Equation (2.1), assuming a Poisson's ratio v=0.17[72] and considering a correction function to account for the structure's face holes (Appendix D), estimated a constituent material stiffness (E_s) of 62 GPa. This agrees remarkably well with the literature utilized upper limit from Figure 4a, confirming performance of our plate-nanolattices at the HS upper bound. Regarding strength, literature-reported compressive properties[55] of pyrolytic carbon with characteristic dimensions down to 600 nm agree well with our pillar experiments. Literature-reported ultimate tensile strengths of 2 μm-size specimens of up to 2.75 GPa[56] are also in good agreement, indicating that our pillar-measured yield strengths represent the constituent yield strength of our plate-nanolattices well.

Plate-nanolattices fully exploit the topological advantages of their plate architecture in the higher relative density range. Although all details of the computer models are not fully reflected in our high-$\bar{\rho}$ plate-nanolattices given the limitations of nano-manufacturing, numerical results confirmed that the structural quality of these lattices were sufficient to perform on par with theoretical and numerical predictions, albeit with some experimental scatter. Correspondingly, experiments with polymeric cubic+octet plate-microlattices with near-ideal geometries (Appendix E) correlated well with the pyrolytic carbon results, but with less scatter. Despite manufacturing imperfections, our pyrolytic carbon data has

one of the lowest variabilities among the nanolattices presented in Figure 6. Outliers in stiffness remain within $\pm$6.9% of the average upper bound predictions.

While plate-lattices clearly outperform beam-lattices in the higher relative density range, our results reveal a tradeoff between performance and manufacturability at lower relative densities. Finite element analyses (Figure 5) revealed that the underperformance of the low-$\bar{\rho}$ plate-nanolattices with respect to the theoretical upper bounds in Figure 4 is related to small plate thickness-to-size ratios which promote warping during pyrolysis and hence introduce plate curvature via pyrolysis-induced buckling (Figures 1). Simulations showed that pre-curvature is the key mechanism diminishing stiffness, with a yielding-to-buckling transition at $\bar{\rho} \approx 37.5\%$ also having a strong effect on the strength. As buckling ideally should not affect stiffness measurements, this explains the notably stronger reduction in yield strength compared to stiffness for the low-$\bar{\rho}$ plate-nanolattices. In agreement with the simulations, near-ideal polymer plate-microlattices did not show a transition to worse stiffness scaling at lower relative densities, although the lowest relative density sample displayed reduced strength (6.Appendix E).

The combination of imperfections and premature buckling of low-$\bar{\rho}$ plate-nanolattices led to convergence of our data with theoretically less efficient pyrolytic carbon beam-nanolattices[6], particularly in terms of strength (Figure 6). While the manufacturing complexity of nano-architected materials may amplify these effects, low-$\bar{\rho}$ plate-lattices are, regardless of scale, far more difficult to manufacture without significant geometric defects than beam-lattices due to the more extreme aspect ratios of individual features. Moreover, the theoretical performance of plate-lattices improves as the number of plate elements per unit cell is increased (as in the simple cubic + body centered cubic (SC-BCC) design[42]); however, in practice each additional plate element further reduces the lowest manufacturable relative density, and the simplest topologies like the cubic+octet design may be most practical.

Plate curvature may mitigate brittle failure in plate-lattices. While our high-$\bar{\rho}$, pre-deformation-free specimens failed in a brittle manner, increasing plate curvature at low $\bar{\rho}$ coincided with a more progressive failure behavior, albeit at the cost of reduced mechanical properties (Figure 3). In previous work, highly

curved, thin shell topologies made of brittle constituent materials, such as pyrolytic carbon, have been shown to exhibit progressive failure with high stress plateaus up to 80% strain[69]. This behavior arises from an advantageous crack propagation mechanism displayed by shells with high radius of curvature-to-thickness ratios. In plate-nanolattices, plate curvature induced during pyrolysis also produces such behavior. Interestingly, non-pre-deformed polymer cubic+octet plate-microlattices also exhibited the same transition from catastrophic to progressive failure (Figure E.2) as result of the introduction of plate curvature by post-yield buckling. Therefore, pre-existent plate curvature is not necessary to induce progressive failure, and elastic buckling may as well have contributed to progressive failure in our pyrolytic carbon structures. The implication is that non-pre-deformed thin-walled pyrolytic carbon plate-nanolattices, if manufacturable, may potentially still exhibit beneficial progressive failure without compromising stiffness and yield strength. Plate-designs with more plate elements per unit cell and thinner features, such as the SC-BCC design, may exploit post-buckling curvature-induced progressive failure most efficiently. At the same time, though, thin wall design is complicated by manufacturing limitations and potentially exacerbates defect-induced buckling strength reductions. Ultimately, both pre-existing and buckling-induced curvature are expected to produce a trade-off between compressive strength and deformability.

The combination of an optimal topology at the HS and Suquet upper bounds, and ultra-high strength nanoscale constituent pyrolytic carbon, makes our plate-nanolattices the only cellular material to lie above the theoretical specific strength limit for all bulk materials, as well as outperform all other architected materials in stiffness (Figure 6). Beam-lattices, such as the octet truss, in practice perform on the order of 25% and 20% of the HS and Suquet upper bounds, respectively; which is in good agreement with the found five- and six-fold improvement, respectively, of our plate-nanolattices over TPP-DLW-derived pyrolytic carbon octet truss and isotropic truss nanolattices[14] in the density range of 0.35-0.79 g/cm³.

2.5. Conclusion

In summary, we demonstrated closed-cell plate-nanolattices manufacturable via TPP-DLW and pyrolysis by applying nanometer-size face holes, which we showed to impose only small reductions in mechanical performance, orientation specific hatching strategies and optimization of support structures to minimize shrinkage mismatch with specimens during pyrolysis. This study is the first experimental demonstration of a cellular material reaching the theoretical strength and stiffness limits of an isotropic voided topology. At the same time, the constituent pyrolytic carbon approaches the theoretical material strength limit, thanks to mechanical size-effects. This unprecedented combination of both optimal topology and ultra-strong constituent material culminates in the strongest and stiffest existing architected material, with up to 639% average performance improvement over the most efficient beam-nanolattices.

While beam-based lattices have dominated structural metamaterials[13] for the past two decades, this study is the first comprehensive experimental characterization of plate-lattices, providing important, scale- and process-independent groundwork to establish plate-architecture as a superior design principle. Our results provide understanding of density-dependent performance and deformation behaviors in light of previous theoretical work and highlight several critical areas of interest for future work, including imperfection sensitivity, and design-dependent manufacturing limitations. Although the TPP-DLW/pyrolysis fabrication route developed in this work is limited to small specimens, plate-lattices with exceptional size-strengthened constituent materials may be manufactured by more scalable techniques (e.g., projection micro-stereolithography[73]) using new preceramic resins which exploit size effects into the micrometer range coupled with dramatically reduced shrinkage during pyrolysis[12]. Hence, plate-nanolattices deserve strong attention in the development of scalable high-resolution additive manufacturing processes[15,74], which might in future make carbon-based nanoarchitected metamaterials as ubiquitous as carbon composites have become in modern engineering applications.

3. Synthesis of Hollow Alumina Particles for Scalable Manufacturing of Size-Effect Strengthened Syntactic Ceramic Foams

3.1. Abstract

Hollow particles are of immense relevance to a number of applications, from opacifiers[75], to inverse photonic glasses[76], dielectrics[77], battery cathodes[78], acoustic impedance matching layers[79] and, most relevantly here, syntactic foams[31,80,81]. Syntactic foams are closed-cell foams made from hollow particles dispersed in a matrix. The matrix and particles can be made of different or identical materials. While ceramic syntactic foams with nano-/micro-sized pores and ligaments are expected to benefit from significant size-effect enhancements in addition to high stiffness and strength derived from the closed-cell structure and uniform porosity (see Chapter 4), there is currently no scalable way of manufacturing them, much less a viable source of hollow particles to be utilized as precursor porogens in the quantities needed. Here, a demonstration of a material-agnostic sol-gel emulsion evaporation technique is provided, that lays the foundation for large-scale template-free synthesis of hollow ceramic particles with 1 μm – 1 mm diameters and wall thicknesses tunable between <1% and 33% of the particle diameter. In addition to producing hollow alumina particles for syntactic foams as demonstrated here, this approach opens potential applications for a suite of interesting hollow particle engineering materials in optics with high refractive index titania[82], zirconia shape memory ceramics[29], and zinc oxide piezoelectrics[83].

3.2. Introduction

Though the cubic+octet plate-nanolattices of the previous chapter are isotropic, maximally stiff and strong, their closed-cell structure is not manufacturable by any scalable additive or assembly process at

present. Furthermore, the thin walls of low relative density plate-lattices make them subject to premature deformation during manufacturing and elastic buckling, which result in properties that converge with inefficient beam-based topologies in the lower limit of relative density. On the other hand, stochastic foams are scalably produced but the traditional methods for manufacturing them result in poor control of porosity, leading to larger knockdowns to stiffness and strength. Syntactic foams, i.e., foams assembled from one or more monodispersed sizes of hollow spheres (also known as cenospheres), offer better stiffnesses and strengths compared to traditional open or closed-cell designs, due to excellent control over their pore size distribution (see Figure 1.5). However, ceramic and metallic syntactic foams are currently only manufacturable either by melt casting or powder metallurgy which impose restrictions on the minimum obtainable pore size and wall thicknesses[32,33]. While syntactic foams composed of size-effect strengthened hollow ceramic particles only several microns in diameter would result in far superior mechanical properties, there is presently no process suitable for producing hollow ceramic microparticles of the scale and quantity required.

An optimal process for fabrication of our hollow microparticles must satisfy the following conditions: (i) hollow particles must be discrete and with hollow cores, (ii) particles can be fabricated in diameters of 1-100 μm, or potentially larger, (iii) particles must minimally aggregate in an emulsion and during drying, (iv) particles are compatible with monodisperse emulsification techniques, (v) shells are nonporous after high temperature calcination, (vi) particle surfaces are smooth, permitting optimal flowability, (vii) the chemical systems are amenable to future scale-up for large production quantities, and (viii) other material chemistries can potentially be used with minimal additional development.

While hollow ceramic microparticles are not a recent development[84], their production remains challenging due to difficulties associated with agglomeration, scalability, and reactivity of many non-silica precursors. These challenges have spawned a large assortment of different approaches, each with significant tradeoffs relating to the particle size, dispersity, maximum and minimum wall thickness, and constituent materials[75,85–88]. All these techniques are classifiable into one of two families, templated and template-free

syntheses. In the former, a sacrificial core, typically a polymer or silica, is coated and subsequently removed via etching, dissolution, or burnout. Template coating methods include mechanofusion[89], vapor deposition[90], and sol-gel chemistry[91–93]. Though templated techniques are the most common, they have several disadvantages, namely small production volumes, expensive template feedstock or long prerequisite template syntheses, cracking from template burnout, and template agglomeration[94,95]. Template-free approaches are generally more diverse, including interfacial polymerization[86,87], metallic nanoparticle oxidation[96], thermal plasma spraying[88], spray drying[97] and emulsion gelation[98] but of poorer quality and control than comparable templated hollow particles.

The principal disadvantages of interfacial polymerization are the immiscibility requirements of the disperse and continuous phases and the limitations associated with shell thickness as it relates to interfacial diffusion. While this approach works well for some systems, namely titania and silica with small particle sizes and thin walls, it can be difficult to identify systems of solvents in which the precursor chemical (typically a metal alkoxide) is miscible, but water is not. Without immiscibility between the phases containing the precursor and the water, the two would intermix resulting in the precipitation of solid aggregates. Nanoparticle oxidation is impractical for both hollow particles larger than a few tens of nanometers and the quantities required to fabricate a bulk foam. Spraying techniques are intrinsically limited to polydisperse particles with limited control of the size distributions. In contrast, emulsion gelation utilizes sols, suspensions of colloidal particles. In principle, any stable sol, can be used which makes it potentially compatible with a broad range of oxide materials, but it's only been demonstrated in one study for which limited information on the process is included[98]. This process involves combining a stable sol with a physical blowing agent that vaporizes upon heating and a film forming agent that undergoes reversible thermal gelation providing a scaffold during gelation of the sol shell. The sol along with the additives is dispersed by aerosolization where droplets form hollow green gelled spheres upon contact with a hot oil bath.

In this work, a combined sol-gel emulsion evaporation method derived from the emulsion gelation approach is developed to fabricate hollow alumina microparticles. First, a stable sol is prepared via modified sol-gel techniques using metal alkoxides. The sol is combined with film forming, blowing, and gelation agents. The sol mixture is then emulsified in a continuous oil phase by homogenization, but compatible with other emulsification techniques specified in Section 3.4 to control the size and dispersity of the final particles. Once heated, the emulsified sol droplets begin to gel via thermal decomposition of the gelling agent as the blowing agent vaporizes, forming a hollow internal cavity. Simultaneously, the film forming agent undergoes reversible thermal gelation, which creates a scaffold in which the sol-gel may crosslink. Once all the blowing agent has evaporated and the walls crosslinked, the green (gelled) particle shells are then either centrifuged or vacuum filtered and washed or simply air dried. At this stage, the walls are still partially porous, so a final calcination step is used to close the surface pores of the green particles producing hollow nonporous ceramic microshells.

3.3. Sol-gels

The term sol describes a stable suspension of nanoparticles in a liquid, while gel constitutes a porous continuous solid network which supports a continuous liquid phase. Together they make up the low temperature chemical process of creating ceramics as thin film coatings, porous 3D networks, nano/micro-particles, and fibers[99]. The primary advantage to utilizing sol-gels is the ability to coat and process materials at low temperatures and synthesize high porosity and surface area, low density monoliths. For this reason, sol-gels are most prominently utilized to make aerogels, low density monolithic networks formed by supercritically drying a wet gel. Sol-gel processes are incredibly sensitive to variations in the processing conditions, namely molar ratio of metal alkoxide to water, type of metal alkoxide, hydrolysis time, presence of electrolytes, pH, temperature, solvents, acid concentration and type for peptization, aging time, and drying technique[100]. While the most common sol-gels are made from silica due to its ease of

processing, availability, and documentation, in principle any metal oxide is synthesizable by appropriate choice of precursor, solvent media and catalyst. An overview of typical sol-gel procedures as generally used to produce xero-, aero-, and cryogels is shown in Figure 3.1. These constitute the predominant usage of sol-gels and thus they have received the most attention and development by researchers. As such, the chemistries and processing techniques form a foundation for the work used herein to fabricate hollow ceramic particles.

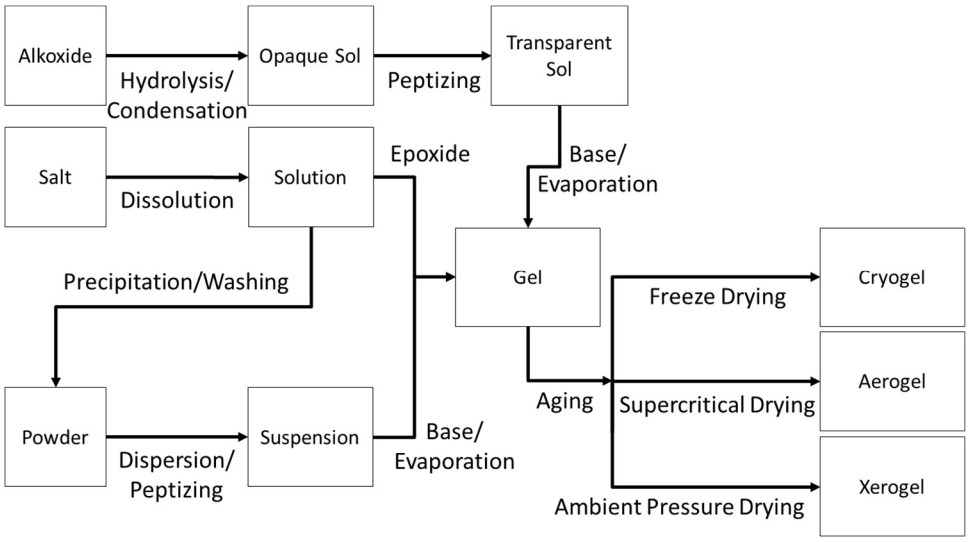

Figure 3.1.*Overview of typical sol-gel procedures.*

As mentioned previously, the sol for this process must satisfy multiple criteria: (i) it must be stable (not sediment appreciably, gel or precipitate over the course of approximately 7 days), (ii) it must have peptized particles smaller than 100 nm (a requirement for microfluidic droplet generation, smooth surfaces and thin walls in the smallest of particles), (iii) it must have high chemical purity (avoiding introduction of Si, Ca, and Na impurities which form poorer property aluminate phases), (iv) it contains sufficiently high solid loading fractions (ensures shell walls are resilient to drying and calcination), (v) gelation is thermally triggerable in the emulsion, (vi) its viscosity is low enough that it is amenable for use in microfluidic devices, and (vii) the disperse sol phase has low miscibility with the continuous oil phase of the emulsion

(prevents intermixing and collapse of the emulsion). Though synthesis of the sol is rather simple in practice, the sensitivity to preparation conditions (e.g., precursor to water molar ratio, hydrolysis temperature, solvent concentrations, peptizing acid, chelators, etc.) can dramatically alter the stability and final properties of the sol and the resultant gel.

The first alumina sol-gels were reported by Yoldas[101] and utilized aluminum alkoxides as precursors, specifically aluminum isopropoxide (AIP) and aluminum tri-sec-butoxide (ATSB). When hydrolyzed in water, the alkoxide undergoes simultaneously hydrolysis and condensation reactions, as in:

$$\equiv M-OR + H_2O \longrightarrow \equiv M-OH + R-OH \quad \text{(Hydrolysis)}$$

$$\equiv M-OH + RO-M\equiv \longrightarrow \equiv M-O-M\equiv + R-OH \quad \text{(Condensation)} \qquad (3.1)$$

$$\equiv M-OH + HO-M\equiv \longrightarrow \equiv M-O-M\equiv + H_2O$$

The rate of hydrolysis and condensation is closely linked to the coordinating ligands and whether the precursor is monomeric. Despite having smaller ligands compared to ATSB, AIP has a lower reactivity due to its tri- or tetramer structure[102]. This is also readily apparent given that AIP exists as a stable crystalline solid, while ATSB is a viscous, honeylike liquid which rapidly reacts with ambient moisture to produce a white flaky skin.

Yoldas identified a conversion from hydroxide to monohydroxide occurred upon heating the aluminum alkoxide solutions above 60° C, which was a prerequisite to peptizing, the process of converting a precipitate to a colloid, a transparent sol[101,103] (e.g., a sol with the smallest particle size). After heating, the sol is then peptized via the addition of an acid. The concentration of acid plays a critical role given that strong acids such as nitric and hydrochloric acids also act as electrolytes which in higher concentrations may induce premature gelation by collapsing the electric double layer[103]. Yoldas identified an optimal acid concentration of ~ 0.07 mol acid per hydroxyl group for sols prepared from ATSB which achieves the

smallest gelling volume (e.g., most stable sol) when boiled to gelation. This acid concentration is the optimal below which the insoluble hydroxide precipitates do not form a colloid and above which the kinetics of gelation are accelerated.

More recently, epoxide-assisted gelation has become the favorite method for producing non-silica aerogels because of the lower cost of precursors (alkoxides are typically expensive), versatility of the metal ion (potentially any metal salt can be used as a metal ion source), and more straightforward preparation and control of condensation reactions as compared to the hydrolysis and peptization steps performed with alkoxides. To synthesize alumina aerogels, an aluminum salt, such as $Al(NO_3)_3 \cdot 9H_2O$ or $AlCl_3 \cdot 6H_2O$, is dissolved in a solvent medium. These salts readily dissolve in water and alcohol media. After dissolution the addition of an epoxide, such as propylene oxide or epichlorohydrin, results in gelation. By utilizing different epoxides (ring sizes) and solvents, it is possible to control gelation time, network morphology, and porosity[104,105]. A curiosity of this approach is that below a critical concentration of epoxide, gels will not form, but above this concentration even with separate stepwise additions of epoxide a rigid gel network will form. This is seemingly an ideal route to synthesize hollow particles; however, condensation proceeds indefinitely after the addition of the epoxide and a suitable independent thermally triggerable reaction to produce an epoxide which induces gelation was not identified.

Summarizing, most reported syntheses of sol-gels for xero-, aero-, or cryogels where minimally concerned with the gelation time so long as it was not instantaneous, because the gels were left to age in molds immediately after synthesis until drying in air, supercritical extraction or freeze drying depending on the desired final state. In contrast, the work detailed here relies heavily on controlling the point of gelation precisely within the synthesis with minimal change to viscosity and particle size proceeding that. Without this control, changes in viscosity, particle size, etc. would lead to deviations in the final distribution of the particle sizes and internal cavities during emulsification and in the worst-case solid particles, bulk gelation or clogging of microfluidic devices. Even in the most dilute stable sols (100:1 H_2O: ATSB) prepared here and also reported in literature, the viscosity slowly increases over time[106]. Though it's noted that this

change is very gradual and occurs over the course of approximately 1 month, longer than the processing window needed here for demonstration purposes, this would become problematic when syntheses were scaled to produce larger volumes of particles. Furthermore, increasing the molar ratio of precursor to water significantly hastens this aging process. When higher concentration colloids (higher solid loading fraction) are required, gelation may even occur during or prior to peptization. This is a consequence of the high reactivity of most non-silica-based precursors. A common solution involves the introduction of a chelator that substitutes an alkoxide ligand, coordinates the metal ion at two or more sites, reduces its reactivity and prolongs the life of the sol. For aluminum alkoxides, the two most common chelators are ethyl acetoacetate (EAcAc) and acetylacetone (EAcAc)[106–108]. Both belong to the chemical family, β-diketones, which undergo keno-enol tautomerism because of the two carbonyl groups which permit double coordination of the Al ion and better stability.

Separately, the addition of hexamethylenetetramine (HMTA) can be used to trigger irreversible gelation by heating sols with and without a chelator. HMTA decomposes in aqueous media to formaldehyde and ammonia at temperatures around 80° C[109] as shown in:

$$\cdot\text{HMTA} + 6\,H_2O \xrightarrow{\triangle} 6\,\text{HCHO} + 4\,NH_3 \qquad (3.2)$$

Evolved ammonia converts to ammonium hydroxide in aqueous solution which increases the pH of the sol resulting in irreversible condensation and gelation. After emulsifying a sol containing HMTA, gelation may be triggered by simply heating the emulsion.

3.4. Emulsification, Gelation and Drying

Once the sol has been synthesized, it may be combined with those additional film forming, gelation and blowing agents before dispersion into droplets. In this work, the sol comprises the disperse phase; thus,

the emulsion is a water-in-oil type. Making water-in-oil emulsions presents its own challenges, that is stability is often less than oil-in-water because charge repulsions of polar continuous media and surfactants is not present in oils. However, utilizing long chain polymer surfactants such as ABIL EM 90 and ABIL EM 180 improves their stability. In many cases, ionic (anionic and cationic) surfactants are added to the disperse water phase to improve stability, however this was explicitly avoided because of the potential for ionic surfactants to act as electrolytes in the sol and trigger premature gelation. Typical oil continuous phases include mineral, paraffin, and silicone oils. However, the best results found here were with a petroleum derived isoparaffinic, Isopar-G, which had low viscosity and high stability water-in-oil emulsions when combined with ABIL EM 90 and 180 nonionic surfactants.

Over the years, multiple approaches have been developed to create emulsions, ranging from microfluidic droplet generators[110–112], membrane emulsification[113], vibratory droplet breakup[114], homogenization, and sonication[115]. While the work here is limited to polydisperse demonstrations of hollow particles made form emulsions by homogenization (high shear breakup of disperse phase into droplets) and subsequent heating (Figure 3.2a), the other methods illustrated in Figure 3.2b-d could be used to obtain monodisperse emulsions in larger quantities for future work. These include interfacial polymerization in which a precursor is dispersed in a water immiscible phase and droplets are created from the regular breakup of a capillary stream agitated by a sinusoidal vibration of a piezoelectric crystal (Figure 3.2b), vibratory droplet breakup in air of a stable sol (Figure 3.2c), or microfluidic droplet generation by tip-streaming or dripping modes (Figure 3.2d).

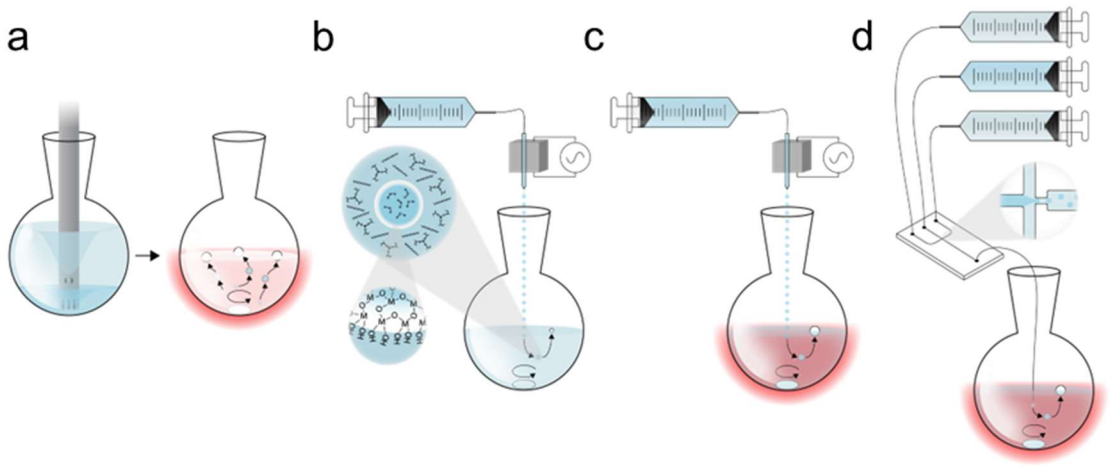

Figure 3.2. *Emulsification by homogenization (a), interfacial polymerization (b), in-air vibratory droplet generation (c), and microfluidic droplet generator chips (d).*

After emulsifying the sol using the previous techniques excluding interfacial polymerization, gelled particles are obtained by simply heating the emulsion under stirring to prevent agglomeration and stagnation. These particles may be left to age to promote higher crosslinking within the shells before drying. Drying may be performed either by air drying the particles directly or by centrifuging or vacuum filtering as illustrated in Figure 3.3a and b. The dry particles are then calcined in a furnace to obtain the final hollow ceramic particles as shown in Figure 3.3c.

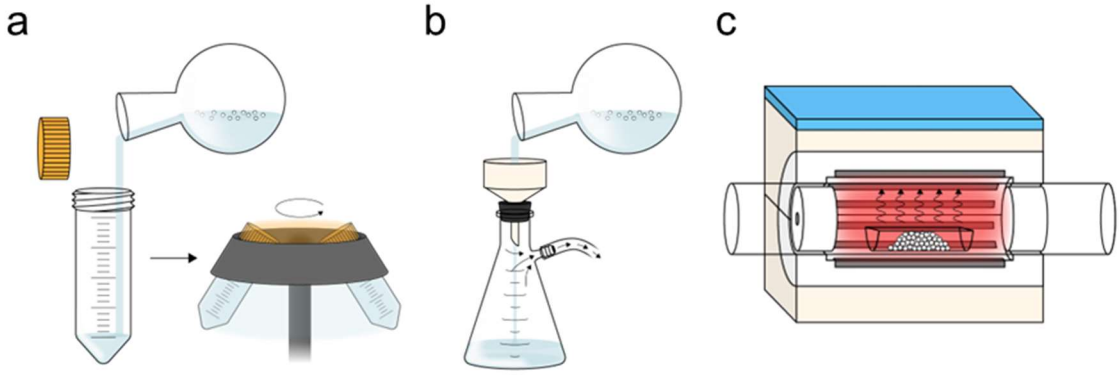

Figure 3.3. *Separation by centrifuging (a) or vacuum filtration (b) and calcination in a tube furnace (c).*

3.5. Synthesis and Optimization of Alumina Sols

Bottle tests were performed on various molar concentrations of aluminum alkoxide precursors to determine the best recipe for forming a stable alumina sol for synthesizing hollow ceramic particles. Two precursors were considered, aluminum isopropoxide (AIP) and aluminum tri-sec-butoxide (ATSB). Both of these precursors have previously been utilized to form aerogels of alumina. All hydrolysis was performed in 85° C water for 30 minutes followed by peptization via the dropwise addition of 70 wt% nitric acid. The resultant sols are shown in Figure 3.4.

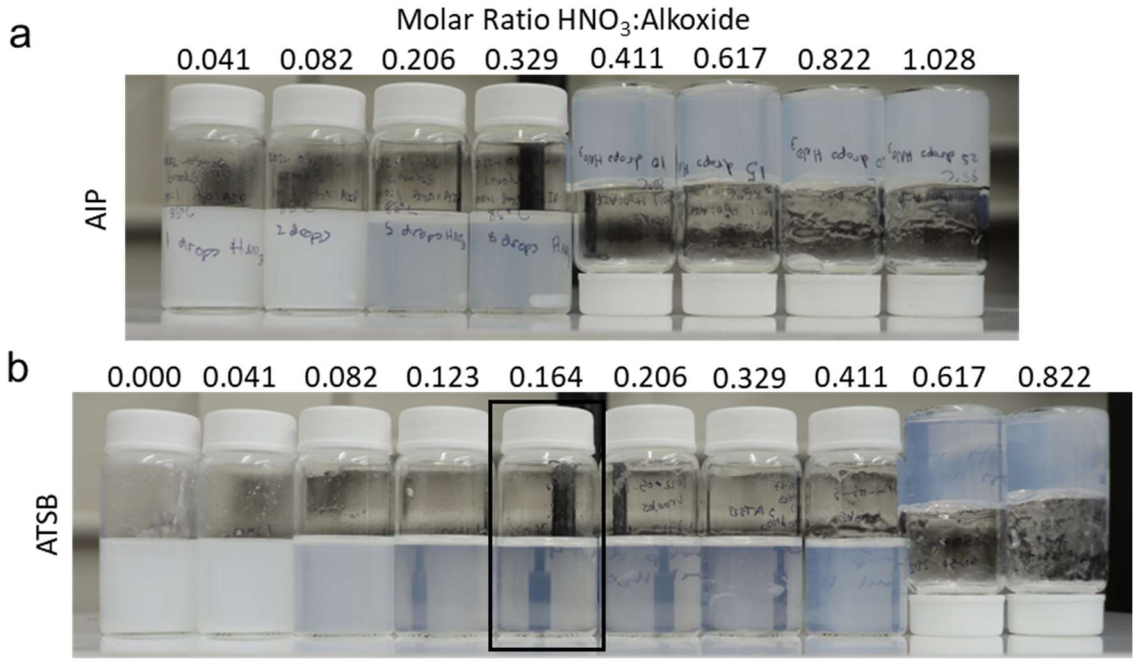

Figure 3.4. *Sols prepared from AIP (a) and ATSB (b) by hydrolysis in hot water for 30 minutes followed by varying addition of 70 wt% nitric acid. Samples prepared with the highest acid concentrations in both the AIP and ATSB systems gelled immediately after peptization. The optimal stability sol is outlined in black.*

Except for those samples with no or minimal added acid, all show clearly bluish hues indicative of Rayleigh scattering from nanoparticles. It is also clear that sols prepared with ATSB are more transparent

than AIP, which likely correlates with smaller particle sizes given the molar concentration is identical for both precursors and by extension the fired solid percent oxide content. Tri- and tetramer molecules of AIP may explain larger particle sizes between sols prepared with AIP as compared to monomeric ATSB precursors. For these reasons, all other sols were prepared herein with ATSB as the precursor. Additionally, it is noted that all ATSB samples with acid to alkoxide molar ratios above 0.329 gelled one day after peptization and though the sample with a molar ratio of 0.206 did not gel, the solution became turbid likely indicating coarsening of particle sizes as seen in Figure 3.5. Other attempts to synthesize sols from higher molar ratios of ATSB:H_2O and/or peptize with glacial acetic acid formed either extremely viscous sols or immediately gelled. Therefore, further processes were performed with 100:1 molar H_2O:ATSB sols unless otherwise specified.

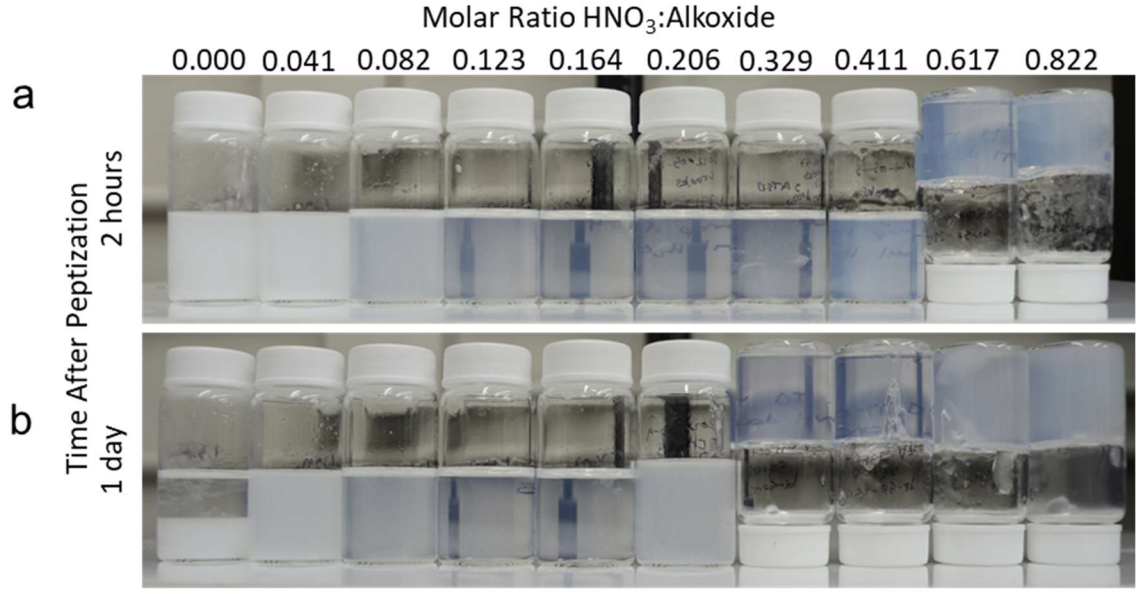

Figure 3.5. *Time-dependent gelation behavior of ATSB sols. Following peptization, sols with higher acid concentrations gelled after 1 day.*

To test that the sol could be thermally gelled, a 100:1 molar ratio H_2O:ATSB sol was prepared by hydrolysis at 85° C for 30 mins after which the sol was peptized by dropwise addition of 70 wt% nitric acid until the

molar ratio of acid to precursor of 0.164 was reached with a pH of ~3-4. As with the previously prepared sol in Figure 3.4b, a transparent sol with a blueish tinge was formed. Thereafter, 1 wt% HMTA (gelling agent), 2 wt% 15 cP methyl cellulose (MC) (film forming agent) and 20 wt% acetone (physical blowing agent) was added to mimic the initial formulation of the disperse phase used in emulsions. After heating for 30 min at 85° C, the mixture formed a solid permanent gel which even after 9 months retained its shape as shown in Figure 3.6.

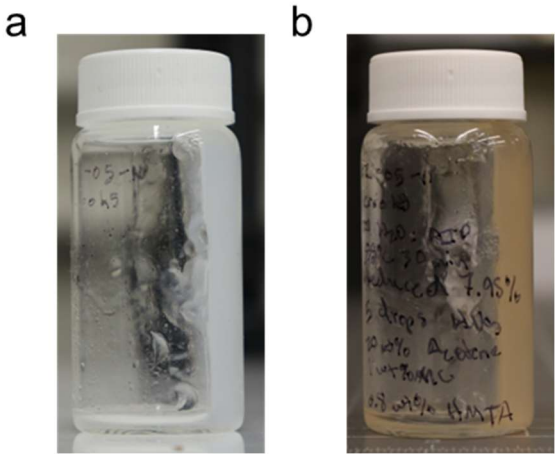

Figure 3.6. *100:1 molar ratio H_2O:ATSB sol with addition of 1 wt% HMTA, 2 wt% 15 cP MC and 20 wt% acetone gelled by heating at 85° C for 30 min (a) and after 9 months of storage (b). The reddish hue is likely due to oxidation of remaining nitrate.*

3.6. Hollow Particles Formed from Gelled Emulsions

Using the 100:1 molar sol prepared previously with the addition of HMTA, MC and acetone, emulsions were made by combining Isopar-G with 2 wt% ABIL EM 90 and the sol in a volume concentration of 20% v/v in a round bottom flask. A homogenizer (Ika T 25 digital ULTRA-TURRAX with a S 25 N – 18 G Dispersing tool attached) was immersed in the round bottom flask after which shear forces from homogenization at 8000 rpm for 1 min dispersed the sol phase into small droplets with sizes between 1-40 μm in diameter characterized by a log-normal distribution. The homogenizer was then removed, and a

magnetic stir bar was placed inside to agitate the emulsion and prevent unwanted agglomeration during the subsequent heating step. The emulsion was heated in a mantle under strong stirring to 95° C and left for 30 minutes. The resultant emulsion showed thin-walled hollow particles as seen in Figure 3.7. Unfortunately, the walls of the particles were too thin and several could be seen collapsing in optical images of the emulsion in Figure 3.7a and c. Likewise, these same particles were also observed collapsing from surface tension as the remaining liquid evaporated from the internal cavity and walls when a drop of the emulsion was placed on a glass slide for imaging (Figure 3.7b and d). This prevented the particles from being centrifuged or vacuum filtered to be collected and calcined. While an obvious solution would involve a solvent exchange to an alcohol such as isopropanol and then super critical drying with CO_2 to prevent collapse of the particles during drying from surface tension, it would be unlikely to ensure that particle remained intact and undamaged during handling and subsequent calcination. Furthermore, the smallest of the particles were below the smallest commercially available critical drying sample holders which would require development of a custom dried or sample holder.

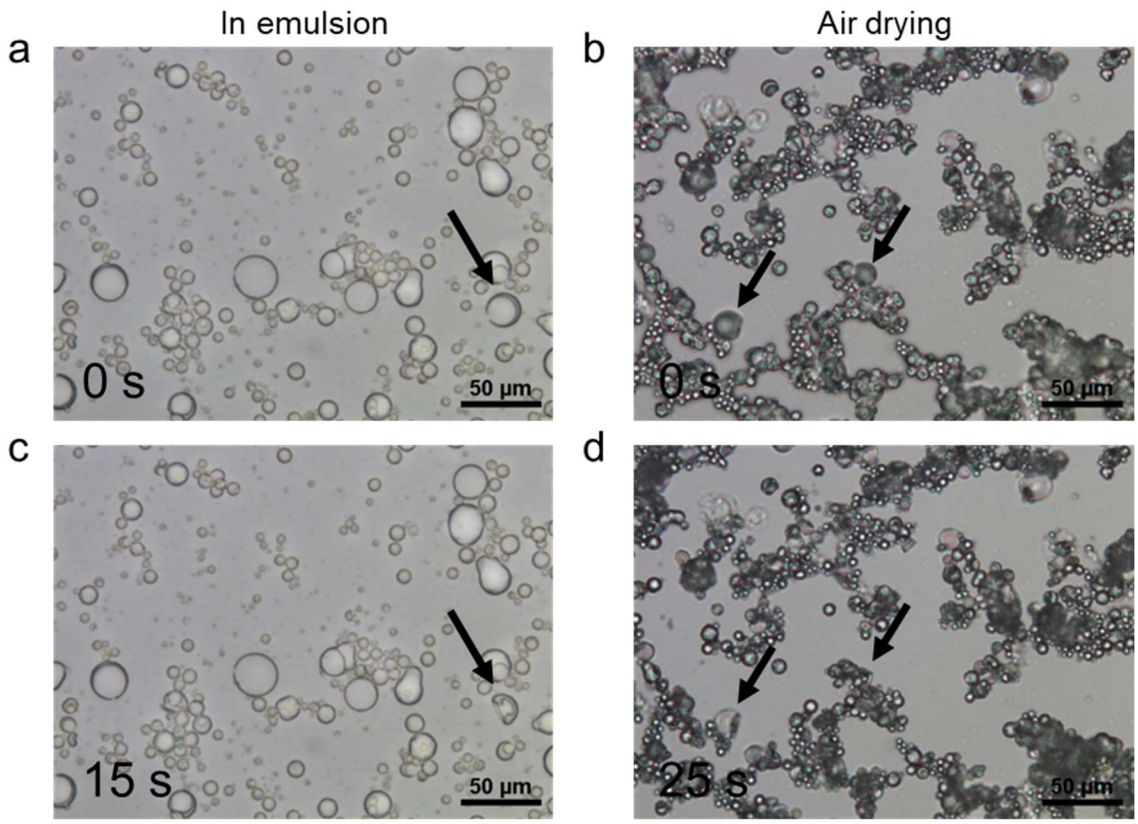

Figure 3.7. *Optical images of hollow particles made from 100:1 H_2O:ATSB with solid wt% of ~3-4% with 1 wt% HTMA, 2 wt% 15 cP MC and 20 wt% acetone emulsified in Isopar-G and then gelled at 85° C for 30 min. Left side panels show hollow particles in the emulsion at 0 (a) and 15 s (c) and right-side panels show hollow particles air drying on a glass slide at 0 (b) and 25 s (d). Arrows highlight particles that collapsed due to thin walls or surface tension from evaporation.*

Instead, the more straightforward approach to make particles more resilient to drying was to increase the wall thickness. This necessitated the synthesis of a higher solid weight fraction sol. Unfortunately, attempts to concentrate the peptized and unpeptized 100:1 molar ratio sol by rotovaping and vacuum heating all led to premature gelation. For this reason, a higher molar ratio sol (50:1) was prepared by chelating the ATSB with EAcAc during hydrolysis. As seen in Figure 3.8a, the unchelated sol on the left gels immediately after peptization. By contrast, the chelated sol (Figure 3.8b) forms a solution of similar hue and transparency as the original unchelated 100:1 molar ratio sol, but with a higher solid weight fraction of approximately 7-8%.

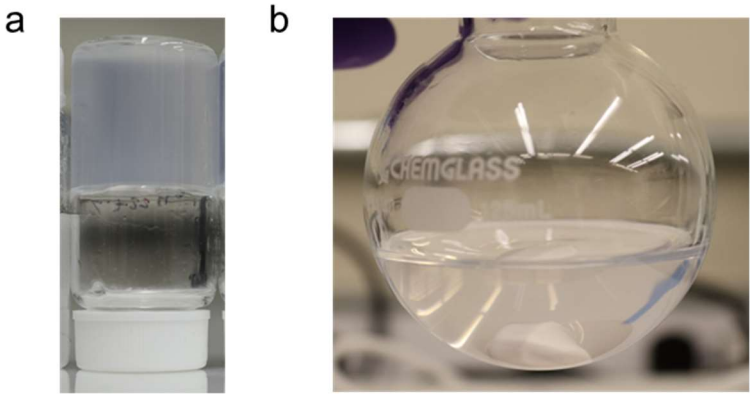

Figure 3.8. *50:1 molar ratio H_2O:ATSB sol prepared with (a) and without (b) chelation by EAcAc. The inverted bottle in the unchelated sol indicates the sol gelled immediately after peptization.*

Again, an emulsion was formed by homogenizing the 50:1 molar ratio chelated sol with Isopar-G. However, to help prevent collapse of the particle walls during drying, the gelation time was extended to 2 hours to promote further crosslinking of sol particles and improve the strength of the green state walls. Likewise, the weight percent of acetone was lowered to 15 percent to produce smaller internal voids. Additionally, the surfactant ABIL EM 180 was used instead at a concentration of 5 wt% in the continuous oil phase and the volume fraction of the sol phase was reduced to 5% v/v to improve the higher temperature stability of the emulsion and prevent agglomeration during the longer gelation time, respectively. All other parameters were held constant. The resultant particles had much thicker walls, approximately 1/3 of the diameter which was consistent across all particle sizes. Though residue was visible on the glass slides during optical imaging, the vast majority of dried material comprised intact hollow particles. This indicated that the chelated sol was successful at forming denser (thicker walled) hollow particles. Dried hollow particles calcined at 200° C for 1 hour are shown Figure 3.10 in which the insets clearly show an intact centrally located pore. Importantly, it is evident that even small changes to the solid weight fraction and acetone concentration produce significant changes in the wall thickness.

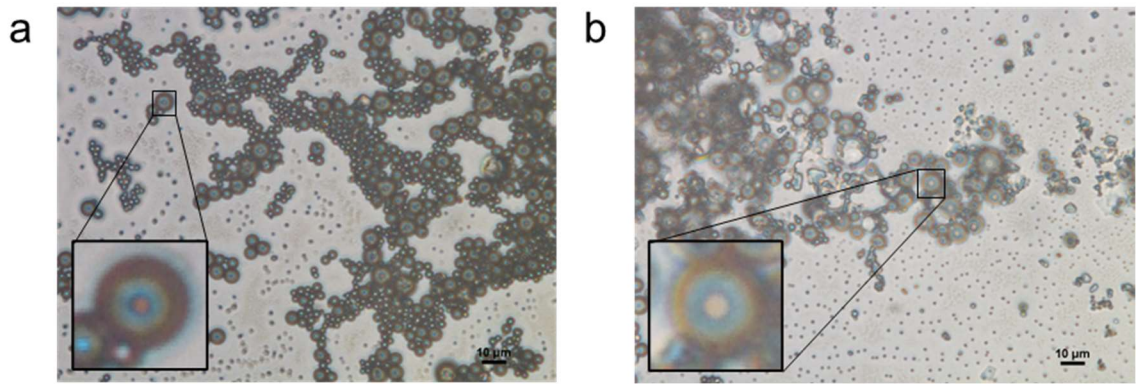

Figure 3.9. *Unwashed (a) and IPA washed (b) hollow particles calcine at 200° C made from 50:1 molar ratio chelated ATSB sol.*

There was some concern the particles would be susceptible to collapse if washed with isopropanol (IPA) given that both the continuous phase, Isopar-G, and disperse sol were miscible with it. Thus, washing could swell the green gel walls and internal cavity leading to rupture. However, this was observed not to be the case. Furthermore, upon closer inspection of the IPA washed particles (Figure 3.9b), the internal cavity seems lighter colored which might indicate removal of entrapped residual water and byproduct alcohols from condensation and gelation of the sol. Also interestingly, it seems that the slower kinetics of the chelated sols resulted in the formation of rod structures during gelation which are characteristic of crystalline boehmite particles (Figure 3.10).

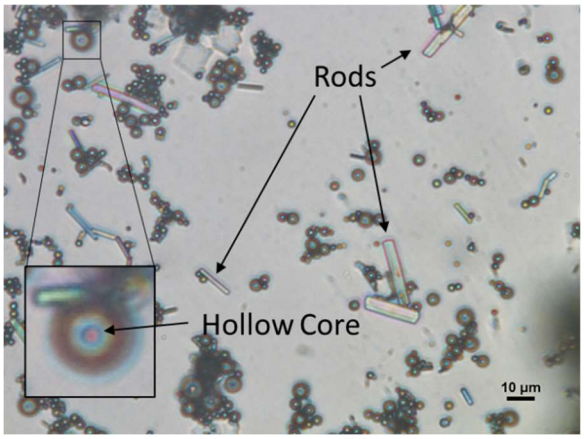

Figure 3.10. *Rodlike particles formed during gelation of the 50:1 molar ratio chelated sol in emulsion prior to heating at 200° C with an inset of a hollow particle in which the interior void is clearly visible.*

Unfortunately, HMTA also undergoes a secondary side reaction with β-diketones as shown in Figure 3.11 resulting in precipitates which was identified soon after the previous emulsion was created. This reaction proceeds slowly in comparison with the processing of the sols and emulsions where a noticeable color change was visible after a few hours, but precipitates were only observed after approximately 2-3 days. While this may have contributed to the thicker walls of the particles, it seems that in the current formulation of the disperse phase, it is unavoidable. Though not investigated here, several proposed solutions requiring extensive secondary investigations include the use of alternative chelators which do not react with HMTA or conversely an alternative gelation agent that does not react with HMTA. As mentioned at the very beginning of this section, the epoxide-assisted gelation approach is attractive but finding a mechanism by which to trigger gelation upon heating was not identified. Nonetheless, should a reaction to produce an epoxide via a thermal degradation in aqueous solutions be identified, that may serve as a suitable alternative to the alkoxide approach used here.

Figure 3.11. *Reaction of EAcAc (left) and AcAc (right) with 1 wt % HMTA in DI water. Color and precipitates are the results of undesirable side reactions occurring between HMTA (gelling agent) and EAcAc/AcAc (chelating agent).*

3.7. Conclusions

In summary, a combined sol-gel/emulsion synthesis route was demonstrated to produce hollow ceramic particles. Firstly, a stable sol was created using ATSB which was chelated by EAcAc. After peptization, the sol was combined with a physical blowing agent, a film forming agent, and a gelation agent then dispersed in a water-in-oil emulsion by homogenization. The emulsion was then heated under stirring causing the sol to gel while the blowing agent formed a hollow internal cavity. The chelated sol with its higher solid weight fraction resulted in walls sufficiently thick that particles survived washing with IPA and subsequent heating to 200° C. This demonstrated the efficacy of this synthesis approach to produce hollow particles with consistent wall thickness to particle diameter ratios without the need for internal templates. This lays the groundwork for scalable synthesis of hollow particles. Provided further development to improve the stability of the sol and generate monodisperse emulsions, the approach developed herein will undoubtedly enable the use of hollow particles in application relevant quantities, not just for mechanical metamaterials but also inverse photonic glasses, battery cathodes, and acoustic metamaterials, to name a few of the most important applications.

4. Mesoscale Modelling of Size-Effect Strengthened Syntactic Ceramic Foams

4.1. Abstract

While fabricating size-effect strengthened syntactic ceramic foams with uniform pore sizes remains a difficult experimental task, modeling the behavior of these foams could provide meaningful insight to narrow the design space, particularly as it pertains to the roles of pore dispersity and ligament size on the metamaterial strength. Here a computational framework is developed to generate realistic 2D and 3D syntactic foam geometries comprised of non-overlapping spherical pores and simulate their uniaxial tension/compression behavior, using the material point method; this model captures both the size-effects and the stochastic local variability (Weibull distributions) on the alumina strength. Although such analyses are generally performed with finite element methods, the material point method can more naturally simulate contact, fracture, and large deformation, as well as capturing strain rate effects. After the model is introduced, multiple simulations are performed to identify strength trends in syntactic ceramic foams as they relate to relative density, pore size and dispersity, and tension/compression asymmetries.

4.2. Introduction

In the computational work performed here, the goal was to investigate the role of pore size and dispersity by simulating the mechanical response of monodisperse and bidisperse syntactic ceramic foams. First, a thorough review of the existing literature on alumina strength was performed to better quantify the size-effects and Weibull statistics associated with alumina ceramics. Next, a material model to reproduce the effect of increasing strength with reductions in characteristic feature sizes and a method for determining

the maximal size of an idealized penny-shape crack that might reside at any point within an arbitrary voided volume were developed. This complete model of alumina strength was implemented in and simulated using the material point method (MPM) as executed by the GEOS-MPM software developed and maintained by Lawrence Livermore National Laboratory (LLNL), which includes methods for capturing large deformations, implicit contact, and fracture.

The material point method is a hybrid Lagrangian-Eulerian computational method in which a continuum body is discretized into Lagrangian particles, also called material points, that carry history-dependent state data. During each explicit timestep, particle data is interpolated to a static Eulerian background mesh where the derivatives are computed, and the mass and momentum constitutive equations are solved. The results are then re-interpolated to the particles, the background mesh reset and the timestep advanced as shown in Figure 4.1.

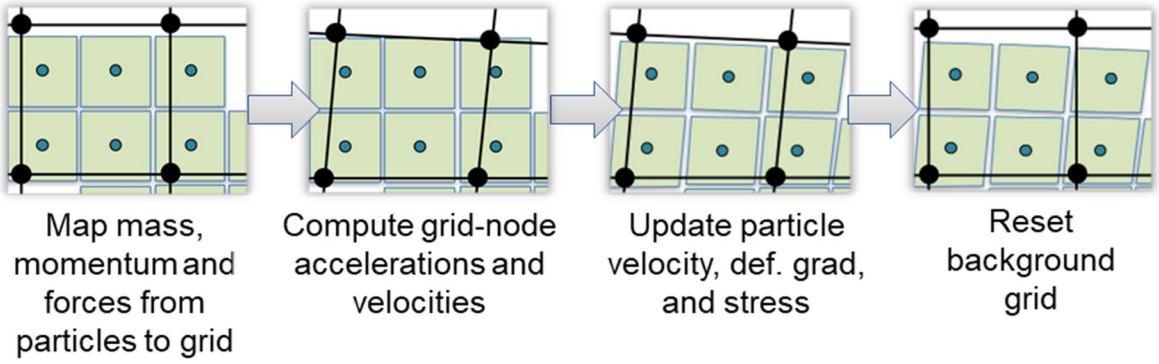

Figure 4.1. *Overview of a single timestep computation in the material point method.*

By performing calculations under small strains during each timestep and resetting the background mesh between timesteps, the MPM algorithm ensures that the mesh does not become entangled under large deformations, in contrast to the body-fixed meshes of Lagrangian finite element methods. Thus, remeshing is not required, preserving accuracy and eliminating costly and complex remeshing operations. Additionally, the solid bodies of the simulation are easily discretized into material points via voxelization, where material points are only created if their position is interior to the solid volumes. This avoids tedious

and complex mesh conditioning for irregular geometries typically required in Lagrange finite element methods.

In traditional MPM, particles are treated as lumped masses, which leads to noisy results and instabilities particularly in large deformations and particle-cell crossings events. The generalized interpolation material point (GIMP) method reduces noise by accounting for the finite special extent of each particle with smoother interpolation functions[116]. However, GIMP still suffers from instabilities during the crossing of particles between grid cells. Convected particle domain interpolation (CPDI) solves this instability by treating particle domains as deforming parallelograms for which the grid basis function is interpolated at the corners of the parallelogram or parallelepipeds by standard finite element interpolations. The GEOS-MPM software used for calculations herein utilizes CPDI[117]. GEOS-MPM also employs damage field gradient (DFG) partitioning which uses a kernel-based damage field[124]. The gradient of this field is used to dynamically repartition particles into contact pairs to model fracture and frictional contact implicitly without the need to explicitly track cracks or contact surfaces.

4.3. Experimental Al_2O_3 Strength Literature

Though size effects in ceramic materials are well known and consistently reported, individual studies are typically limited to specific processing conditions, size regimes and microstructures[28,37,55,118]. While an investigation of this phenomenon is of critical importance, such a thorough study is beyond the scope of this work. In its place, a thorough review of available literature on the strength of alumina was performed, and available data was normalized to obtain comparable effective Weibull volumes when not explicitly reported in the original work. A list of all consulted publications is shown in Table 4.1.

Stochastic variations in the strength of brittle materials is generally well captured by Weibull statistics, which is based on the weakest link theory[119]. According to this theory, the probability of failure, P_f, is given by:

$$P_f = 1 - \exp\left(-\frac{V_{eff}}{V_o}\left(\frac{\sigma}{\sigma_0}\right)^m\right) \tag{4.1}$$

where V_0 is a reference volume, V_{eff} is the effective volume determined by the state of stress within the component, σ_0 is the reference stress, σ is the applied stress and m is the Weibull scale parameter. The reference stress is usually determined by fitting the Weibull distribution to experimental strength data. For a small number of tests, determining the Weibull parameters is typically performed by linear regression. Equation (4.1) is rearranged into the following, which now takes the form of a linear equation in logarithmic space as:

$$\ln\left[\ln\left(\frac{1}{1-P_f}\right)\right] = m\ln(\sigma) - m\ln(\sigma_0) \tag{4.2}$$

The slope of the linear fit corresponds to m and σ_0 is computed from the value of the slope and intercept. This procedure requires the experimental strength data be sorted in ascending order and ranked to determine P_f. Mean ranking, $P_f = \frac{j}{N+1}$ where j is the failure order number and N is the total number of tests, is less accurate for skewed Weibull distributions. Therefore, median ranking is preferred. The median rank, Z, is used to compute the true probability of failure, P, using:

$$P = \sum_{k=j}^{N} \binom{N}{k} Z^k (1-Z)^{N-k} \tag{4.3}$$

Z is computed numerically by solving the equation for $P = 0.5$ for each value of j. Each value of Z is then used as the P_f for the strength data point corresponding to that value of j. Often, Bernard's less accurate

approximation, $P_f = \frac{j-0.3}{N+0.4}$ for the median rank, is used instead for its simplicity, but there are also other approximations not detailed here.

An alternative fitting procedure is maximum likelihood estimation (MLE), which defines an estimator, $\mathcal{L}$:

$$\mathcal{L} = \prod_{i=1}^{N} \left(\frac{m}{\sigma_0}\right)\left(\frac{\sigma_i}{\sigma_0}\right)^{m-1} exp\left[-\left(\frac{\sigma_i}{\sigma_0}\right)^{m}\right] \tag{4.4}$$

where σ_i are the experimental strengths for N tests. Both m and σ_0 are determined by differentiating $\mathcal{L}$ which respect to m and σ_0 and solving for the critical point that maximizes $\mathcal{L}$. This produces the following where m is determined numerically:

$$\frac{\sum_{i=1}^{N} \sigma_i^m \, ln\, \sigma_i}{\sum_{i=1}^{N} \sigma_i^m} - \frac{1}{N}\sum_{i=1}^{N} ln\, \sigma_i - \frac{1}{m} = 0 \tag{4.5}$$

Then σ_0 is computed by:

$$\sigma_0 = \left[\frac{1}{N}\sum_{i=1}^{N} \sigma_i^m\right]^{\frac{1}{m}} \tag{4.6}$$

To allow meaningful comparisons between Weibull distributions performed on samples of different sizes, the effective volume must be determined. The effective Weibull volume is calculated based on the stresses at failure using:

$$V_{eff} = \int_V \left(\frac{\sigma_{eq}}{\sigma_{eq,max}}\right)^m dV \tag{4.7}$$

where $\sigma_{eq,max}$ and σ_{eq} are the maximum and equivalent stress, respectively, at failure. For samples tested under uniform stress fields such as uniaxial tension or compression, $V_{eff} = V$. However, most ceramic testing methods use nonuniform stress fields, such as 3- or 4- point bending, ball-on-3-balls, and ball-on-ring. Depending on the test, the integral may be computed using either analytical elastic field equations or by postprocessing of finite element analyses.

For any multiaxial state of stress on a volume of material with off-diagonal stress tensor, $\bar{\sigma}$, components, we can find an equivalent description of the state of stress comprised only of diagonal components called the principal stress components, σ_p where $p = 1,2,3$ for each stress direction in three dimensions. The principal stress components are generally reported in the order of tensile magnitude of $\sigma_1 \geq \sigma_2 \geq \sigma_3$. Calculating these principal stress components is performed by computing the eigenvalues of $\bar{\sigma}$:

$$(\bar{\sigma} - \lambda I) = 0 \tag{4.8}$$

where the eigenvalues λ correspond to the principal stresses. For a test with multiaxial stresses, both $\sigma_{eq,max}$ and σ_{eq} are chosen according to a failure criteria such as normal stress criterion (NPS), empirical criterion of Richard (ECR), principal of independent action (PIA) and maximum principal stress (MPS)[120] and shown in Table 4.2 where τ_{II} is the shear stress, K_{IIC} is the fracture toughness of Mode II and Y_I and Y_{II} are the geometric constants for Modes I and II, respectively. The noted deviation between MPS and PIA is generally small. Therefore in the absence of reported values in the literature, the effective Weibull volumes have been calculated with MPS for simplicity[121]. As a final note, we have chosen to ignore contributions of surface flaws and roughness to the strength as we were not able to find a suitable

computational method to capture these features as a continuum given the scarcity of data, diversity of testing methods, and reported Weibull statistics. However, ceramics materials are known to be strongly influenced by surface flaws. In many common ceramic tests, the maximal stresses occur at the surface of the sample as in 3-point bending where surface flaws may be more influential than internal flaws on the strength. It has been found that polishing improves the flexural strength for ceramic components[122]. In the limit of small sizes approaching the theoretical strength and below the process zone of alumina (~1-3 μm)[123], a statistical description of strength is still applicable due to surface imperfections, that is no surface is atomically smooth. Here, we have chosen to capture this phenomenon, through a separate empirical means discussed later.

Table 4.1. *Summary of literature reported mechanical properties of Al_2O_3. Effective Weibull volumes were determined from extracted literature data using the MPS criterion in the absence of reported values.*

Source	**Testing Method**	**Fabrication Process**	**Weibull Parameters**		
			Effective Volume (V_0, mm^3)	**Modulus (m)**	**Scale Parameter (σ_0, MPa)**
Gross et al.[124]	Ball-on-3-Balls Ring-on-Ring	Commercial Manufacturer	2.8×10^{-5}-0.6	12-19	244-564
Fu et al.[125]	3-Point Bending	Dry Pressing/Cold Isostatic Pressing/Sintering	3.2-29	4-14	186-309
Rontu et al.[126]	Bulge Test	Atomic Layer Deposition	2.4×10^{-6}- 3.5×10^{-6}	28-55	870-2230
Feilden et al.[127]	3-Point Bending	Particles	1.3×10^{-13}- 3.8×10^{-13}	3.7	5300
Berdova et al.[128]	Bulge Test	Atomic Layer Deposition	4.5×10^{-6}- 4.7×10^{-6}	14.7-15.4	2100-3100
Philips et al.[129]	Cantilever Bending	Inkjetting			
Michálek et al.[130]	Ball-on-3-Balls	Injection Molding	3.2×10^{-4}	11.8	1257
Lupercio et al.[131]	Ball-on-Ring	Bulk Consolidation	2.9	14.3	289
Žagar et al.[132]	Bending	Fibers	7×10^{-9}	7.2	5300

Han et al.[133]	3-Point Bending	Pressureless Sintering Hot Pressing Oscillatory Pressure Sintering	0.2-1.6	9.6-28.9	
Krell et al.[134]	3-Point Bending	Gelcasting and Pressureless Sintering Pressure filtration, Gelcasting and Pressureless Sintering Freeze Drying, Cold isostatic pressing and Sintering			
Cantonwine[135]	Uniaxial Tension	Fibers	2.8×10^{-3}	7-11	2510-3370
Wang et al.[136]	Loop Test	Whiskers			
Lankford et al.[137]	Uniaxial Compression	Bulk rods	38	10.1	3679
Kuroyanagi et al.[138]	Nanoindentation	Single Crystal Particles			
Bansal et al.[118]	3-Point Bending 4-Point Bending	Isostatic Pressing of Spray Dried Powder	410 -5.1×10^{4}	11-34	253-413*
Broutman et al.[139]	Pressurized Cylinder with Axial Load	Sintered			
Danzer et al.[140]	Ball-on-3-Balls	Discs	2.1×10^{-5}-0.20	12	363-668
Jeong et al.[141]	Ball-on-3-Balls	Powder consolidation and sintering	0.11	7.0	442

Table 4.2. *Equivalent stresses for various multiaxial failure criteria.*

Multiaxial Failure Criterion	**Definition**
Normalized stress criterion (NSC)	$\sigma_{eq} = \frac{1}{2}\left[\sigma_n + \sqrt{\sigma_n^2 + 4\tau_{II}\frac{K_{IC}}{K_{IIC}}\left(\frac{Y_{II}}{Y_I}\right)^2}\right]$
Principal of independent action (PIA)	$\sigma_{eq} = (\sigma_1 + \sigma_2 + \sigma_3^m)^{\frac{1}{m}},\ \ \sigma_1 > 0$
Maximal Principal Stress (MPS)	$\sigma_{eq} = \sigma_1, \qquad \sigma_1 > \sigma_2 \geq \sigma_3$

The primary challenge here is the diversity of reported material which spans different testing methods, sample geometries, microstructures, and sizes. For these reasons, the results obtained from this model are intended to convey general trends in the size effect of randomly packed porous ceramics, rather than quantitative estimations of experimental performance. Nonetheless, there are several clear observations: (i) samples of all sizes have statistical variations in strength, (ii) the strength plateaus at the smallest volumes near the theoretical strength of the material, and (iii) samples with critical dimensions below the critical Weibull flaw size have enhanced strength corresponding to the maximal flaw size that can physically reside in the specimen[28].

4.4. Particle Packing

The core feature of syntactic foams is that pores do not overlap; therefore, we can reformulate the generation of the pore geometries as a problem of particle packing, like those for computational investigations of granular media, e.g., non-penetrating hard particles. Several approaches to packing particles have been demonstrated, falling into one of four families: the discrete element method (DEM)[142], molecular dynamics (MD)[143], random sequential adsorption (RSA)[144] and the Lubachevsky-Stillinger (LS) algorithm[145]. Packings generated here also needed to be periodic in all directions for suitable boundary conditions to be applied to approximate the response of a bulk material. Additionally, the packing method had to be computationally efficient and capable of generating packings at or near the random close packing limit. While DEM is advantageous because it can be applied to arbitrary particle meshes and hence shapes, it is difficult to obtain jammed packings which have triply periodic boundaries and packing fractions near the packing limit. Likewise, MD approaches typically rely on force field approximations to hard spheres which may permit slight overlap between adjacent particles in the final packing. RSA is well suited for arbitrary particle shapes and periodic boundaries but struggles to reach packing limits within computationally reasonable times since particles are added serially via random trial positions. In the LS

algorithm, an arbitrary domain is populated initially by uniformly distributed points with zero radius. During packing, the particle radii grows while interparticle and particle-wall collisions, in the case of hard wall boundaries conditions, are resolved by inelastic collisions. The packing algorithm is terminated when either the desired packing fraction is reached or the particles become jammed. We found the LS algorithm most suitable here, namely, it supports triply periodic boundaries for packing of 2D and 3D pore structures, readily reaches the random close packing limit with volume fractions of approximately 0.63-0.64[146] for monodisperse particles and is computationally efficient, all while maintaining flexibility of the underlying domain and pore sizes. LS packing of spherical particles was performed via a custom modified code from Skoge et al.[147].

Figure 4.2 shows the results of mono- and bidisperse packings generated with the LS algorithm. As can be seen from Figure 4.2a, the monodisperse packing converges to the random close packing limit at 50 pores. In Figure 4.2b, bidisperse random packings were generated with 10 large pores for particle size ratios of large to small of 2, 3, and 5 for different numbers of small pores. In the limit of an infinite ratio of large to small particle sizes, the maximal packing fraction for bidisperse spherical particles is approximately 86%. For small ratios, there exists an optimal number of small pores which maximizes the packing fraction, which is 55, 110, and 450 small pores for ratios 2, 3, and 5 respectively. 2D packings were also performed with the LS algorithm, but the reduced dimensionality results in maximal packing fractions over 80% with hexagonal symmetry. Therefore, 2D packings which were used to examine trends too computationally intensive to perform in 3D, were generated by terminating the packing algorithm once the packing fraction of the corresponding 3D pack of the same particle dispersity and relative sizes was reached. This prevented packings from becoming crystallized while maintaining pore size distributions.

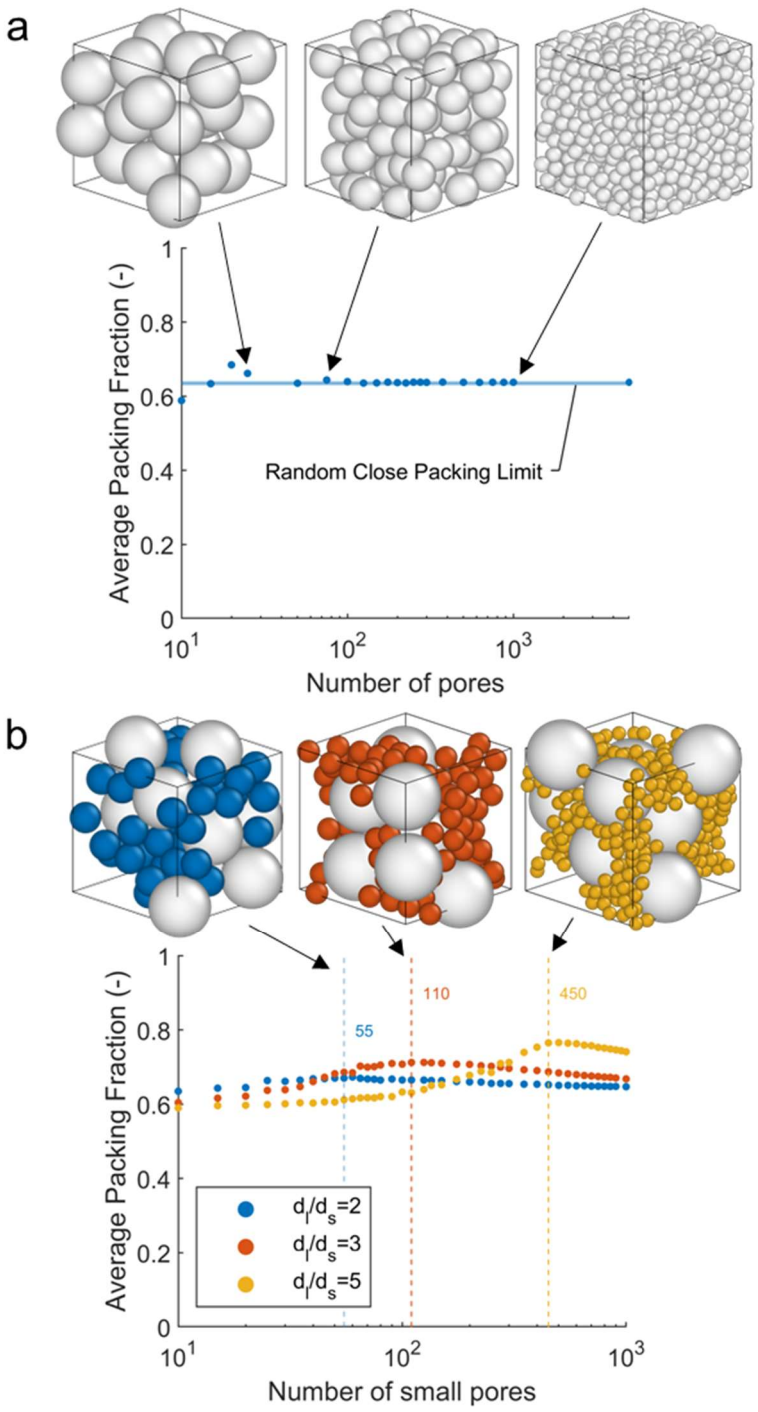

Figure 4.2. *Packing fraction of monodisperse (a) and bidisperse with 10 larger pores (b) particle systems in 3D. Each data point in the 2D and 3D packings represents the average of 25 and 10 individual packing simulations, respectively.*

After generating particle packings, the desired relative density of monodisperse syntactic foams is obtained by scaling the particle radii by s_R given by:

$$s_R = \left(\frac{1-\bar{\rho}}{p_f}\right)^{\frac{1}{d}} \tag{4.9}$$

where $\bar{\rho}$ is the desired relative density, d is the dimensionality (e.g., 2 or 3), and p_f is the packing fraction of the granular particles. Then the minimum ligament size, l_{min}, which corresponds to the thickness of two contacting particle shells, is enforced by scaling the domain by s_D:

$$s_D = \frac{l_{min}}{2s_R(1-r)} \tag{4.10}$$

where r is the radius of the particles in the original packing. For 2D bidisperse systems, the process is identical except that the ratio of wall thickness, $\alpha = \frac{t_S}{t_L}$, between two contacting larger particles and two contacting smaller particles is also tunable. When α = 1, the thickness of the wall between two contacting large pores and the two contacting small pores is identical and the radius scale for large ($s_{R,L}$) and small ($s_{R,S}$) particles is given by:

$$\begin{aligned} s_{R,L} &= \frac{\alpha n_s\sqrt{\pi}(r_L\alpha - r_S) + \sqrt{\bar{\rho}(n_L + \alpha^2 n_S) - n_L n_S \pi(r_S^2 - 2\alpha r_L r_S + \alpha^2 r_L^2)}}{r_L\sqrt{\pi}(n_L + n_S\alpha^2)} \\ s_{R,S} &= 1 - \alpha\left(\frac{r_L}{r_S}\right)\left(1 - s_{R,L}\right) \end{aligned} \tag{4.11}$$

where n is the number of pores in the RVE, and L and S subscripts denote terms for large and small pores, respectively. The domain size is still scaled by Equation (4.10), but s_R must be replaced by the scaling

factor for large or small particles depending on which ligament size should be restricted. This has the effect of determining whether hierarchy is introduced by adding smaller particles to form smaller ligaments or by introducing larger particles retaining the same minimum ligament size as those of the monodisperse foams. If instead α is equal to the ratio of the small to larger particle diameters, then the previous relation for s_R for monodisperse foams is recovered exactly and $s_{R,L} = s_{R,S}$.

4.5. Weibull Variability

Weibull variability is incorporated by applying a strength scale sampled from the Weibull distribution to particle groups defined by a Voronoi tessellation over the simulation domain. For a set of predefined points in space, a Voronoi tessellation is the partition of space such that each cell encloses all points residing closest to a given predefined point. Voronoi tessellations have broad significance in problems such as determining nearest neighbors, graph networks and modelling polycrystalline microstructures. To ensure Voronoi cells have relatively uniform volumes, random Voronoi cell centers are generated by Poisson disc sampling.

Poisson disc sampling is an efficient computational procedure to generate points in arbitrary dimensions, d, while enforcing a minimum spacing, r_{min},. In this procedure, a domain is discretized into a uniform grid with a cell size equal to $r_{min}/\sqrt{d}$. A random initial point is chosen within the domain and added to lists of seed and output points. New points are added iteratively by selecting a seed point from the list and generating new candidate points in the neighborhood of that seed point via a random displacement vector with minimum magnitude r_{min}. The grid size is chosen such that only the grid cells immediately adjacent to the cell corresponding to the candidate point must be checked. If no points belonging to the list of output points is within r_{min} of the candidate point, it is added to the list of seed and output points and its index in the list of output points is added to its occupied grid cell for future lookup. When N consecutive candidate points are rejected, the seed point is discarded from the list of seed points and a new seed point

is selected. The process is repeated until the list of seed points is empty. Advantageously, this algorithm can also be performed with periodic boundary conditions.

Each Voronoi cell size is approximately 6 cells, or 12 particles, across, which was found sufficient to enable realistic crack nucleation and propagation following the failure of a single particle[148]. The strength scale, s, for each Voronoi cell is initialized by first sampling a uniform random variable, R_V, and then computing the cell strength based on:

$$s = \frac{\sigma}{\sigma_0} = \left(-\frac{V_0}{V_V}\ln(1 - R_V)\right)^{\frac{1}{m}} \tag{4.12}$$

where V_V is volume of the Voronoi cell internal to the material[149,150]. Without the tessellation when particle strength is initialized individually according to the Weibull distribution, single weak particles are generally surrounded by many strong particles resulting in artificial strengthening. Additional details on this method can be found in Homel et al.[148].

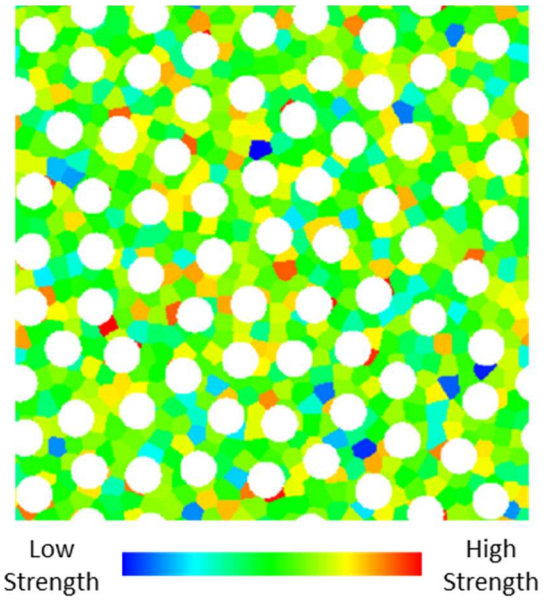

Figure 4.3. *Weibull distribution of material point strength scales in a 2D syntactic foam. The strength scales of nearby material points are grouped by Voronoi cells to correctly resolve crack nucleation and tip stresses.*

4.6. Flaw Field

In periodic architected materials, size-effects in the strength of brittle materials are observed when the characteristic dimensions are small enough that they restrict the maximum size of a flaw. For these regular structures, the characteristic feature size is trivial, i.e., the diameter of a beam or the thickness of a plate or shell. However, syntactic foams are characterized by a distribution in wall thicknesses and pore interstitial sites, depending on the arrangement of pores. Therefore, a method to determine the characteristic dimension within an arbitrarily voided solid is needed. In the treatment herein, this characteristic dimension corresponds to the maximum radius of an idealized penny-shaped crack that might span a particular point within the solid; this mapping has been termed the "flaw field".

Generating the flaw field involves three steps, as shown in Figure 4.4. First, the distance field is computed by calculating the distance of each point in the domain to the nearest pore surface. Points within pores are ignored since they constitute the void phase. For spherical pores calculating the distance field is trivial. However, in principle the distance field for any pore or surface shape could be computed using ray marching. Next, saddle points are identified in the distance field by finite differences. The collection of saddle points is termed the critical points. Lastly, a watershed algorithm propagates the distance field values of each critical point to the rest of the field. This process is illustrated in two dimensions in Figure 4.4 in which its possible to see that the largest cracks are restricted to the interstitial sites between neighboring pores (black circles). The same method is also easily applied in three dimensions.

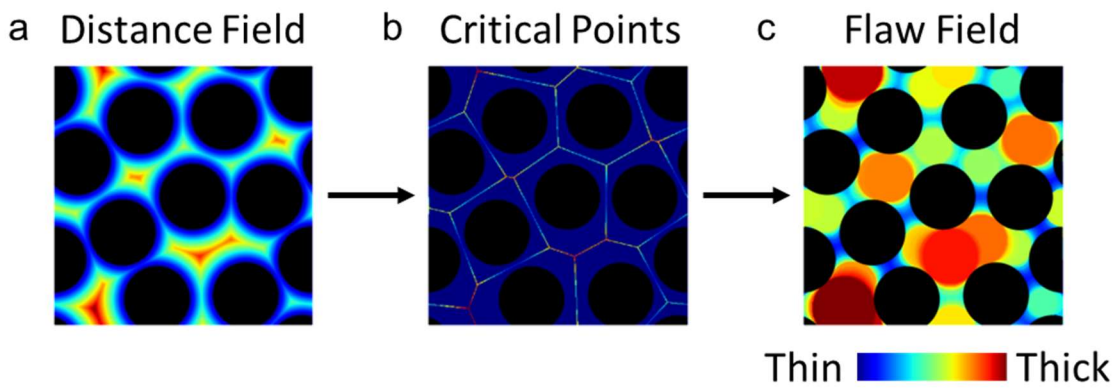

Figure 4.4. *Flaw field generated from arbitrary 2D pores by computing the distance field (a), identifying critical points by finite differences (b), and watershed propagation of critical points (c).*

4.7. Material Model

The material model described herein accounts for the asymmetry of tensile and compressive failure of ceramics under multiaxial stress states, particle damage, a frictional strength cutoff, stochastically governed strength, and size-effects from shrinking features. Although the reported mechanical properties of alumina are diverse and available for a myriad of testing methods, microstructures, processing, grain sizes, and surface roughness, etc., those features were ignored in favor of a minimally complex material model in the interest of generality.

For arbitrary loading, the stress intensity of a crack is divisible into three orthogonal modes shown in Figure 4.5: opening, in-plane shear, and anti-plane (or out-of-plane) shear.

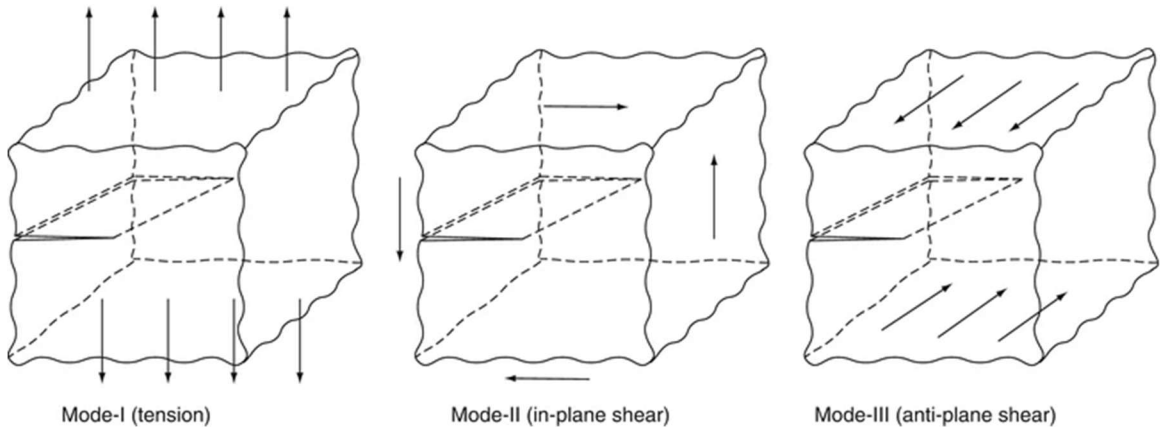

Figure 4.5. *Schematic of crack loading modes[151].*

In general, crack shapes are highly irregular, but generally modelled as idealized penny-shaped features (see Figure 4.6) in three dimensions wherein a unit normal describes the orientation and a radius defines the size.

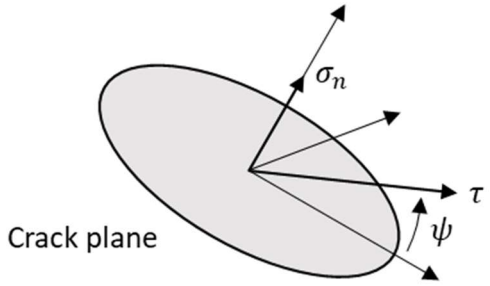

Figure 4.6. *An idealized penny-shape crack arbitrarily oriented in the material and loaded by normal (σ_n) and shear (τ) stresses in the reference frame of the crack.*

For a penny-shaped crack arbitrarily oriented and loaded, the stress intensity for each mode is described by:

$$K_I = 2\sigma_n\sqrt{\frac{a}{\pi}}$$
$$K_{II} = \frac{4\tau}{(2-v)}\sqrt{\frac{a}{\pi}}cos\,\psi \tag{4.13}$$

$$K_{III} = \frac{4(1-v)}{(2-v)}\tau\sqrt{\frac{a}{\pi}}\sin\psi$$

where K is the stress intensity, $I - III$ denote the crack mode, σ_n is the stress normal to the crack, τ is the shear stress in the plane of the crack, ψ is the angle of shear stress in the plane of the crack with respect to the crack coordinates and v is the Poisson's ratio[152]. Assuming an ideally brittle material (no plastic work occurs at the crack tip during extension), an equivalent stress intensity is defined using the G-criterion as:

$$K_{eq}^2 = K_I^2 + K_{II}^2 + \frac{E}{2G}K_{III}^2 \tag{4.14}$$

where E is the Young's modulus and G is the shear modulus. Crack extension occurs when the equivalent stress intensity exceeds the local fracture toughness, K_{IC}. If cracks are assumed to be non-interacting and uniformly distributed throughout the constituent material, then the failure strength is taken as the stress at which a critically oriented crack propagates. Unfortunately, an implementation of mixed mode explicitly tracked cracks is too complex and expensive for the framework here. It is also not clear that explicitly tracking cracks is feasible given the large size disparity between larger scale features and micron size or smaller cracks.

However, even in mixed mode loading, we find the size-effect to still scale proportionally as:

$$\sigma_f = \frac{\gamma^*}{\sqrt{a}} \tag{4.15}$$

where σ_f is the fracture strength, γ^* is a free parameter that captures the fracture toughness, geometry and orientation of the population of cracks in a ceramic material and can be tuned to match experimental data.

To model the failure surface under triaxiality, a hypoelastic, i.e. a rate-independent constitutive relation for which the Cauchy stress depends only on the history of deformation, isotropic material model

is chosen, only requiring 11 input parameters: Young's modulus (E), Poisson's ratio (v), density (ρ), reference tensile (Y_{t_0}), triaxial strength ratio (Γ), maximum strength cutoff (Y_{max}), Weibull scale parameter (m), Weibull reference volume (V_0), non-dimensional stress intensity coefficient (γ^*), crack speed (v_{crack}) and granular coefficient of friction (μ). Both Weibull and geometric size-effects are introduced by scaling the particle strengths within a Voronoi cell by a non-stochastic scalar value, s_0, according to:

$$s_{flaw} = \frac{\gamma^*}{\sqrt{a}}, \qquad s_{Weibull} = \left(\frac{V_0}{V_V}\right)^{\frac{1}{m}}$$
$$s_0 = \min\left[\max\left[s_{weibull}, s_{flaw}\right], s_{max}\right] \tag{4.16}$$

where a is the flaw size taken from the flaw field, s_{max} is the maximum scaling parameter determined from $\frac{Y_{max}}{\Gamma Y_{t_0}}$, V_V is the volume of the Voronoi cell interior to the solid, V_0 is the Weibull reference volume and m is the Weibull scale parameter. The value of a is taken from the value of the flaw field at the center of each Voronoi cell. If the Voronoi cell center lies outside the solid region, then the value of the flaw field at the nearest solid interior point is used instead.

Given that strength is observed to follow Weibull statistics even in the limit of small volumes, an empirical approach is adopted that maintains a constant Weibull scale parameter across sizes and thus a constant ratio between the standard deviation and mean of the strengths. Size-effects related to small features and Weibull statistics are introduced solely by scaling the Weibull reference strength with s_0. Stochastic perturbations of local strength are then generated by sampling a uniform random variable, R_v and computing the final scaling value, s, for particles interior to each Voronoi cell using:

$$s = s_0(-\ln(1 - R_V))^{\frac{1}{\mathrm{m}}} \tag{4.17}$$

Interestingly, if the strength were instead modelled by truncating at the flaw field value a fixed distribution of crack sizes, back computed from the Weibull distribution of a macroscopic component, the mean strength of these two approaches would coincide almost exactly with the exception that the standard deviation of strength would approach zero in the limit of small feature sizes. This is not observed in any experiment. For brevity further discussion of this is excluded, but this fact is easily derived.

Because the problem of fitting a nonlinear failure surface to sparse experimental data is not a well-defined problem, fitting was performed visually to best capture general trends. We note that the results here are intended to provide general trends in material behavior rather than exact predictions of experiments. The selected material properties for a model alumina constituent material are list in Table 4.3. A Weibull modulus of 12 was chosen from the work of Danzer et al.[140] which characterized the effect of volume on the Weibull scaling over eight orders of magnitude in alumina using ball-on-3-balls test and includes analysis of principal stresses in the Weibull treatment. The maximum compressive strength was taken from rule of thumb ($\sim E/30 - E/10$) calculations of the theoretical strength of materials, this value also closely matches reported values from loop tests performed on α-Al_2O_3 whiskers by Wang et al.[136]. The Young's modulus, Poisson's ratio and density were taken from standard values for alumina ceramics. The Weibull volume was arbitrarily chosen since it only serves as a reference point and the Weibull reference strength was adjusted to best match experimental trends. The crack velocity did not play a strong role given that the strain rates utilized here approximated quasistatic loading but was selected as the transverse wave velocity given by $\sqrt{G/\rho}$. The triaxial strength ratio, Γ was taken from the ratio the mean of the compressive strength from Lankford et al.[137] and the mean tensile strength of the fit which agreed with results from Broutman et al.[139]. The complete model of the size-effect is shown in Figure 4.7 where the mean tensile strength is plotted against alumina literature data, the flaw radius, and the effective Weibull volume.

Table 4.3. *List of relevant simulation parameters.*

Parameter	**Description**	**Value**

E	Young's modulus	400 GPa
v	Poisson's ratio	0.26
ρ	Density	3.987 g/cm^3
Y_{t_0}	Uniaxial unconfined reference tensile strength	0.3
Γ	Triaxial Extension to Compression Strength Ratio	8
Y_{max}	Max compressive strength	42 GPa
m	Weibull modulus	12
V_0	Weibull reference volume	1 mm^3
γ^*	Non-dimensional stress intensity coefficient	0.036 mm$^{1/2}$
μ	Coefficient of friction	0.25
v_{crack}	Crack speed	6.3 mm/μs

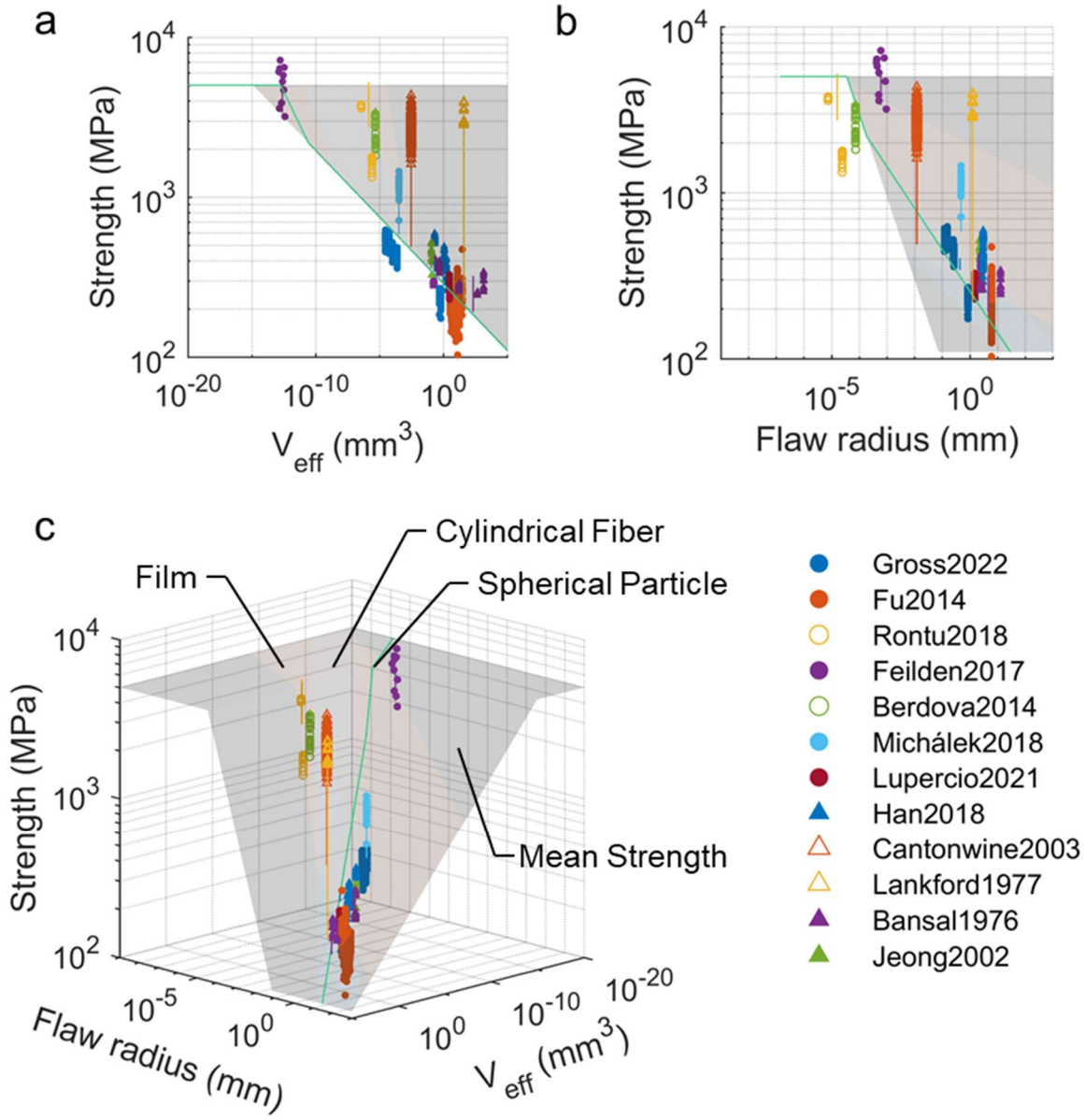

Figure 4.7. *Literature tensile strength data corrected for effective Weibull volume and plotted against the mean tensile strength of the size-effect strengthened model. Hollow markers were not considered in the fit of the mean strength but are included for visual reference because they represent compressive data, amorphous phases, or anomalous strength due to specific processing.*

The failure surface is modulated by scaling the uniaxial tensile and compressive strengths according to:

$$Y_t = \min\left[sY_{t_0}, \frac{Y_{max}}{\Gamma}\right], \qquad Y_c = \min\left[sY_{c_0}, Y_{max}\right] \tag{4.18}$$

Damage is tracked by an isotropic scalar variable, D, which is used to interpolate the failure surface between the undamaged material and the frictional strength cutoff of a granular material. When the maximum shear stress in a particle exceeds the shear strength for that stress state, damage is evolved using a time-to-failure approach[153] given by:

$$D^{n+1} = \min\left[1.0, D^n + \frac{dt}{c_f}\right] \tag{4.19}$$

where dt is the timestep and v_{crack} is the crack propagation speed set here as the shear wave velocity in alumina, approximately 6.3 mm/μs. Given any particle state of stress and damage, the shear strength, Y_0, is determined according to:

$$Y_0\left(p, D, Y_c, Y_{t_0}\right) = \begin{cases} 0, \;\; p \le p_{min} = \dfrac{-2Y_cY_t}{3(Y_c - Y_t)} \\ Y_1\left(p, D, Y_c, Y_{t_0}\right), \;\; p < \dfrac{Y_c}{3} \\ Y_2\left(p, D, Y_c, Y_{t_0}\right), \quad \dfrac{Y_c}{3} < p < \dfrac{Y_{max}}{\mu} \\ Y_{max}, \quad p > \dfrac{Y_{max}}{\mu} \end{cases} \tag{4.20}$$

$$Y_1 = \frac{(3 + d(\mu - 3)Y_c) + (d(\mu + 3) - 3)Y_{t_0}}{Y_c + Y_{t_0}}\left(\frac{p - 2(d-1)Y_cY_{t_0}}{3\left(Y_c + Y_{t_0}\right)}\right) \tag{4.21}$$

$$Y_2 = \frac{Y_{max} - Y_c}{\frac{Y_c}{3} - \frac{Y_{max}}{\mu}}\left(\left(\frac{Y_c}{3} - \frac{Y_{max}}{\mu}\right) + \left(\frac{Y_{max}}{\mu} - p\right)\left(\frac{\frac{Y_{max}}{\mu} - p}{\frac{Y_{max}}{\mu} - \frac{Y_c}{3}}\right)^{\beta} + \frac{Y_c}{3}\left(\frac{\frac{Y_c}{3} - \frac{Y_{max}}{\mu}}{Y_c - Y_{max}}\right)\right) \tag{4.22}$$

$$\beta = \frac{Y_1'\left(p, D, Y_c, Y_{t_0}\right)\left(\frac{Y_c}{3} - \frac{Y_{max}}{\mu}\right) - Y_c + Y_{max}}{\frac{Y_c}{3} - \frac{Y_{max}}{\mu}}$$

which are composed of a linear region, Y_1 and a nonlinear smooth interpolation, Y_2, between the linear region and maximum theoretical strength plateau. Anisotropy in the shear plane is captured by a third invariant dependence[154] that depends on the Lode angle (θ) which reduces the strength in triaxial compression (TXC) relative to triaxial extension (TXE) by:

$$\theta = \frac{1}{3}\arcsin\left[\frac{-J_3}{2}\left(\frac{3}{J_2}\right)^{3/2}\right] \tag{4.23}$$

$$\Gamma = \frac{4\beta^2(1-\psi^2) + (2\psi - 1)^2}{(2\psi - 1)\sqrt{4\beta^2(1-\psi^2) + 5\psi^2 - 4\psi + 2\beta(1-\psi^2)}}$$
$$\psi = \frac{1}{1 + \frac{1}{3}\frac{\partial Y_0}{\partial p}}, \qquad \beta = \cos\left(\theta + \frac{\pi}{6}\right) \tag{4.24}$$

where J_2 and J_3 are the stress invariants. The shear strength for a particle composed of partially damaged material is given by:

$$Y = \frac{1}{\Gamma}[(1-D)Y_0 + D\,\min[Y_0, \mu p]], \qquad p > (1-D)p_{min} \tag{4.25}$$

where D is used as a weighting between the undamaged shear strength and the frictional granular strength scaled by the triaxial compression to extension strength ratio. The shear strength versus pressure is shown in Figure 4.8 prior to third invariant scaling for different damage levels and strengths scales.

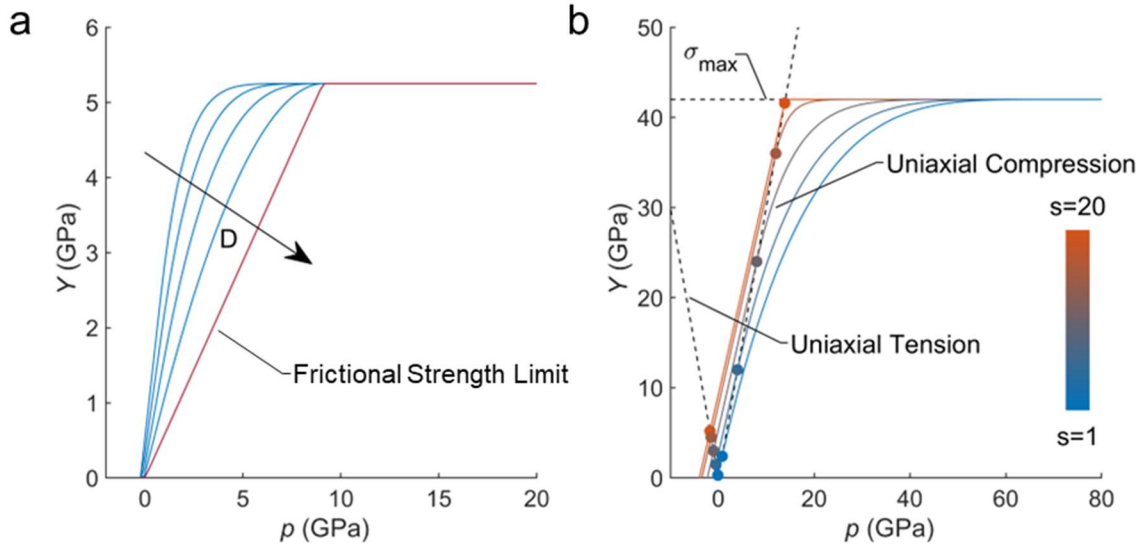

Figure 4.8. *Failure surface evolution with damage (a) and strength scaling (b) plotted in the pressure-shear plane.*

The complete failure surface with third invariant dependence is visualized in the principal stress space for three strength scales in Figure 4.9.

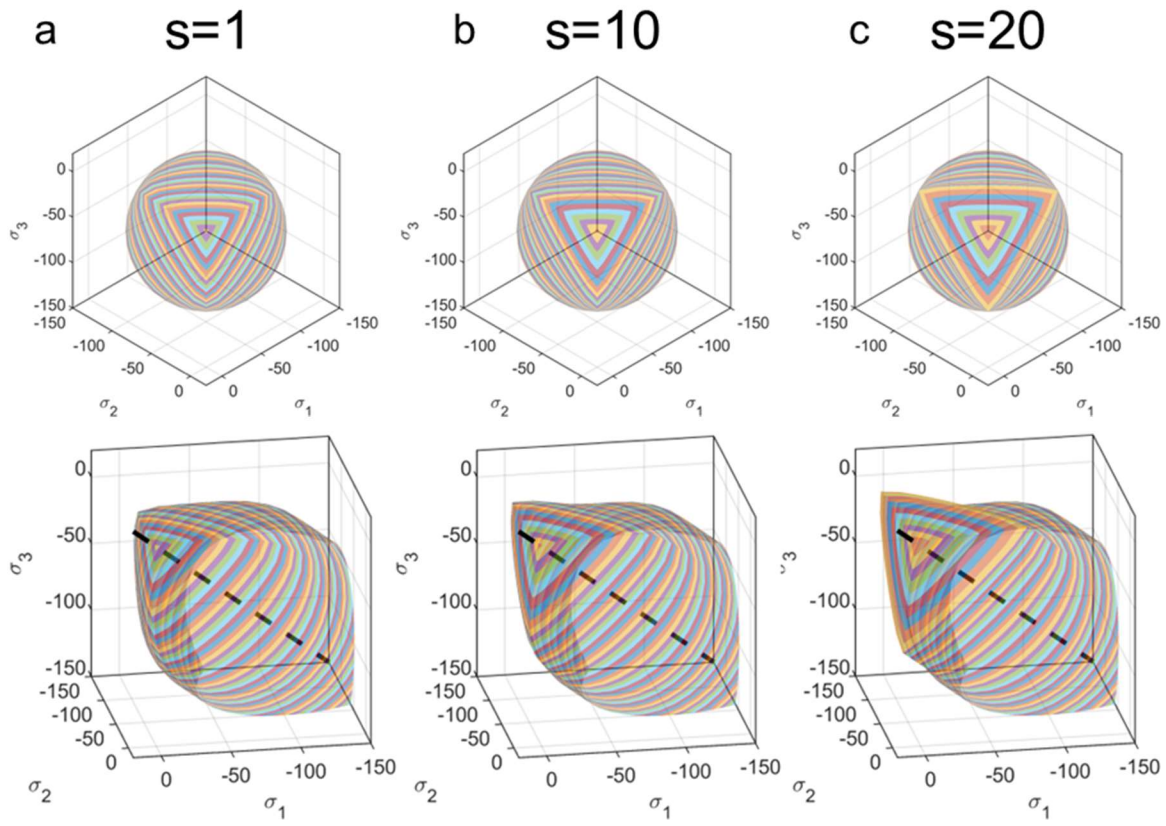

Figure 4.9. *Visualizations of failure surface in principal stress space for 3 scaling values: 1 (a), 10 (b), and 20 (c).*

The resulting failure surface approximates Mohr-Coulomb failure at low pressure and high-pressure ductile failure. Mohr-Coulomb failure is defined by a series of linear equations that form a cone in principal stress space given by the equations:

$$\pm\frac{(\sigma_1-\sigma_2)}{2}=\frac{(\sigma_1+\sigma_2)}{2}\sin(\phi)+c\cos(\phi)$$
$$\pm\frac{(\sigma_2-\sigma_3)}{2}=\frac{(\sigma_2+\sigma_3)}{2}\sin(\phi)+c\cos(\phi) \quad (4.26)$$
$$\pm\frac{(\sigma_3-\sigma_1)}{2}=\frac{(\sigma_3+\sigma_1)}{2}\sin(\phi)+c\cos(\phi)$$

where σ_1, σ_2, and σ_3 are the principal stresses, ϕ is the angle of internal friction and c is the cohesion. It has been found to empirically predict brittle failure of rock and ceramic like materials failure under multiaxial stresses.

4.8. Material Point Method

Simulations were carried out in the GEOS-MPM software package maintained by LLNL using convected particle domain interpolation (CPDI)[117,155]. The material point method has several advantages over Lagrangian finite element methods specifically facile large deformation, simple voxelization of input geometries, fracture, frictional and implicit contact, and high strain rate. Contact, fracture, and friction are accomplished using damage field gradient partitioning[153]. Here computations are performed using an explicit timestep determined automatically by the software. Quasistatic conditions are obtained by a sufficiently slow strain rate, here denoted in multiples of the number of trips an elastic wave traverses along the indentation direction in the bulk material. The strain rate, $\dot{\varepsilon}$, is computed from the P wave speed, v_P, for isotropic media given by:

$$v_P = \sqrt{\frac{K + \frac{4}{3}G}{\rho}} \tag{4.27}$$

where K is the bulk modulus, G is the shear modulus and ρ is the density. Thus, the strain rate is calculated by:

$$\dot{\varepsilon} = N\frac{v_P}{y} \tag{4.28}$$

where N is the number of wave transits and y is the length of the domain along the indentation direction. A minimum of 400 wave transits was found to be sufficient for quasistatic loading based on the convergence of strength as shown in Figure 4.10a. Similarly, convergence in strength was observed for 2D and 3D monodisperse foams with 75 and 50 pores per representative volume element (RVE), respectively.

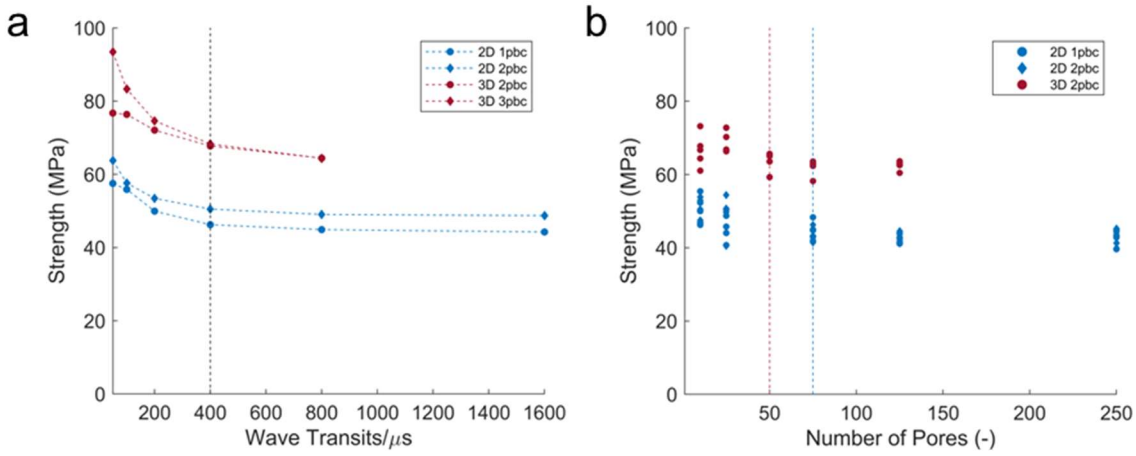

Figure 4.10. Optimization of quasistatic strain rate based on the number of elastic wave transits across the deformed direction for monodisperse geometries with $\bar{\rho} = 0.7$ and 10 pores in 2D and 3D simulations with and without periodic boundaries in the direction of deformation (a) and number of pores in a RVE for 2D and 3D simulations deformed with a strain rate equivalent to 400 elastic wave transits (b).

4.9. Computational Results

Initial computational investigations began by simulating a two dimensional monodisperse foam with 75 pores performed in plane strain. To control for variations in pore location all simulations were run using the same particle packing. Only the Weibull tessellations were different between relative densities. The foam geometry was simulated with different minimum ligament sizes of 1 mm, 100 µm, 10 µm, 1 µm and 100 nm and subjected to displacement controlled confined uniaxial tension for relative densities of 0.5, 0.6, 0.7, 0.8, and 0.9. While lower densities up to the random packing limit, e.g., 0.63-0.64, are feasible in monodisperse systems, the computation expense growths exponentially by enforcing a minimum of 12

material points across the smallest possible ligament. The strengths of these foams are plotted in Figure 4.11. Except for the foams with $\bar{\rho} = 0.5$ and 0.6 with a minimum ligament size of 1 μm, the scaling behavior is seen to be identical. The greatest enhancement in strength occurs between minimum ligament sizes of 10 and 1 μm where the size of the maximum flaw begins to be restricted by the ligament size. In the highest relative densities of the 1 μm and 100 nm minimum ligament sizes, there was no initial advantage to reducing the size of ligaments. However, in the lowest relative densities, the strength was notably lower deviating from the scaling trend observed in all other simulations.

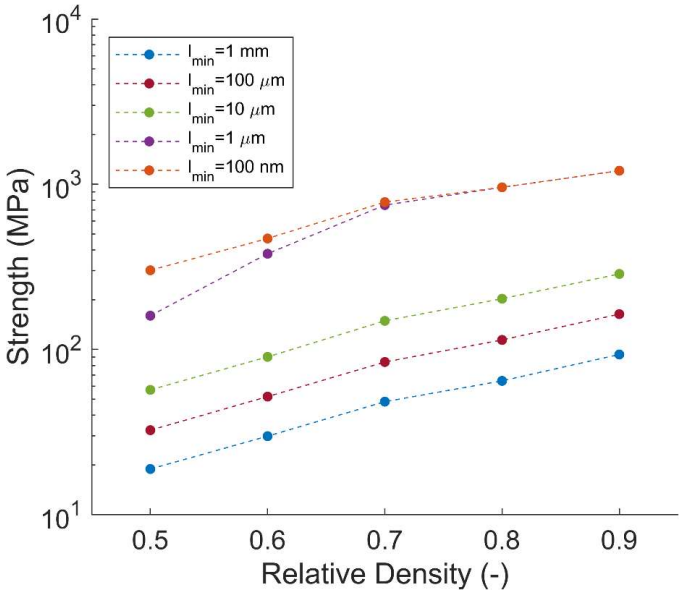

Figure 4.11. *Scaling behavior of monodisperse 2D foams with 75 pores and minimum ligament sizes 1 mm, 100 μm, 10 μm, 1 μm, and 100 nm.*

To examine the deviation in strength for the lowest relative density foams with 1 μm minimum ligament sizes, the strength scale distributions of particles for $\bar{\rho} = 0.5$ and 0.7 were plotted in Figure 4.12 for comparison. This deviation is clearly linked to changes in the strength scale distribution because of geometric differences arising from changes in the radius of curvature between different size pores. In the case of $\bar{\rho} = 0.7$ with minimum ligaments of 1 μm, the strength distribution coincides nearly perfectly with that of the 100 nm minimum ligament simulation. By contrast, the long right-side tail in strength

distributions of $\bar{\rho} = 0.5$ with minimum ligaments of 1 μm clearly indicates that there is some enhancement of ligament strength from shrinking ligaments, but ultimately less so in interstitial sites.

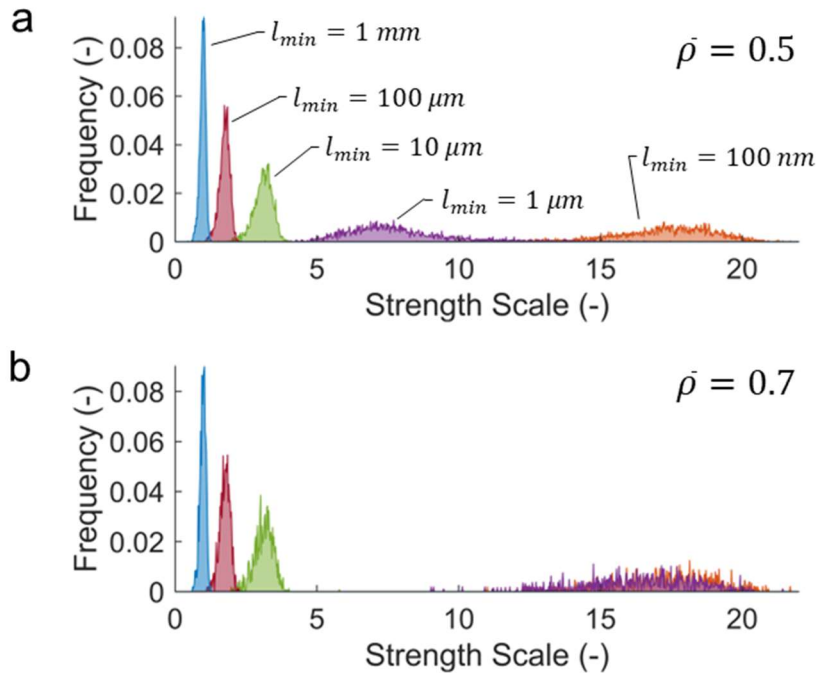

Figure 4.12. *Strength scale distributions for monodisperse 2D foams with 75 pores for* $\bar{\rho} = 0.5$ *(a) and* $\bar{\rho} = 0.7$ *(b).*

While 3D simulations were far more computationally expensive, the 2D results were validated by simulating three-dimensional monodisperse foams for minimum ligament sizes, 1 mm and 1 μm. The results are shown in Figure 4.13. The 2D simulations underestimate the strength of the 3D monodisperse foams and the general reduction in strength is more pronounced in the 3D foams. However, like the 2D foams, scaling behavior did not seem to deviate between the two sizes examined here. Nonetheless, decreasing the ligament size by three orders of magnitude in both the 2D and 3D cases yielded approximately an order of magnitude improvement in strength between minimum ligament sizes of 1 mm and 1 μm.

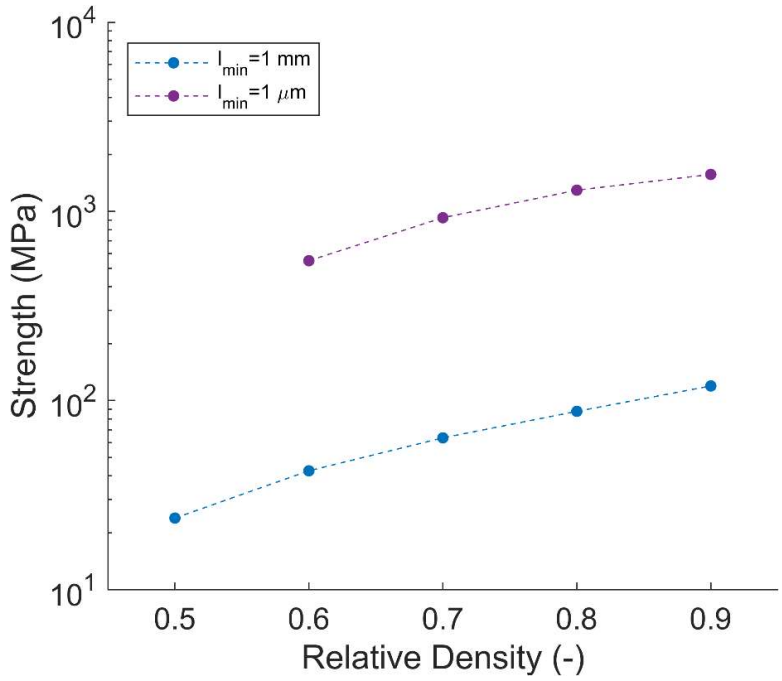

Figure 4.13. *Scaling behavior of monodisperse 3D foams with 50 pores with minimum ligament sizes of 1mm and 1 μm.*

To examine the mechanical response under larger deformations, compression simulations were performed of the lowest relative density ($\bar{\rho} = 0.5$) 2D foam for minimum ligament thicknesses of 1 mm, 100 μm, 10 μm, 1 μm and 100 nm. The stress-strain plots are displayed alongside the crack patterns with the underlying strength scales in Figure 4.14. All had characteristically brittle catastrophic failure, with one notable exception for the minimum ligament size 10 μm where a short plateau was observed after the initial stress drop due to the failure of a subset of ligaments. The crack patterns of both extremes of minimum ligament sizes are indicative of shear failure typical of foams, but intermediate minimum ligament sizes do not show such clear crack behavior. Comparison with 2D tensile strength results shows that the tensile and compressive strength asymmetry of the foams closely matches that of the alumina constituent material.

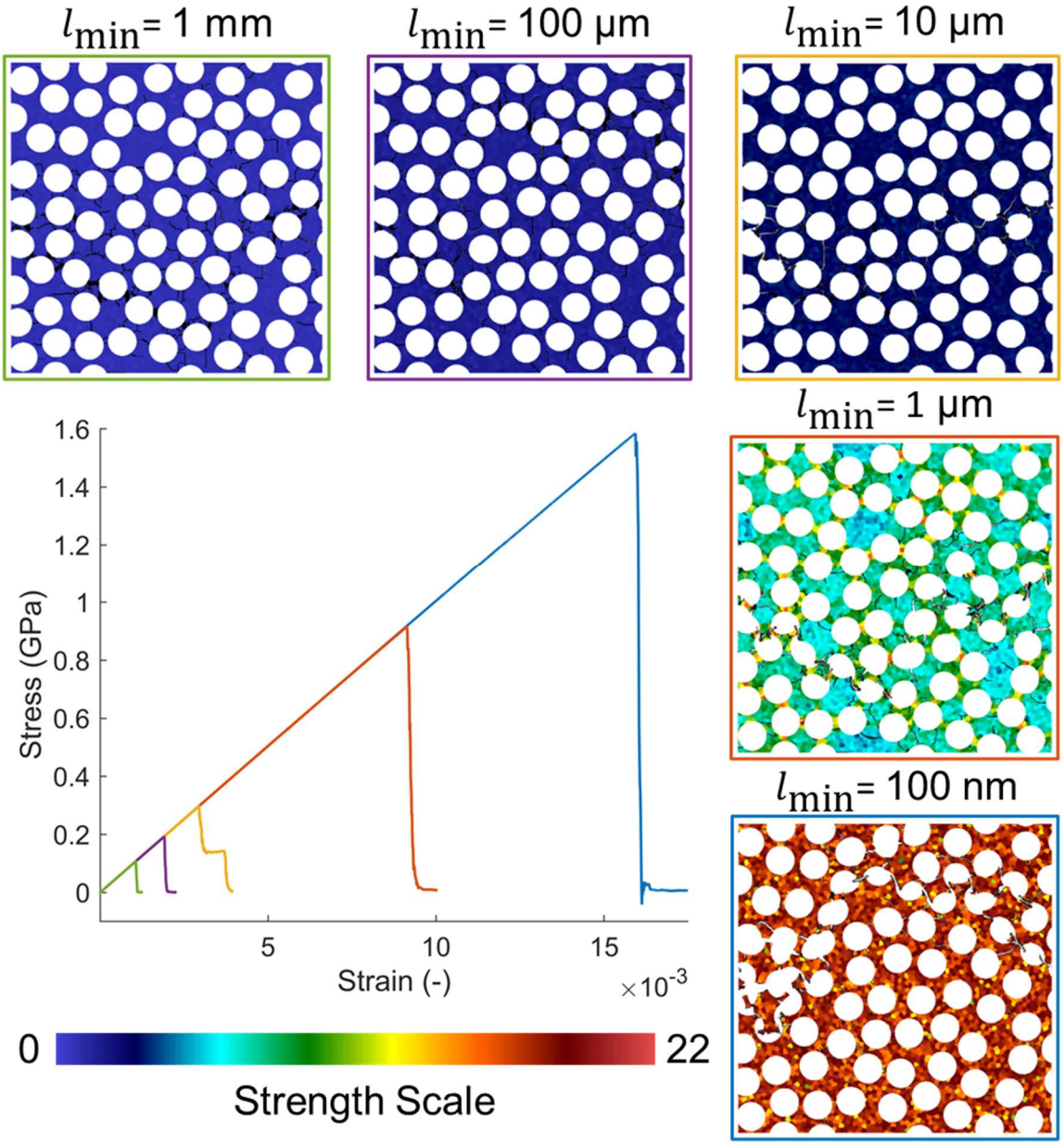

Figure 4.14. *Stress strain curves for monodisperse 2D foams of* $\bar{\rho} = 0.5$ *with different minimum ligament sizes subjected to uniaxial confined compression with renderings of particle strength scales and crack pattern after failure. Damaged material is shown in black.*

The elastic properties of the 2D and 3D monodisperse foams were also examined. The Young's modulus and Poisson's ratio were computed based on the transverse stresses in the simulation domains. The bulk and shear moduli were then computed from the Young's modulus and Poisson's ratio by isotropic

linear elastic relations. The elastic properties for 2D and 3D monodisperse foams are plotted in Figure 4.15 against the HS upper bound for an isotropic voided material. The elastic properties for monodisperse simulations are over and underestimated for simulations performed in 3D and 2D, respectively. However, the trends closely correspond to the expected scaling in relation to the Hashin-Shtrikman upper bound. The bulk moduli of both the 3D and 2D simulations matches the scaling of the upper bound almost exactly. The deviation in the Poisson's ratio from the HS upper bound is directly related to the deviation of the shear modulus from the bound at lower relative densities. Nonetheless, these monodisperse foams have elastic properties that surpass those of truss-based lattices which are only capable of reaching 50% of the upper bound.

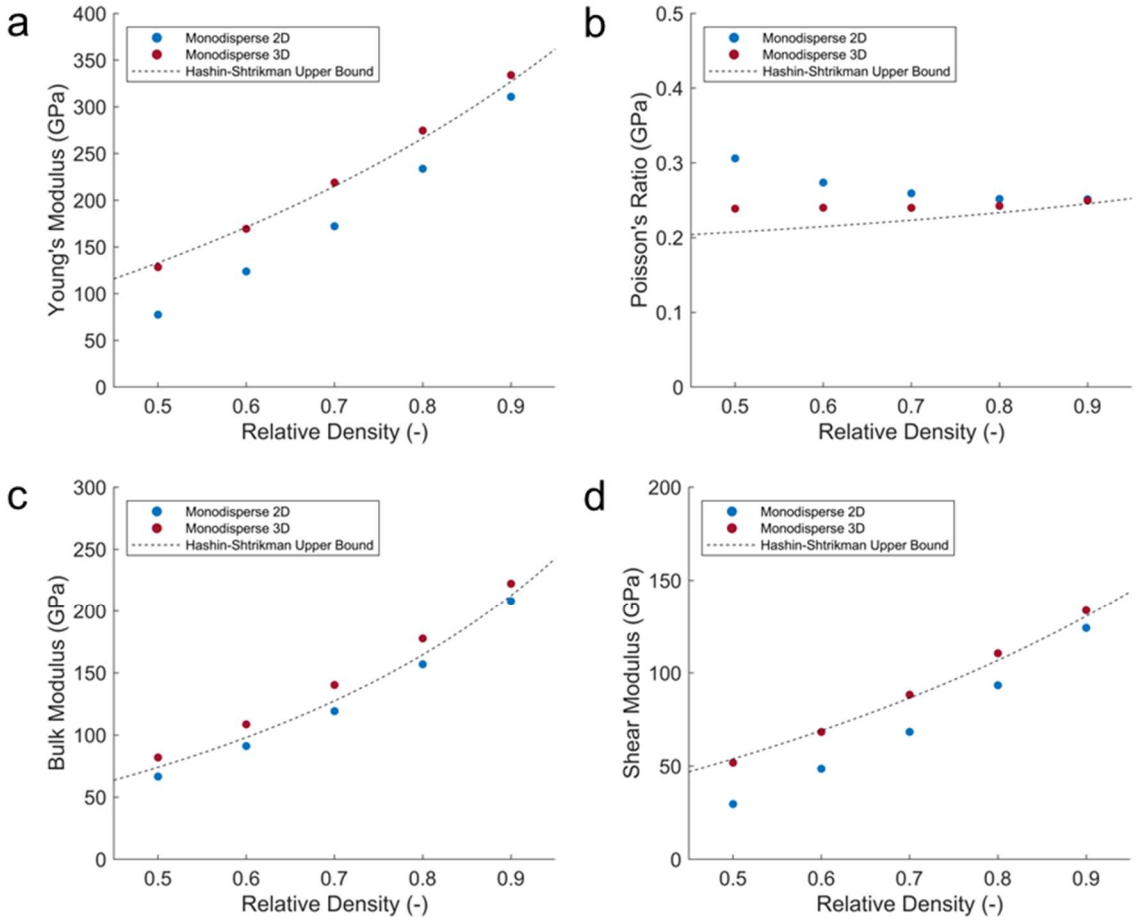

Figure 4.15. *Young's modulus (a), Poisson's ratio (b), bulk modulus (c) and shear modulus (d) of monodisperse 2D and 3D foams as determined under confined uniaxial tension plotted against the Hashin-Shtrikman upper bound for an isotropic voided material.*

A final investigation involved the role of bidispersity on the properties of syntactic foams. By introducing hollow particles of a different size, not only is the minimum attainable density reduced (lower relative density), but the smaller ligament sizes, provided the additional particles are smaller, could enhance strength. However, adding hierarchy is typically associated with compounding knockdowns of multiple scales of architectures. Because these simulations were too intensive to perform in 3D, 2D simulations were performed in tension of bidisperse foams with diameter ratios of large to small particles of 2, 3, and 5 at $\bar{\rho} = 0.5$. Although of interest, larger ratios were infeasible due to the number of small particles required for every large particle. Since clear convergence was not attainable in these more computationally intensive simulations, multiple simulations were performed with varying numbers of large pores per RVE to elucidate convergence trends. Additionally, the ratio of pore shells was varied either to maintain identical ligament thicknesses between small and large particles, denoted U, or thicknesses proportional to the pore diameter. Of those shells with thicknesses proportional to the particle diameter, two sets of simulations were run to control for the size-effect related to differences in ligament thickness by fixing the shell thickness of either the largest pores or the smallest pores, denoted by L and S, respectively, such that the ligament thicknesses of two identically sized contacting pores were 1 mm. Renderings of the strength scales for 2D bidisperse foams under these various conditions are shown in Figure 4.16. Both the L and S simulations were regarded as upper and lower bounds on the size-effect of bidisperse pores for a given fixed ligament size.

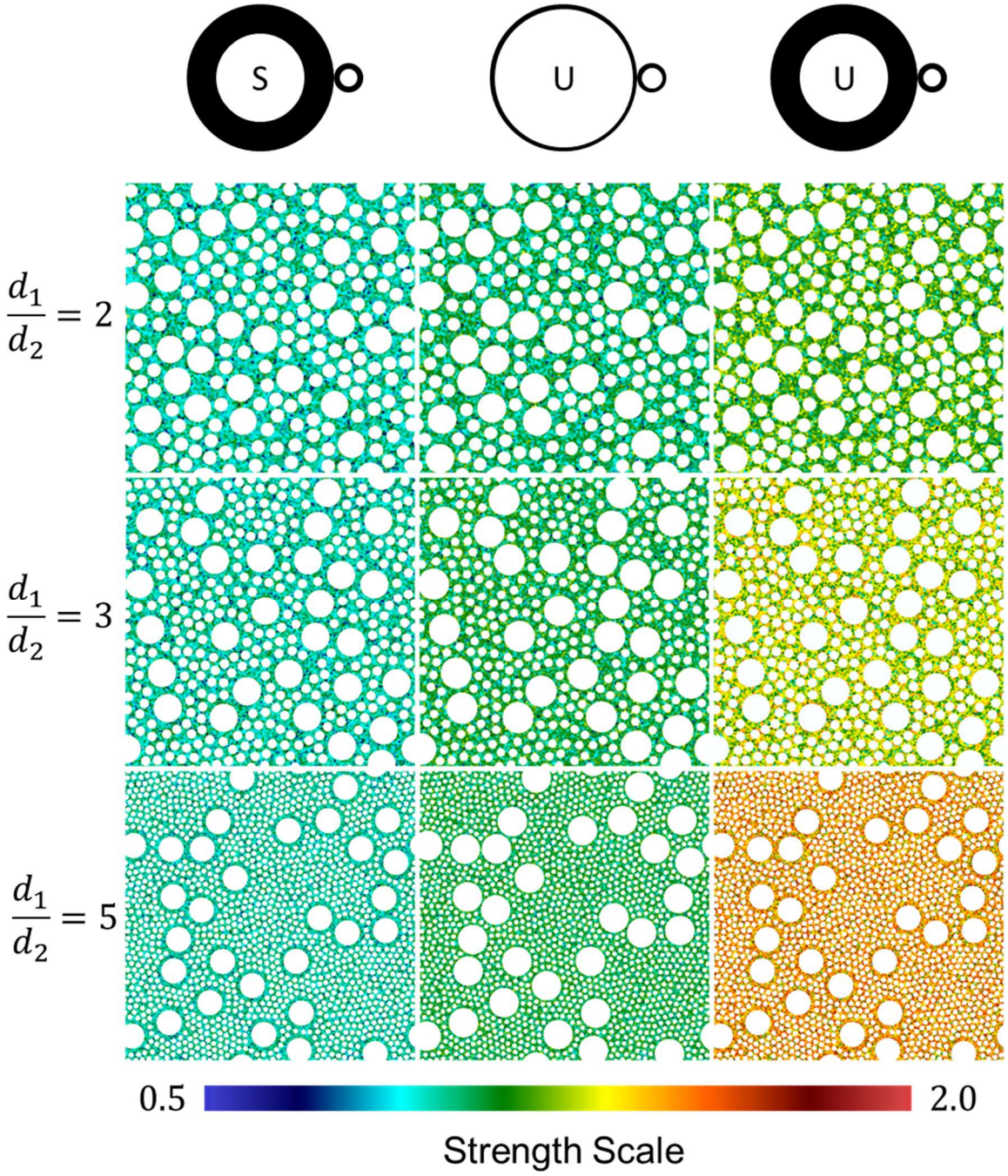

Figure 4.16. *Strength scale renderings of bidisperse 2D foams. Rows correspond to foams of different particle size disparities while columns from left to right correspond to fixed 1 mm ligament sizes between contacting large particles, uniform ligament sizes of 1 mm, and fixed 1 mm ligament sizes between contacting small particles.*

The strength results of tensile simulations are plotted in Figure 4.17. Interestingly, uniform ligaments and those where the smallest ligaments were controlled by the shells of the smallest particles had the lowest strengths, even below the monodisperse 2D foam. Furthermore, it appears that having uniform ligaments provides no advantage. However, simulations in which the smaller pores had correspondingly thinner ligaments enhanced by size-effect strengthening resulted in properties of the bidisperse foams surpassing those of the monodisperse foams.

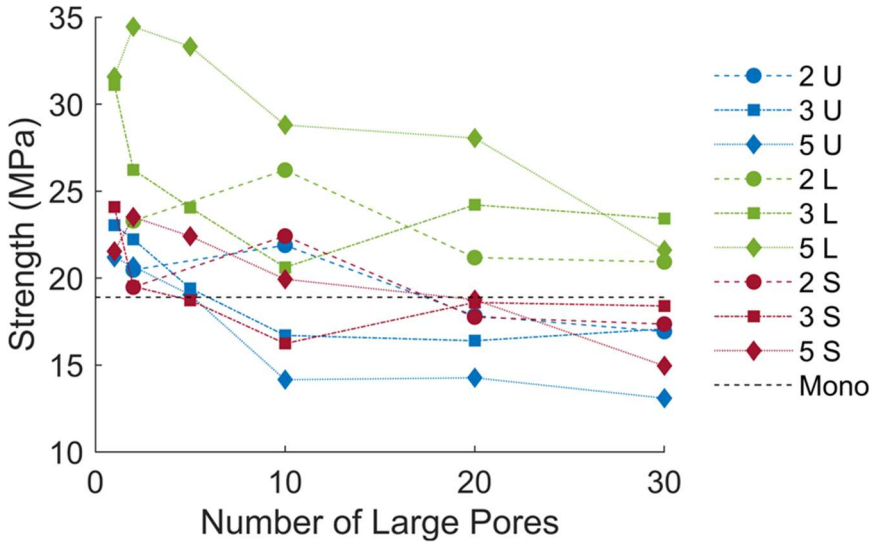

Figure 4.17. *Strength of bidisperse 2D foam simulations versus the number of large pores in the RVE. The suffixes L, U, and S denote fixed ligament sizes of 1 mm enforced between contacting larger particles, uniform ligaments, and contacting small particles, respectively. Mono refers to the strength of the 2D monodisperse foam with* $\bar{\rho} = 0.5$.

The deviation in strength between the 2D and 3D simulations is likely related to both the plane strain boundary conditions applied to 2D simulations and the greater directional freedom of 3D cracks. In both dimensionalities, the scaling in strength properties was worse than linear. However, the foams simulated here constitute high density architected materials while typical power law scaling relations are generally more applicable in the limit of low relative density.

After closer examination of the 2D monodisperse compression simulations, the origin of the failure response in the 10 μm minimum ligament size is unclear given that this behavior is not observed in the

other minimum ligament sizes despite identical pore geometry. This could indicate that the ligament strengthening is responsible, but it is not clear from the distribution in Figure 4.12a nor visually in the strength scale rendering. Nevertheless, the increase in peak stresses between the minimum ligament sizes closely matches the previous tensile experiments. Interestingly, no progressive failure was observed in the lowest relative density simulations performed here despite the stochastic structure and thin ligaments[69]. This could in part be due to the continuum treatment of cracks, e.g., there is no consideration of preferential crack propagation except as resolved by crack tip stresses. In most simulations, cracks originated at the surfaces of pores and propagated to the nearest pore. Since the highest stresses are typically developed within the thinnest section of the ligament most cracks quickly crossed the ligaments leading to catastrophic failure which correlates closely with the mechanism observed in pyrolytic carbon shell spinodals[69]. However, the failure of one crack in these structures led to the subsequent collapse of nearby ligaments which now had to support addition load causing a rapid cascade of failure.

Given that GEOS did not have boundary conditions for modelling periodic transverse boundaries with zero stress conditions, the overperformance of the 3D foams in relation to the HS upper bound is likely due to tests being performed in confined rather than unconfined uniaxial deformation. The material point method is also known to slightly overestimate elastic properties. However, closed-cell cellular materials are known to have bulk moduli which closely follow the HS upper bound[44] which is true of the trend for both the 2D and 3D simulations only with deviations in the form of offsets below and above the bound, respectively. In general, the elastic properties appear overestimated from 3D simulations. Therefore, the actual properties of foam likely reside somewhere in between the results of the 2D and 3D simulations. This closely matches previous computational work on random polydisperse spherical pores[144] where the stiffness was computed using finite element analysis. This might indicate that even monodisperse syntactic foams have elastic properties near the upper bound for stiffness for an isotropic voided material. Nevertheless, close-cell topologies are known to possess bulk moduli that reside near the HS upper bound, but lower shear moduli that have larger knockdowns causing deviations from the bound[44]. Regardless, the

elastic properties of these foams are expected to reside above those for truss-based lattices which are limited to 50% of the HS upper bound[40] and thus constitute a strong improvement over these topologies.

Regarding bidispersity, it is clear that having uniform ligaments derived from identical shell thicknesses of hollow large and small particles is detrimental to strength. Similarly, introducing larger pores results in strength knockdowns larger than those of the monodisperse foams. However, when smaller hollow particles with shell thicknesses proportional to their diameters are introduced, the size-effect related to smaller ligaments offsets knockdowns from the introduction of hierarchy, ultimately resulting in effective strengths surpassing those of monodisperse syntactic foams. Of course, this effect might be limited to bidisperse systems, in the sense that any improvement in constituent material strength derived by further levels of hierarchy may be negated by compounding knockdowns. The important implication is that there may be an optimal level of hierarchy related to this foam topology and the constituent material strength size-effect. Unfortunately, simulations of the scale required to investigate this are beyond current computational means.

4.10. Conclusion

In summary, monodisperse foams composed of nonoverlapping spherical pores, and an alumina constituent material were simulated under confined uniaxial tension and compression to examine the effect of ligament size, pore dispersity and relative density on mechanical properties. Reducing the minimum ligament size resulted in increasing strength, with the largest increase occurring due to ligaments with features below the critical flaw size taken from a macroscopic Weibull strength distribution. The failure response of all simulations followed catastrophic brittle failure while elastic properties for the monodisperse stochastic foams surpass periodic truss-based lattices. Lastly, although introducing hierarchy in the form of smaller pores is typically associated with strength knockdowns, it appears that the introduction of smaller size-effect strengthened ligaments might offset these losses.

5. Summary and Conclusions

This thesis investigated the potential of size-effect strengthened metamaterials, demonstrating unprecedented performance, and introducing novel techniques for scalable manufacturing and multi-scale modeling. Three specific contributions are reported: (i) a manufacturing process to fabricate nanoarchitected materials with complex plate topologies and a size-effect strengthened constituent material, resulting in optimal isotropic stiffness and unprecedented specific strength; (ii) a viable processing route to manufacture hollow microparticles for potential use as precursor porogens for size-effect strengthened syntactic foams; and (iii) a holistic multi-scale platform to model the mechanical behavior (strength and failure mechanisms) of syntactic foams based on the material point method, accounting for size-effects and stochastic response at the constituent material level, as well as large deformations and implicit contact.

In Chapter 2, plate-nanolattices were fabricated from pyrolytic carbon to experimentally verify their superior performance at the upper bounds of stiffness and strength and demonstrate dramatic improvements over well-established truss-based lattices. This marked the first demonstration of plate lattices reaching the Hashin-Shtrikman and Suquet upper bounds for isotropic stiffness and strength, respectively. Moreover, the combination of an optimal plate-lattice topology with size-effect strengthened pyrolytic carbon as constituent material resulted in the architected material with the highest specific strength ever reported (at the time of publishing).

In Chapter 3, a process to fabricate hollow template-free ceramic particles was introduced as a means to enable future self-assembled size-effect strengthened syntactic ceramic foams wherein the hollow ceramic particles become the porogen allowing exceptional control over pore size distribution. In addition to demonstrating tunability of the particle size and wall thickness, the process also included special considerations for scalability and extensibility to other material systems to enable fabrication of application relevant quantities of monodisperse hollow ceramic particles, for potential uses which extend well beyond the fabrication of efficient mechanical metamaterials.

In Chapter 4, a multi-scale computational procedure is developed to model mechanical response (initial strength and progressive failure mechanisms) in size-effect strengthened ceramic syntactic foams, which may be produced in a scalable fashion using the particle porogens introduced in the previous chapter. The computational approach includes a novel flaw field which may be generated for arbitrary porosity, and an accompanying material model which accounts for Weibull variability in the strength of brittle ceramics as well as increasing strength arising from reductions in the characteristic dimension of geometric features. This model is developed in the framework of the material point method, constituting the first demonstration of a simulation incorporating large deformation, contact and fracture mechanics to investigate the strength and failure mechanisms of syntactic foams under uniaxial tension and compression.

This thesis lays the groundwork for the design, modeling, and scalable manufacturing of future mechanical metamaterials with enhanced properties, for a wide range of applications.

6. References

[1] W. Cai, U. K. Chettiar, A. V. Kildishev, V. M. Shalaev, *Nat. Photonics* **2007**, *1*, 224.

[2] A. I. Hochbaum, R. Chen, R. D. Delgado, W. Liang, E. C. Garnett, M. Najarian, A. Majumdar, P. Yang, *Nature* **2008**, *451*, 163.

[3] M. Konaković, K. Crane, B. Deng, S. Bouaziz, D. Piker, M. Pauly, *ACM Trans. Graph.* **2016**, *35*, 1.

[4] Q. Wang, J. A. Jackson, Q. Ge, J. B. Hopkins, C. M. Spadaccini, N. X. Fang, *Phys. Rev. Lett.* **2016**, *117*, 175901.

[5] S. Shan, S. H. Kang, J. R. Raney, P. Wang, L. Fang, F. Candido, J. A. Lewis, K. Bertoldi, *Adv. Mater.* **2015**, *27*, 4296.

[6] J. Bauer, A. Schroer, R. Schwaiger, O. Kraft, *Nat. Mater.* **2016**, *15*, 438.

[7] E. Orowan, *Rep. Prog. Phys.* **1949**, *12*, 185.

[8] J. Frenkel, *Z. Für Phys.* **1926**, *37*, 572.

[9] M. A. Meyers, K. K. Chawla, *Mechanical Behavior of Materials*, Cambridge University Press, **2008**.

[10] M. D. Uchic, P. A. Shade, D. M. Dimiduk, *Annu. Rev. Mater. Res.* **2009**, *39*, 361.

[11] Alan Arnold Griffith, *Philos. Trans. R. Soc. Lond. Ser. A* **1921**, *221*, 163.

[12] J. Bauer, C. Crook, A. G. Izard, Z. C. Eckel, N. Ruvalcaba, T. A. Schaedler, L. Valdevit, *Matter* **2019**, *1*, 1547.

[13] J. Bauer, L. R. Meza, T. A. Schaedler, R. Schwaiger, X. Zheng, L. Valdevit, *Adv. Mater.* **2017**, *29*, 1701850.

[14] X. Zhang, A. Vyatskikh, H. Gao, J. R. Greer, X. Li, *Proc. Natl. Acad. Sci.* **2019**, *116*, 6665.

[15] X. Zheng, W. Smith, J. Jackson, B. Moran, H. Cui, D. Chen, J. Ye, N. Fang, N. Rodriguez, T. Weisgraber, C. M. Spadaccini, *Nat. Mater.* **2016**, *15*, 1100.

[16] X. Zheng, H. Lee, T. H. Weisgraber, M. Shusteff, J. DeOtte, E. B. Duoss, J. D. Kuntz, M. M. Biener, Q. Ge, J. A. Jackson, S. O. Kucheyev, N. X. Fang, C. M. Spadaccini, *Science* **2014**, *344*, 1373.

[17] S. N. Khaderi, M. R. J. Scherer, C. E. Hall, U. Steiner, U. Ramamurty, N. A. Fleck, V. S. Deshpande, *Extreme Mech. Lett.* **2017**, *10*, 15.

[18] J. J. do Rosário, J. B. Berger, E. T. Lilleodden, R. M. McMeeking, G. A. Schneider, *Extreme Mech. Lett.* **2017**, *12*, 86.

[19] J. H. Pikul, S. Özerinç, B. Liu, R. Zhang, P. V. Braun, V. S. Deshpande, W. P. King, *Sci. Rep.* **2019**, *9*, 719.

[20] J. Biener, A. M. Hodge, A. V. Hamza, L. M. Hsiung, J. H. Satcher, *J. Appl. Phys.* **2005**, *97*, 024301.

[21] C. A. Volkert, E. T. Lilleodden, D. Kramer, J. Weissmüller, *Appl. Phys. Lett.* **2006**, *89*, 061920.

[22] A. M. Hodge, J. Biener, J. R. Hayes, P. M. Bythrow, C. A. Volkert, A. V. Hamza, *Acta Mater.* **2007**, *55*, 1343.

[23] L. J. Gibson, M. F. Ashby, *Cellular Solids: Structure and Properties*, Cambridge University Press, **1999**.

[24] L. J. Gibson, M. F. Ashby, *Adv. Polym. Technol.* **1989**, *9*, 165.

[25] V. S. Deshpande, N. A. Fleck, M. F. Ashby, *J Mech Phys Solids* **2001**, *49*, 1747.

[26] T. Tancogne-Dejean, D. Mohr, *Int. J. Solids Struct.* **2018**, *138*, 24.

[27] Z. Hashin, S. Shtrikman, *J. Mech. Phys. Solids* **1963**, *11*, 127.

[28] J. Bauer, A. Schroer, R. Schwaiger, I. Tesari, C. Lange, L. Valdevit, O. Kraft, *Extreme Mech. Lett.* **2015**, *3*, 105.

[29] A. Lai, Z. Du, C. L. Gan, C. A. Schuh, *Science* **2013**, *341*, 1505.

[30] G. Castro, S. R. Nutt, *Mater. Sci. Eng. A* **2012**, *553*, 89.

[31] B. P. Neville, A. Rabiei, *Mater. Des.* **2008**, *29*, 388.

[32] A. Rabiei, A. T. O'Neill, *Mater. Sci. Eng. A* **2005**, *404*, 159.

[33] J. Marx, A. Rabiei, *Adv. Eng. Mater.* **2017**, *19*, 1600776.

[34] P. M. Suquet, *J. Mech. Phys. Solids* **1993**, *41*, 981.

[35] X. Zhang, Y. Wang, B. Ding, X. Li, *Small* **2020**, *16*, 1902842.

[36] J. R. Greer, V. S. Deshpande, *MRS Bull.* **2019**, *44*, 750.

[37] J. J. do Rosário, E. T. Lilleodden, M. Waleczek, R. Kubrin, A. Yu. Petrov, P. N. Dyachenko, J. E. C. Sabisch, K. Nielsch, N. Huber, M. Eich, G. A. Schneider, *Adv. Eng. Mater.* **2015**, *17*, 1420.

[38] V. S. Deshpande, M. F. Ashby, N. A. Fleck, *Acta Mater.* **2001**, *49*, 1035.

[39] M. C. Messner, *J. Mech. Phys. Solids* **2016**, *96*, 162.

[40] L. Dong, V. Deshpande, H. Wadley, *Int. J. Solids Struct.* **2015**, *60*, 107.

[41] D. Pasini, J. K. Guest, *MRS Bull.* **2019**, *44*, 766.

[42] T. Tancogne-Dejean, M. Diamantopoulou, M. B. Gorji, C. Bonatti, D. Mohr, *Adv. Mater.* **2018**, 1803334.

[43] H. N. G. Wadley, *Philos. Trans. R. Soc. Math. Phys. Eng. Sci.* **2006**, *364*, 31.

[44] J. B. Berger, H. N. G. Wadley, R. M. McMeeking, *Nature* **2017**, *543*, 533.

[45] R. Schwaiger, L. R. Meza, X. Li, *MRS Bull.* **2019**, *44*, 758.

[46] X. Li, H. Gao, *Nat. Mater.* **2016**, *15*, 373.

[47] Granta Design Limited, **2019**.

[48] L. J. Jiang, Y. S. Zhou, W. Xiong, Y. Gao, X. Huang, L. Jiang, T. Baldacchini, J.-F. Silvain, Y. F. Lu, *Opt. Lett.* **2014**, *39*, 3034.

[49] A. Sadezky, H. Muckenhuber, H. Grothe, R. Niessner, U. Pöschl, *Carbon* **2005**, *43*, 1731.

[50] M. Zilske, H. Lamecker, S. Zachow, *Proc EUROGRAPHICS 2008* **2007**, *27*.

[51] M. P. Manoharan, H. Lee, R. Rajagopalan, H. C. Foley, M. a. Haque, *Nanoscale Res. Lett.* **2010**, *5*, 14.

[52] C. Garion, *World J. Mech.* **2014**, *4*, 79.

[53] M. Danielsson, D. M. Parks, M. C. Boyce, *J. Mech. Phys. Solids* **2002**, *50*, 351.

[54] C. N. LaFratta, J. T. Fourkas, T. Baldacchini, R. A. Farrer, *Angew. Chem. Int. Ed.* **2007**, *46*, 6238.

[55] A. Albiez, R. Schwaiger, *MRS Adv.* **2019**, 1.

[56] X. Zhang, L. Zhong, A. Mateos, A. Kudo, A. Vyatskikh, H. Gao, J. R. Greer, X. Li, *Nat. Nanotechnol.* **2019**, 1.

[57] T. A. Schaedler, A. J. Jacobsen, A. Torrents, A. E. Sorensen, J. Lian, J. R. Greer, L. Valdevit, W. B. Carter, *Science* **2011**, *334*, 962.

[58] J. R. Hayes, A. M. Hodge, J. Biener, A. V Hamza, K. Sieradzki, *J. Mater. Res.* **2006**, *21*, 2611.

[59] Z. C. Eckel, C. Zhou, J. H. Martin, A. J. Jacobsen, W. B. Carter, T. A. Schaedler, *Science* **2016**, *351*, 58.

[60] A. Torrents, T. A. Schaedler, A. J. Jacobsen, W. B. Carter, L. Valdevit, *Acta Mater.* **2012**, *60*, 3511.

[61] J. Bauer, S. Hengsbach, I. Tesari, R. Schwaiger, O. Kraft, *Proc Natl Acad Sci USA* **2014**, *111*, 2453.

[62] M. Mieszala, M. Hasegawa, G. Guillonneau, J. Bauer, R. Raghavan, C. Frantz, O. Kraft, S. Mischler, J. Michler, L. Philippe, *Small* **2017**, *13*, 1602514.

[63] X. W. Gu, J. R. Greer, *Extreme Mech. Lett.* **2015**, *2*, 7.

[64] L. Valdevit, S. W. Godfrey, T. a. Schaedler, A. J. Jacobsen, W. B. Carter, *J. Mater. Res.* **2013**, *28*, 2461.

[65] J. Bauer, A. Schroer, R. Schwaiger, O. Kraft, *Adv. Eng. Mater.* **2016**, *18*, 1537.

[66] L. R. Meza, S. Das, J. R. Greer, *Science* **2014**, *345*, 1322.

[67] A. J. Jacobsen, S. Mahoney, W. B. Carter, S. Nutt, *Carbon* **2011**, *49*, 1025.

[68] I. C. Cheng, A. M. Hodge, *Scr. Mater.* **2013**, *69*, 295.

[69] A. G. Izard, J. Bauer, C. Crook, V. Turlo, L. Valdevit, *Small* **2019**, *15*, 1903834.

[70] J. Bauer, A. G. Izard, Y. Zhang, T. Baldacchini, L. Valdevit, *Adv. Mater. Technol.* **2019**, 1900146.

[71] Y. Ji, C. Li, G. Wang, J. Koo, S. Ge, B. Li, J. Jiang, B. Herzberg, T. Klein, S. Chen, J. C. Sokolov, M. H. Rafailovich, *EPL* **2008**, *84*.

[72] J. X. Zhao, R. C. Bradt, P. L. J. Walker, *Carbon* **1985**, *23*, 15.

[73] C. Sun, N. Fang, D. M. Wu, X. Zhang, *Sens. Actuators Phys.* **2005**, *121*, 113.

[74] L. Jonušauskas, D. Gailevičius, S. Rekštytė, T. Baldacchini, S. Juodkazis, M. Malinauskas, *Opt. Express* **2019**, *27*, 15205.

[75] B. T. T. Pham, D. Nguyen, V. T. Huynh, E. H. Pan, B. Shirodkar-Robinson, M. Carey, A. K. Serelis, G. G. Warr, T. Davey, C. H. Such, B. S. Hawkett, *Langmuir* **2018**, *34*, 4255.

[76] S.-H. Kim, S. Magkiriadou, D. K. Rhee, D.-S. Lee, P. J. Yoo, V. N. Manoharan, G.-R. Yi, *ACS Appl. Mater. Interfaces* **2017**, *9*, 24155.

[77] B. S. Garrett, N. J. Hudak, M. Zablocki, T. Creazzo, A. Sharkawy, B. G. DeLacy, M. S. Mirotznik, *J. Opt. Soc. Am. A* **2020**, *37*, 1989.

[78] G. M. Koenig, I. Belharouak, H. M. Wu, K. Amine, *Electrochimica Acta* **2011**, *56*, 1426.

[79] C.-M. Kang, Y. Baek, J.-Y. Jeong, J. Sim, E.-J. Gwak, T.-J. Je, D.-S. Choi, G. M. Kim, J. S. Han, *Ceram. Int.* **2022**, *48*, 32036.

[80] L. Zhang, J. Ma, *Carbon* **2009**, *47*, 1451.

[81] N. Gupta, R. Nagorny, *J. Appl. Polym. Sci.* **2006**, *102*, 1254.

[82] A. Vyatskikh, R. C. Ng, B. Edwards, R. M. Briggs, J. R. Greer, *Nano Lett.* **2020**, *20*, 3513.

[83] D. W. Yee, M. L. Lifson, B. W. Edwards, J. R. Greer, *Adv. Mater.* **2019**, *31*, 1901345.

[84] J. Bertling, J. Blömer, R. Kümmel, *Chem. Eng. Technol.* **2004**, *27*, 829.

[85] M. Chatterjee, D. Enkhtuvshin, B. Siladitya, D. Ganguli, *J. Mater. Sci.* **1998**, *33*, 4937.

[86] D. Li, Z. Guan, W. Zhang, X. Zhou, W. Y. Zhang, Z. Zhuang, X. Wang, C. J. Yang, *ACS Appl. Mater. Interfaces* **2010**, *2*, 2711.

[87] T. Nakashima, N. Kimizuka, *J. Am. Chem. Soc.* **2003**, *125*, 6386.

[88] Z. Károly, J. Szépvölgyi, *Powder Technol.* **2003**, *132*, 211.

[89] T. Kato, H. Ushijima, M. Katsumata, T. Hyodo, Y. Shimizu, M. Egashira, *J. Mater. Sci.* **2002**, *37*, 2317.

[90] Y. D. Xia, R. Mokaya, *Adv. Mater.* **2004**, *16*, 886.

[91] F.-L. Li, H.-J. Zhang, *Materials* **2017**, *10*, 995.

[92] K. Y. Jang, K. Kim, R. S. Upadhye, *J. Vac. Sci. Technol. Vac. Surf. Films* **1990**, *8*, 1732.

[93] X.-F. Guo, Y.-S. Kim, G.-J. Kim, *J. Phys. Chem. C* **2009**, *113*, 8313.

[94] Q. Zhang, W. Wang, J. Goebl, Y. Yin, *Nano Today* **2009**, *4*, 494.

[95] Y. Xia, R. Mokaya, *J. Mater. Chem.* **2005**, *15*, 3126.

[96] R. Nakamura, D. Tokozakura, H. Nakajima, J.-G. Lee, H. Mori, *J. Appl. Phys.* **2007**, *101*, 074303.

[97] P. Roy, G. Bertrand, C. Coddet, *Powder Technol.* **2005**, *157*, 20.

[98] K. H. Moh, M. Company, S. Paul, *MRS Online Proc. Libr.* **1994**, *372*, 15.

[99] L. Li, X. Liu, G. Wang, Y. Liu, W. Kang, N. Deng, X. Zhuang, X. Zhou, *Chem. Eng. J.* **2021**, *421*, 127744.

[100] M. A. Aegerter, N. Leventis, M. M. Koebel, Eds., *Aerogels Handbook*, Springer New York, New York, NY, **2011**.

[101] B. E. Yoldas, *J. Appl. Chem. Biotechnol.* **1973**, *23*, 803.

[102] I. J. Worrall, *J. Chem. Educ.* **1969**, *46*, 510.

[103] B. E. Yoldas, *J. Mater. Sci.* **1975**, *10*, 1856.

[104] T. F. Baumann, A. E. Gash, S. C. Chinn, A. M. Sawvel, R. S. Maxwell, J. H. Satcher, *Chem. Mater.* **2005**, *17*, 395.

[105] A. E. Gash, T. M. Tillotson, J. H. Satcher Jr, L. W. Hrubesh, R. L. Simpson, *J. Non-Cryst. Solids* **2001**, *285*, 22.

[106] C. Jing, X. Zhao, Y. Zhang, *Mater. Res. Bull.* **2007**, *42*, 600.

[107] T. Heinrich, F. Raether, H. Marsmann, *J. Non-Cryst. Solids* **1994**, *168*, 14.

[108] M.-A. Muñoz-Hernandez, T. S. Keizer, S. Parkin, Y. Zhang, D. A. Atwood, *J. Chem. Crystallogr.* **2000**, *30*, 219.

[109] J. Wang, Y. Wang, M. Qiao, S. Xie, K. Fan, *Mater. Lett.* **2007**, *61*, 5074.

[110] R. K. Shah, H. C. Shum, A. C. Rowat, D. Lee, J. J. Agresti, A. S. Utada, L.-Y. Chu, J.-W. Kim, A. Fernandez-Nieves, C. J. Martinez, D. A. Weitz, *Mater. Today* **2008**, *11*, 18.

[111] E. Amstad, M. Chemama, M. Eggersdorfer, L. R. Arriaga, M. P. Brenner, D. A. Weitz, *Lab. Chip* **2016**, *16*, 4163.

[112] W.-C. Jeong, J.-M. Lim, J.-H. Choi, J.-H. Kim, Y.-J. Lee, S.-H. Kim, G. Lee, J.-D. Kim, G.-R. Yi, S.-M. Yang, *Lab. Chip* **2012**, *12*, 1446.

[113] C. Charcosset, I. Limayem, H. Fessi, *J. Chem. Technol. Biotechnol.* **2004**, *79*, 209.

[114] H. Brandenberger, D. Nüssli, V. Piëch, F. Widmer, *J. Electrost.* **1999**, *45*, 227.

[115] Y.-F. Maa, C. C. Hsu, *Pharm. Dev. Technol.* **1999**, *4*, 233.

[116] S. G. Bardenhagen, E. M. Kober, *Comput. Model. Eng. Sci.* **2004**, *5*, 477.

[117] A. Sadeghirad, R. M. Brannon, J. Burghardt, *Int. J. Numer. Methods Eng.* **2011**, *86*, 1435.

[118] G. K. Bansal, W. H. Duckworth, D. E. Niesz, *J. Am. Ceram. Soc.* **1976**, *59*, 472.

[119] J. J. Petrovic, *Metall. Trans. A* **1987**, *18*, 1829.

[120] S. Nohut, *Ceram. Int.* **2012**, *38*, 2411.

[121] R. Danzer, T. Lube, P. Supancic, R. Damani, *Adv. Eng. Mater.* **2008**, *10*, 275.

[122] M. Albakry, M. Guazzato, M. Vincent Swain, *J. Dent.* **2004**, *32*, 91.

[123] D. K. Tran, A. S. Kobayashi, K. W. White, *Exp. Mech.* **1999**, *39*, 20.

[124] J. P. Gross, J. Malzbender, R. Schwaiger, *J. Mater. Sci.* **2022**, *57*, 7481.

[125] Y. Fu, Z. Tao, X. Hou, *Ceram. Int.* **2014**, *40*, 7661.

[126] V. Rontu, A. Nolvi, A. Hokkanen, E. Haeggström, I. Kassamakov, S. Franssila, *Mater. Res. Express* **2018**, *5*, 046411.

[127] E. Feilden, T. Giovannini, N. Ni, C. Ferraro, E. Saiz, L. Vandeperre, F. Giuliani, *Scr. Mater.* **2017**, *131*, 55.

[128] M. Berdova, T. Ylitalo, I. Kassamakov, J. Heino, P. T. Törmä, L. Kilpi, H. Ronkainen, J. Koskinen, E. Hæggström, S. Franssila, *Acta Mater.* **2014**, *66*, 370.

[129] N. R. Philips, B. G. Compton, M. R. Begley, *J. Am. Ceram. Soc.* **2012**, *95*, 3016.

[130] M. Michálek, M. Michálková, G. Blugan, J. Kuebler, *Ceram. Int.* **2018**, *44*, 3255.

[131] A. E. Lupercio, E. Moshkelgosha, R. C. Winters, C. Doyle, M. Mamivand, A. T. Nelson, B. J. Jaques, *Int. J. Ceram. Eng. Sci.* **2021**, *3*, 128.

[132] G. Žagar, V. Pejchal, M. G. Mueller, A. Rossoll, M. Cantoni, A. Mortensen, *Acta Mater.* **2015**, *100*, 215.

[133] Y. Han, S. Li, T. Zhu, W. Wu, D. An, Z. Xie, *Ceram. Int.* **2018**, *44*, 5238.

[134] A. Krell, *J. Am. Ceram. Soc.* **1998**, *81*, 1900.

[135] P. E. Cantonwine, *J. Mater. Sci.* **2003**, *38*, 461.

[136] S. Wang, Y. He, H. Huang, J. Zou, G. J. Auchterlonie, L. Hou, B. Huang, *Nanotechnology* **2013**, *24*, 285703.

[137] J. Lankford, *J. Mater. Sci.* **1977**, *12*, 791.

[138] S. Kuroyanagi, K. Shinoda, A. Yumoto, J. Akedo, *Acta Mater.* **2020**, *195*, 588.

[139] L. J. Broutman, R. H. Cornish, *J. Am. Ceram. Soc.* **1965**, *48*, 519.

[140] R. Danzer, W. Harrer, P. Supancic, T. Lube, Z. Wang, A. Börger, *J. Eur. Ceram. Soc.* **2007**, *27*, 1481.

[141] S. M. Jeong, S. E. Park, H. L. Lee, *J. Eur. Ceram. Soc.* **2002**, *22*, 1129.

[142] L. J. H. Seelen, J. T. Padding, J. A. M. Kuipers, *Chem. Eng. Sci.* **2018**, *189*, 84.

[143] S. R. Williams, I. K. Snook, W. van Megen, *Phys. Rev. E* **2001**, *64*, 021506.

[144] M. G. Tarantino, O. Zerhouni, K. Danas, *Acta Mater.* **2019**, *175*, 331.

[145] B. D. Lubachevsky, F. H. Stillinger, *J. Stat. Phys.* **1990**, *60*, 561.

[146] V. Baranau, U. Tallarek, *Soft Matter* **2014**, *10*, 3826.

[147] M. Skoge, A. Donev, F. H. Stillinger, S. Torquato, *Phys. Rev. E* **2006**, *74*, 041127.

[148] M. A. Homel, S. A. Povolny, C. Crook, E. B. Herbold, **2023**.

[149] H. W. Meyer, R. M. Brannon, *Int. J. Impact Eng.* **2012**, *42*, 48.

[150] O. E. Strack, R. B. Leavy, R. M. Brannon, *Int. J. Numer. Methods Eng.* **2015**, *102*, 468.

[151] Alan T. Zehnder, Q. Jane Wang, Yip-Wah Chung, in *Encycl. Tribol.*, Springer US, Boston, MA, **2013**, pp. 2292–2295.

[152] J. Laurencin, G. Delette, M. Dupeux, *J. Eur. Ceram. Soc.* **2008**, *28*, 1.

[153] M. A. Homel, E. B. Herbold, *Int. J. Numer. Methods Eng.* **2017**, *109*, 1013.

[154] R. Brannon, S. Leelavanichkul, *Survey of Four Damage Models for Concrete.*, Sandia National Laboratories, Albuquerque, New Mexico 87185 and Livermore, California 94550, **2009**.

[155] M. A. Homel, R. M. Brannon, J. Guilkey, *Int. J. Numer. Methods Eng.* **2016**, *107*, 31.

[156] T. Bückmann, N. Stenger, M. Kadic, J. Kaschke, A. Frölich, T. Kennerknecht, C. Eberl, M. Thiel, M. Wegener, *Adv. Mater.* **2012**, *24*, 2710.

[157] ASTM International, *Standard Test Method for Compressive Properties of Rigid Plastics*, **2008**.

Appendix A. Pyrolytic Carbon Cubic+Octet Plate-Nanolattice Manufacturing Strategy

Cubic+octet plate-nanolattices were fabricated by a two-photon-polymerization direct laser writing (TPP-DLW) and pyrolysis[6] fabrication route (Figure A.1). Samples were printed atop a silicon wafer with a drop of IP-Dip resin into which the writing objective was inserted from below, also termed Dip-in Laser Lithography (DiLL)[156]. After printing, samples were developed in a PGMEA bath followed by an IPA bath and then dried in a critical point dryer (CPD). Once developed, samples were pyrolyzed to convert the polymer to pyrolytic carbon.

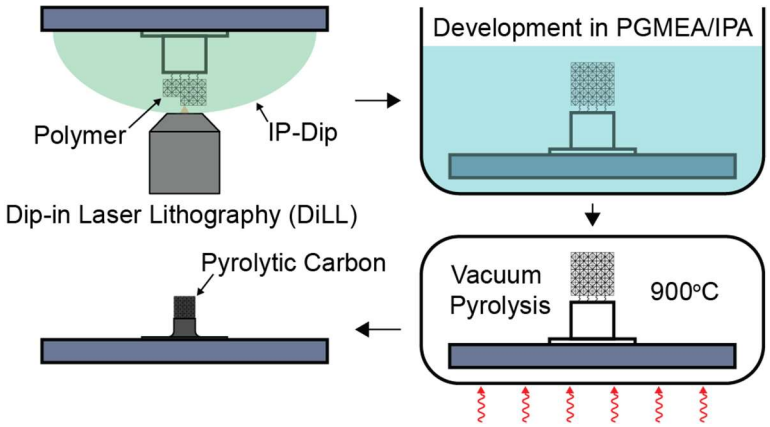

Figure A.1. *Illustration of two-photon-polymerization-direct laser writing (TPP-DLW) and pyrolysis process for manufacturing of pyrolytic ceramic nanolattices.*

TPP-DLW and pyrolysis has been successfully employed for open-cell nano-architectures, like beam-lattices[6,13,14], whereby entire structures can be printed in a simple 3D trajectory pattern with a fixed set of process parameters. In contrast, the complexity of plate-nanolattices imposes several manufacturing challenges, including precise wall thickness and constituent material property control, retention of high surface quality while printing at the TPP-DLW resolution limit in a layer-by-layer pattern, and

accommodation of pyrolysis-induced shrinkage with ~3 times larger structures compared to same-feature-size beam-lattices of a given relative density. To resolve the above challenges, we have developed a plate orientation specific TPP-DLW strategy, encompassing a writing parameter optimization procedure using SEM-based wall thickness and surface quality calibration, micro-Raman spectroscopy-measured microstructural characterization and optimization of support pillars and springs.

Figure A.2 illustrates the hatching strategies adopted to print horizontal and vertical cubic walls of the same thickness with the correct thickness ratio to the octet walls, while achieving the smallest possible feature size and hence structure sizes. This ensures manufacturability within the limited print volume and minimal pyrolysis-induced shrinkage deformations in addition to the best possible exploitation of material-strengthening size-effects. The wall-specific hatching strategy, necessitated by the ellipsoidal voxel shape inherent to TPP-DLW, required thickness control of single voxel-thick horizontal cubic and octet walls by laser average power, while the vertical cubic wall thickness was controlled by the hatching distance and number of hatched lines.

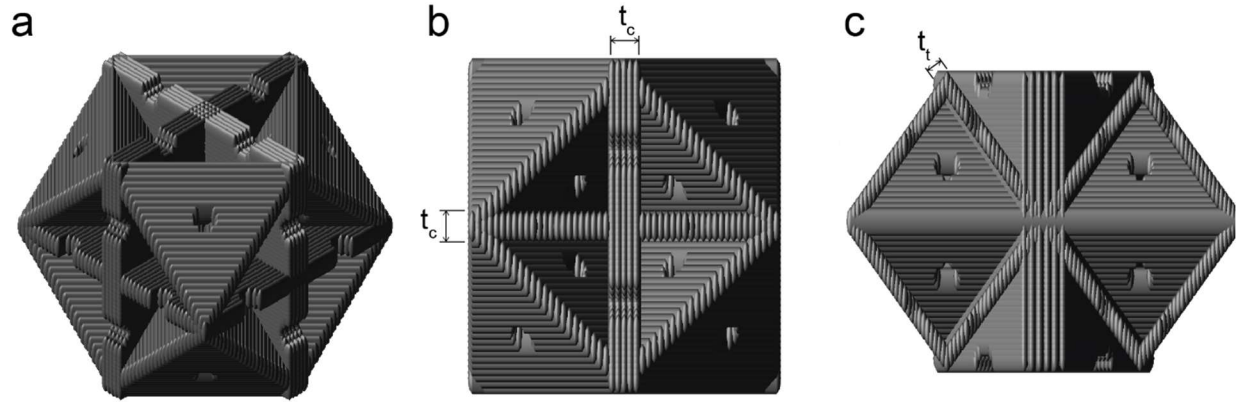

Figure A.2. *Wall orientation specific hatching strategies print cubic+octet plate-lattices with maximal surface quality and smallest possible feature sizes. Renderings of cubic+octet plate-lattice TPP-DLW print strategies of a unit cell (a-c) showing that octet and horizontal cubic walls are composed of single voxel-thick lines and vertical cubic walls are composed of many closely hatched lines. Wall thicknesses are denoted as* t_t *and* t_c *for octet and cubic walls, respectively. Note that slicing, hatching distances, and number of vertical hatched lines are coarsened to easily view the print strategy.*

The degree of conversion and hence the mechanical properties of TPP-DLW-derived polymer and pyrolytic carbon largely vary depending on the TPP-DLW writing parameters[70], such as writing speed (v), laser average power (P) as well as hatching (hd) and slicing distance (sd). For the best compromise between structure quality and print time, a v of 5,000 µm/s and sd of 0.05 µm were chosen. Before selecting specific P and hd based on the desired wall thicknesses, the degree of conversion (DC) of individual polymer unit cell plate orientations following a post-print bake were measured by micro-Raman spectroscopy for a range of writing parameters within the printable range. The results of these measurements (Figure A.3a) revealed that the DC largely clustered around 60%. Wall thickness data of fixed hatching distances for the cubic walls (Figure A.3b) was then measured from polymer calibration structures (Figure A.3c) also used to assess the relative surface quality and dimensional reproducibility.

Writing parameters, laser average power, hatching distance and number of hatched lines were then selected within the parametric sweep range of the Raman and wall thickness calibration data in order to provide the best surface quality, smallest feature dimensions, approximately identical DC and correct wall thickness ratio (Figure A.3b). The final hatching distance of the vertical walls was doubled from 0.05 µm to 0.1 µm and the number of hatched lines was halved to 6 to reduce the printing time without noticeably changing the DC or vertical wall dimensions. This process resulted in the final writing parameters: 16 mW P for octet walls, 12 mW P, 6 hatched lines and 0.1 µm hd for vertical cubic walls, and 15.25 mW P and 0.05 µm hd for horizontal cubic walls. The resulting polymer wall thicknesses of the octet and cubic walls were 0.59 µm and 1.01 µm, respectively. The Raman spectra of Figure A.3d and Table A.1 show excellent overlap, indicating that identical microstructures were obtained for all wall directions using the final writing parameters.

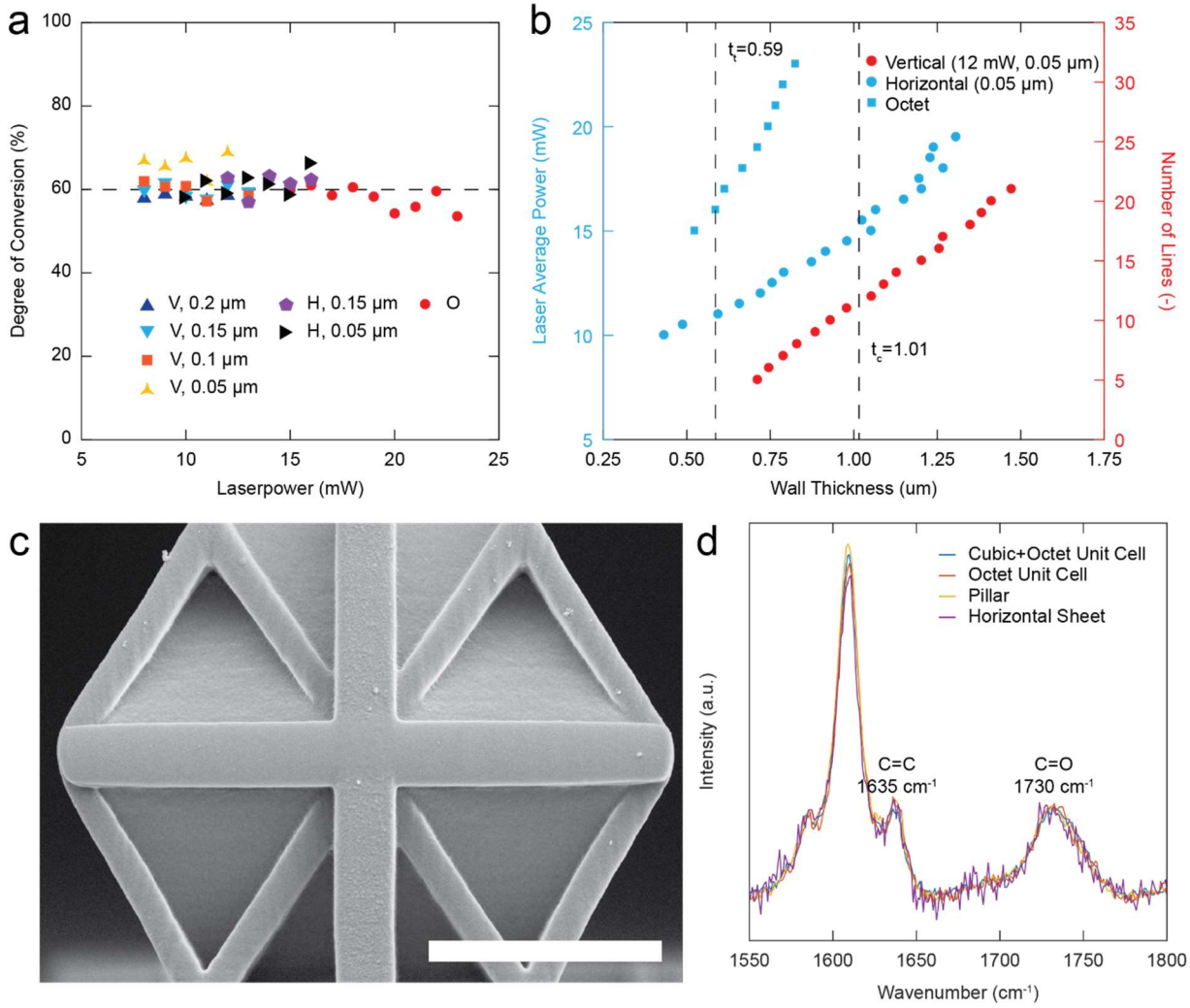

Figure A.3. *Writing parameter optimization encompassing degree of conversion and wall thicknesses measurements of individual plate orientations to produce high surface quality plate-nanolattices with isotropic constituent material and correct cubic-to-octet wall thickness ratio. Micro-Raman measurements of polymeric horizontal cubic (H), vertical cubic (V), and octet (O) plate orientations (a) show clustering of degree of conversion near 60%. Wall thickness calibration data controlled by laser average power (blue) or number of hatched lines (red) (b). Dashed lines indicate the chosen octet (t_t) and cubic (t_c) wall thicknesses. SEM micrograph of a wall thickness calibration structure (c) which was printed with a cut-open along the (110) plane shows walls have smooth surface finish. Scale bar is 5 µm. Raman spectra of polymeric cubic+octet and octet plate-lattice unit cells, pillar printed with the vertical wall parameters and single voxel-thick sheet printed with the horizontal wall parameters (d) show identical degree of conversion.*

Lastly, the polymeric structures had to accommodate the extreme shrinkage of pyrolysis with minimal surface deformations. As introduced in previous work[6], pre-pyrolysis TPP-DLW-printed polymer cubic+octet plate-microlattices were supported atop springs attached to pillars to decouple them from the substrate (Figure A.4). However, shrinkage during pyrolysis of polymers notably increases with increasing surface area and decreasing size. Compared to previously reported beam-lattices, the considerably larger plate-lattice dimensions exacerbated the shrinkage mismatch between support pillar and lattice. We developed a coarse pillar hatching strategy which introduced porosity into the support pillars reducing this mismatch to about 7%. Uniform shrinkage of the porous round pillars was ensured by rotating adjacent sliced layers by 30° from one another in a clockwise fashion as TPP-DLW lines tend to shrink along the writing direction. The aspect ratio of the support pillar, 0.85, was optimized to ensure a flat post-pyrolysis pillar top surface. Support pillar optimization in conjunction with carefully selected spring locations and dimensions reduced deformation during pyrolysis to a minimum.

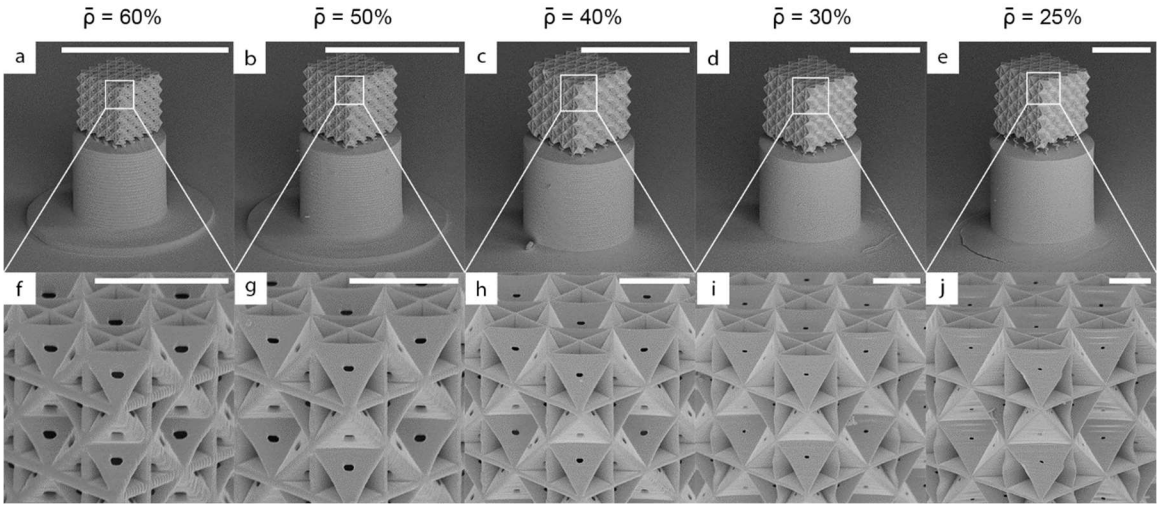

Figure A.4. *SEM micrographs of pre-pyrolysis polymer plate-nanolattices show near perfect lattices. Pre-pyrolysis polymer lattices are suspended atop pillars by coiled springs (a-b). Close ups of the unit cells (f-k) show that walls begin to warp slightly below* $\bar{\rho} = 30\%$*, but are otherwise perfect. Scale bars are 100 µm (a-e) and 5 µm (f-k).*

Raman spectra were also collected from pyrolytic carbon pillars, printed with the writing parameters of the vertical cubic walls, and plate-nanolattices. The degree of graphitization of the pillars and plate-nanolattices appear identical in Figure A.5 and Table A.2. Therefore, the constituent material of both has identical microstructures and thus mechanical properties.

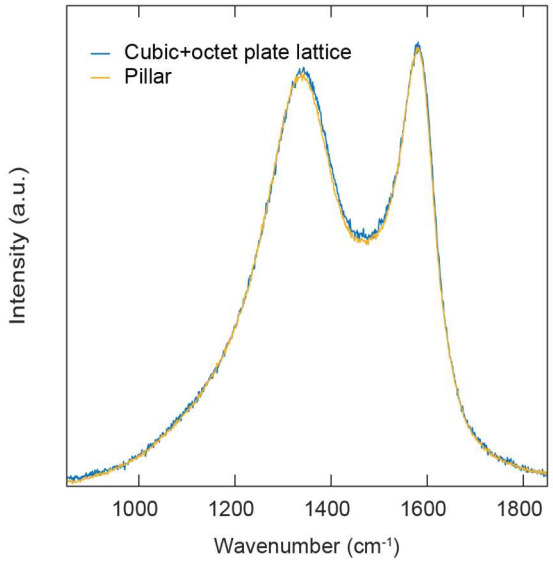

Figure A.5. *Raman spectra of pyrolytic carbon cubic+octet plate-nanolattices and micro-pillars indicate identical degree of graphitization and hence identical microstructures.*

Table A.1. *Raman spectroscopy results of polymer structures*

Structure	C=C (1635 cm^{-1})		C=O (1730 cm^{-1})		
	Peak Intensity (a.u.)	**Fit Error (%)**	**Peak Intensity (a.u.)**	**Fit Error (%)**	**Degree of Conversion (%)**
Cubic+octet plate-nanolattice unit cell	20500	3.68	47750	5.47	59.95
Octet plate-nanolattice unit cell	79740	2.16	191300	4.69	61.04
Square pillar (vertical cubic wall)	311400	2.31	680300	3.94	57.22
Single voxel thick sheet (horizontal cubic wall)	34480	3.31	78230	9.11	58.81

Table A.2. *Raman spectroscopy results of pyrolytic carbon structures*

Structure	R2		Half-width-half-max (HWHM) of D1	
	Average (-)	**Relative Standard Deviation (%)**	**Average (-)**	**Relative Standard Deviation (%)**
Cubic+octet plate-nanolattices	0.80	5.7	104.57	9.2
Micro-pillars	0.83	3.6	110.42	6.7

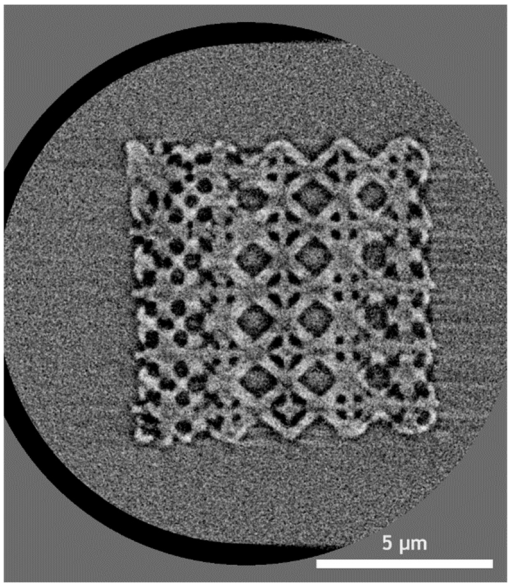

Figure A.6. *Nano-CT scan of cubic+octet plate-nanolattice with a relative density of 60%*

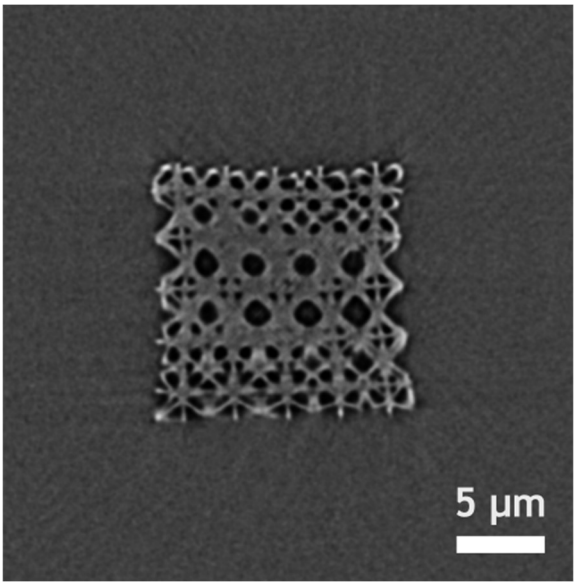

Figure A.7. *Nano-CT scan of cubic+octet plate-nanolattice with a relative density of 40%*

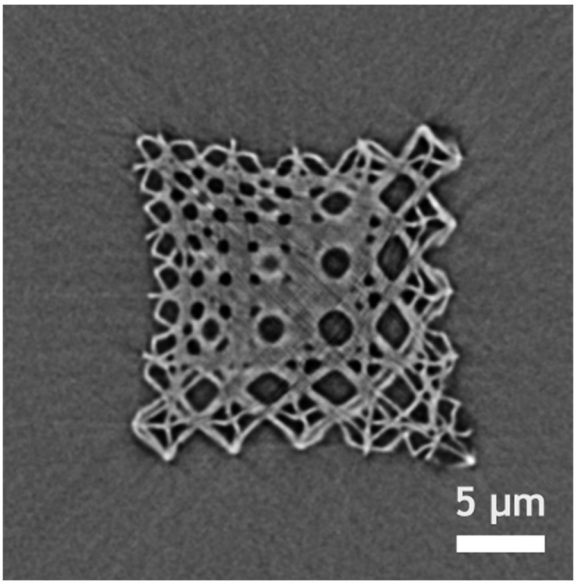

Figure A.8. *Nano-CT scan of cubic+octet plate-nanolattice with a relative density of 30%*

Table A.3. *Measurement parameters used in the X-ray microscopy CT experiments*

Sample Relative Density	**Projection exposure time (s)**	**Field of view ***	**Voxel size**
60%	100	HRES (16 μm^3)	16 nm

40%	60	LFOV (64 μm^3)	64 nm
30%	60	LFOV (64 μm^3)	64 nm

HRES: High resolution mode

LFOV: Large field of view mode

Appendix B. Experimental Characterization of Pyrolytic Carbon Plate-Nanolattices

To determine the constituent material properties of our plate-nanolattices a total of 8 circular pyrolytic carbon micro-pillars were *in situ* mechanically tested in uniaxial compression under identical conditions as the cubic+octet plate-nanolattices, i.e., using a loading-unloading cycle at 7% strain (Figure B.1). Considering the process parameter dependency[70] of TPP-DLW-derived structures, the same printing strategy of the vertical cubic walls of the plate-nanolattices was used to print the micro-pillars to most closely match the actual constituent properties. To reliably correct for substrate and system compliance via digital image correlation (DIC) and to reduce surface roughness due to the unidirectional hatching of the circular pillars, diameters of 6 μm were chosen. An aspect ratio of 3 between the height and diameter[157] was used. Stiffnesses and yield strengths between 37 and 44 GPa and 2.2 and 2.7 GPa, respectively, were determined from DIC corrected stress-strain curves. Post-yield buckling prevented maximum compressive strength measurement, however maximum stresses were on the order of reported compressive strengths[55] of TPP-DLW-derived pyrolytic carbon.

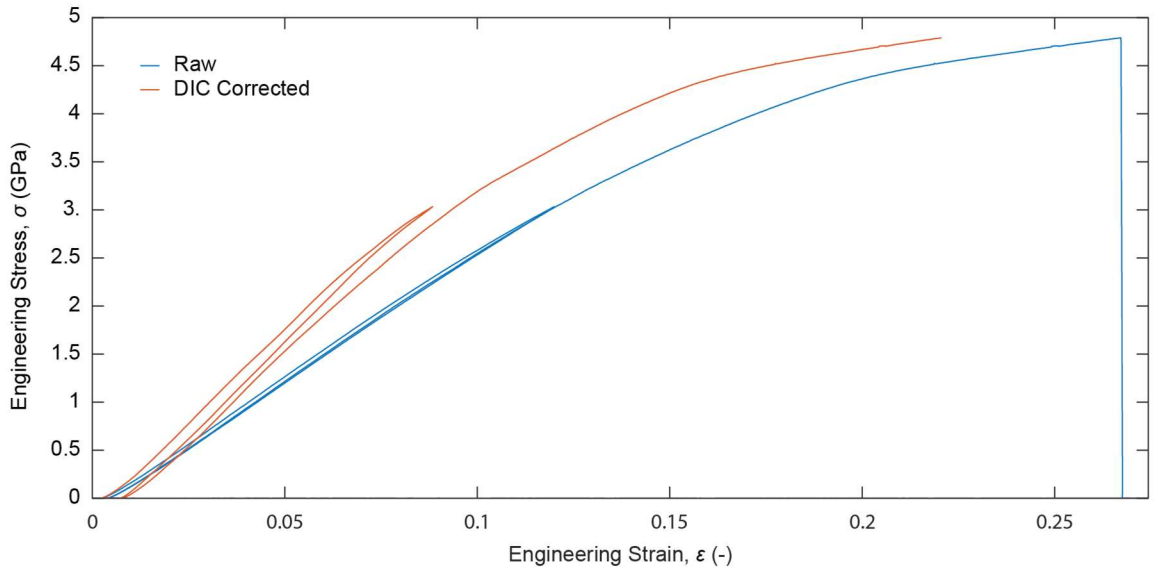

Figure B.1. *Compression experiment of pyrolytic carbon micro-pillar. As measured, raw, and digital image correlation (DIC) corrected compressive stress strain curves.*

Figure B.2 shows the strain at failure of our plate-nanolattices, which undergo elastic-plastic deformation ($\bar{\rho} \geq 37.5\%$), decomposed into their elastic and plastic components. The highest relative density plate-nanolattice ($\bar{\rho} = 57.5\%$) had a failure strain of approximately 21.9%, comparable to pyrolytic carbon nanoarchitectures of the same relative density[6,14,69]. As reported for many brittle beam-lattices[12–14], we found the failure strain of plate-nanolattices with relative densities above 37.5% to decrease with decreasing $\bar{\rho}$. Given that stiffness and yield strength both scaled nearly linearly with density, the yield strain was independent of $\bar{\rho}$. Deformation until failure was predominantly elastic. Finite element analysis (Figure 2.5) indicated that the failure strain-relative density dependency is related to post-yield buckling. Given that pyrolytic carbon at this scale only shows a modest change in stiffness between elastic and plastic deformation, the elastic buckling simulations well approximate the plastic buckling strength. In good agreement with the measured compressive strength, the computed buckling strength exceeds the yield strength above $\bar{\rho} = 37.5\%$ and rapidly increases with $\bar{\rho}$. Simultaneously, the failure strain increases, causing the found dependency with $\bar{\rho}$. At low relative densities ($\bar{\rho} < 37.5\%$), where structures fail in a layer-by-layer fashion, meaningful failure strains may not be defined, because structures can be

progressively deformed until densification. Compression experiments were terminated after failure of the first unit cell layer in our experiments.

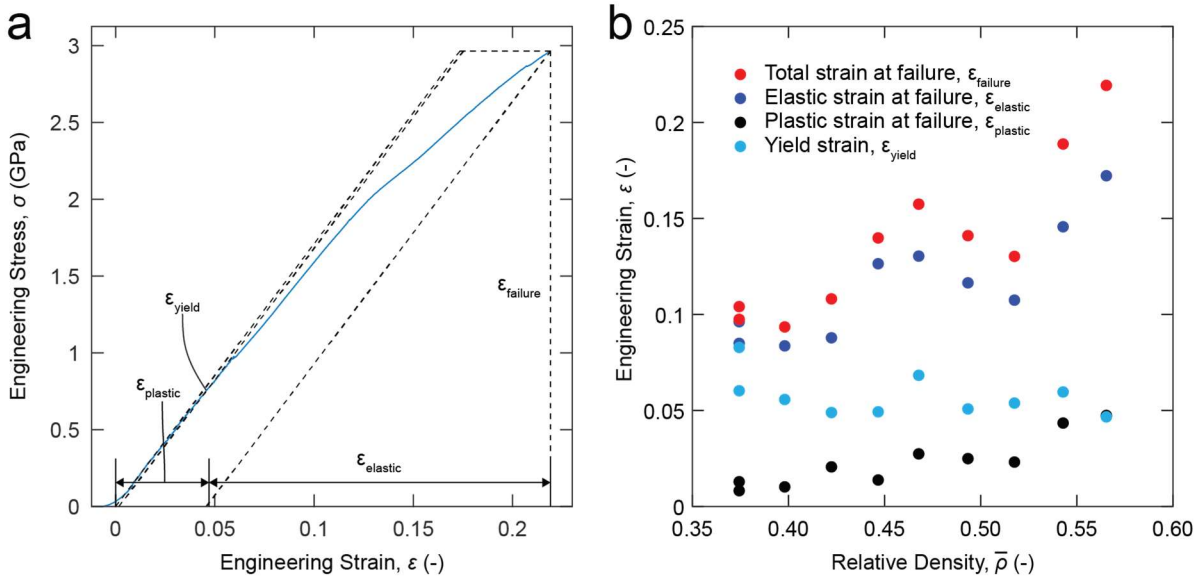

Figure B.2. *Failure strains of high-$\bar{\rho}$ pyrolytic carbon cubic+octet plate-nanolattices are predominantly elastic and decrease with decreasing relative density. Digital image corrected stress-strain response of the $\bar{\rho} = 57.5\%$ specimen with strain components (a). Strain components at failure depending on the relative density (b).*

Figure B.3 shows Ashby charts of stiffness and strength, which are normalized by the constituent material properties. Unfortunately, it is often challenging to extract reliable constituent material properties of architected materials from literature, particularly in the case of micro- and nano-architected structures exploiting size-effect strengthening, which represent the vast majority of architected materials. Hence, in order to provide meaningful comparisons, we only report data for TPP-DLW-derived pyrolytic carbon architectures. While limited to a single material system, the topologies we present nevertheless include the most relevant beam-architectures, like octet and isotropic trusses, as well as shell spinodal topologies. The cubic+octet topology of our plate-nanolattices can clearly be seen to outperform all other available architectures in both strength and stiffness. Absolute strength, stiffness and density values were normalized by 7 GPa, 62 GPa and 1.4 g/cm³, respectively.

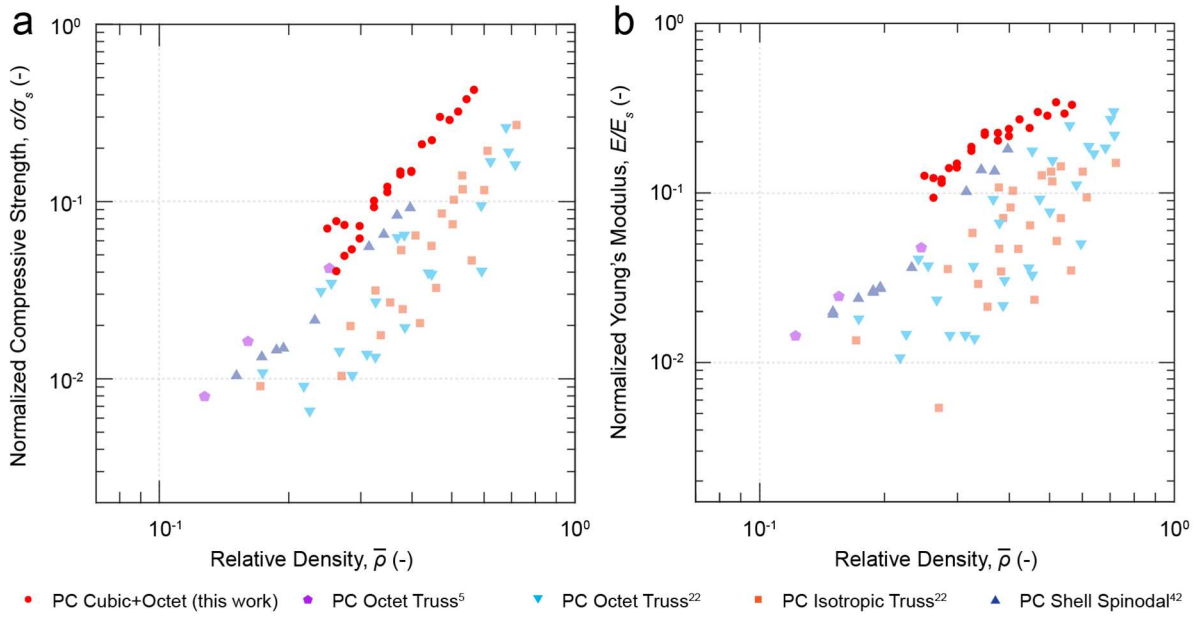

Figure B.3. *Normalized Ashby charts comparing the cubic+octet plate-architecture to beam and shell topologies in strength (a) and stiffness (b).*

Table B.1. *Scaling relations of effective yield strength and stiffness versus relative density of the respective forms* $E = BE_s\bar{\rho}^b$ *and* $\sigma_y = C\sigma_{y,s}\bar{\rho}^c$ *given the effective Young's modulus (E) and yield strength (*σ_y*), the constituent material's Young's modulus (*E_s*) and yield strength (*$\sigma_{y,s}$*), the geometric parameters (B and C), the scaling exponents (b and c), and the relative density (*$\bar{\rho}$*).*

Sample Range	$\boldsymbol{BE_s}$**(GPa)**	$\boldsymbol{b}$	$\boldsymbol{C\sigma_{y,s}}$ **(GPa)**	$\boldsymbol{c}$
$\bar{\rho} < 37.5\%$)	140.2	2.22	11.4	2.78
$\bar{\rho} \geq 37.5\%$)	38.8	1.05	1.7	0.85

Appendix C. Computational Modeling of Cubic+Octet Plate-Lattices

To account for uncertainty in the Poisson's ratio of nanoscale pyrolytic carbon, finite element computations were performed with Poisson's ratios of 0.17[72] and 0.3[44]. No significant change was observed in the results of the normalized Young's Modulus or Zener anisotropy ratio, as shown in Figure C.1.

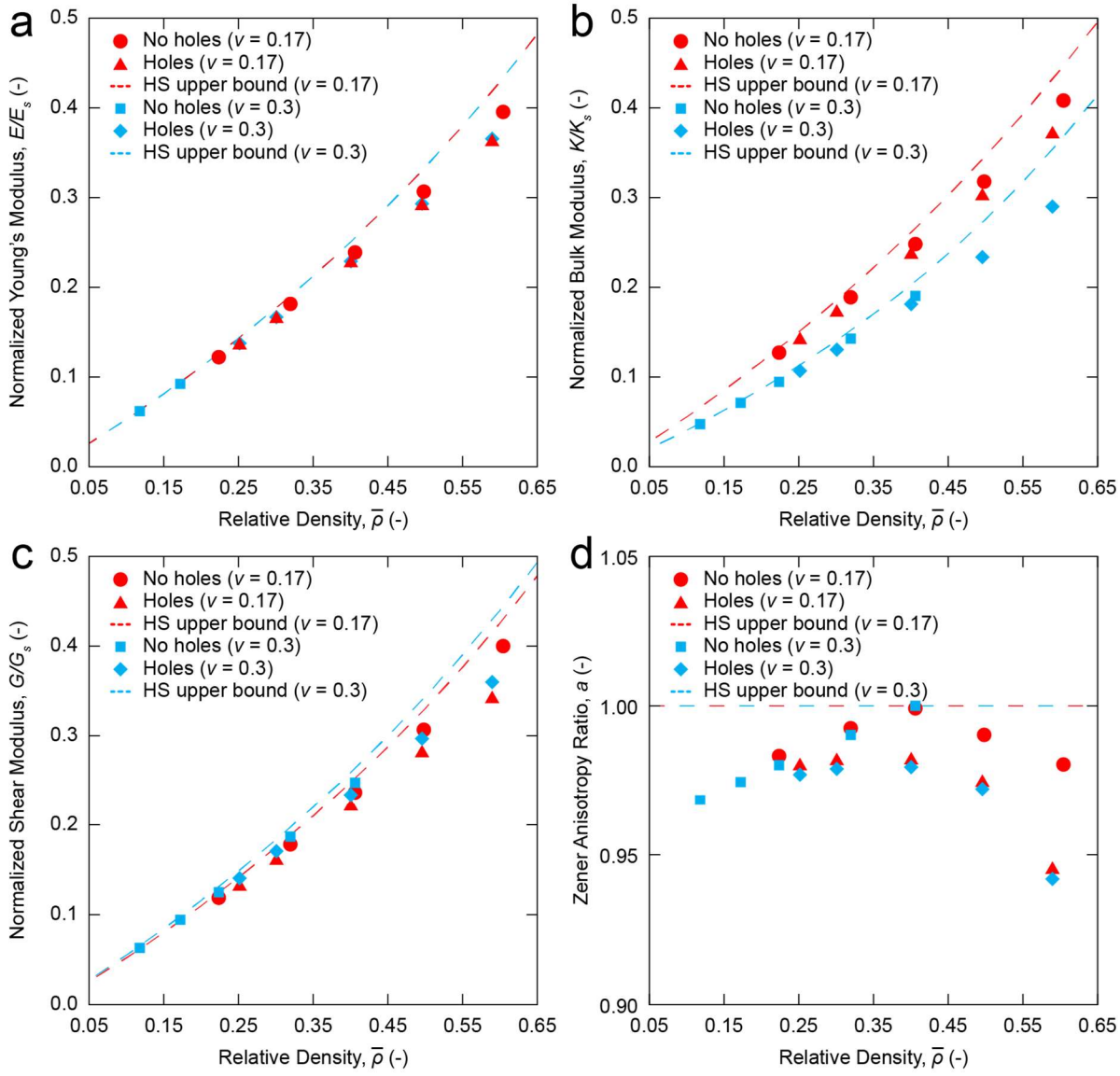

Figure C.1. *Finite element analysis of cubic+octet plate-lattice performance, for two values of the Poisson's ratio, v = 0.17 and 0.3. Normalized Young's modulus (a), normalized bulk modulus (b), normalized shear modulus (c), and Zener anisotropy ratio (d) versus relative density ($\bar{\rho}$) for models with and without holes. Lines, denoting the Hashin-Shtrikman (HS) upper bound, and points in red and blue represent simulations performed with 0.17 and 0.3, respectively, and show that independent from v, holes induce no significant knockdown on the Young's modulus or Zener anisotropy ratio, despite noticeable effects on the shear and bulk moduli.*

Figure C.2 shows the computed mechanical properties of shell and solid models of ideal plate-lattices do not differ noticeably for most of the investigated relative density range. Simulations with pre-deformed low-$\bar{\rho}$ models and eigenmode analysis to determine the buckling strengths shown in Figure 2.6 were carried out with shell models. Furthermore, the holes do not significantly alter the buckling strength of ideal shell model plate-lattices below $\bar{\rho} = 50\%$ (Figure C.2b).

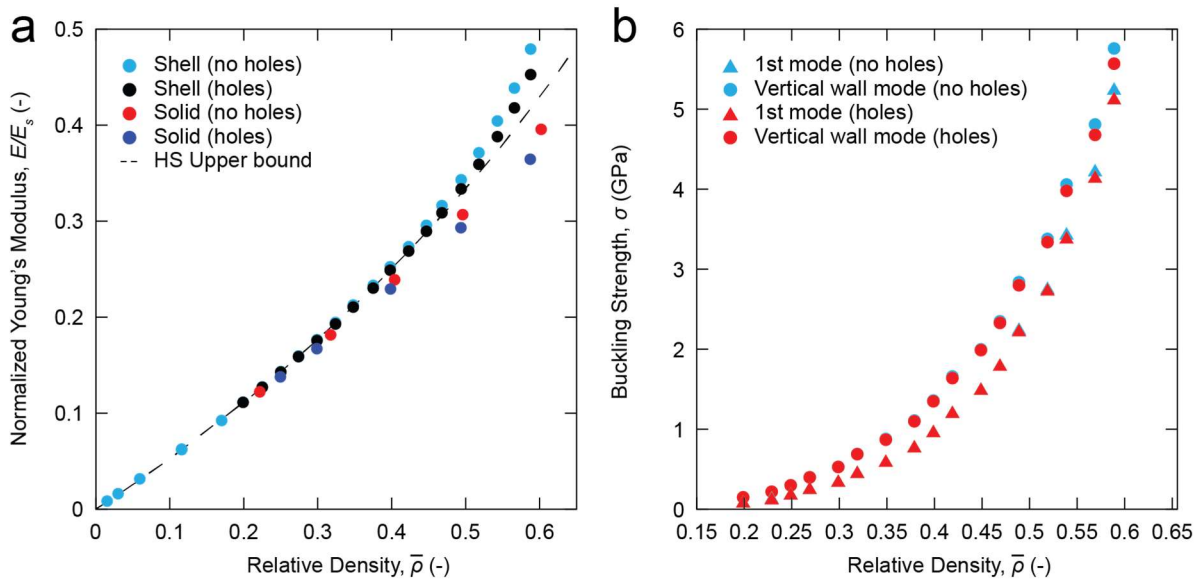

Figure C.2. *Ideal shell and solid models provide nearly identical results simulating plate-lattices with and without holes up to $\bar{\rho} = 40\%$ (a) and holes do not significantly change the simulated buckling strength of shell model plate-lattices below $\bar{\rho} = 50\%$ (b).*

Appendix D. Nonlinear Least Square Fitting Procedure to Approximate the Constituent Material Stiffness of Pyrolytic Carbon Cubic+Octet Plate-Nanolattices with Face Holes

The theoretical upper bound for the Young's modulus of an isotropic cellular material (the Hashin-Shtrikman bound[27]) is given by:

$$\bar{E}_{HSU} = \frac{E_{HSU}}{E_s} = \frac{2\bar{\rho}(5\nu - 7)}{13\bar{\rho} + 12\nu - 2\bar{\rho}\nu - 15\bar{\rho}\nu^2 + 15\nu^2 - 27} \tag{D.1}$$

with the Young's modulus (E_s), Poisson's ratio (ν) of the constituent material, and the relative density ($\bar{\rho}$). The cubic+octet plate-nanolattices of this study included face holes to allow trapped monomer to escape during development. Although small, the holes included a certain knockdown to the stiffness. To account for the contributions of the face holes (see Figure 2.1), we calculate a correction function (C_C) by least squares fitting the normalized Young's moduli of the finite element plate-lattice data from Figure 2 to the equation:

$$\frac{E_{CO}}{E_s} = C_C \bar{E}_{HSU} \tag{D.2}$$

where E_{CO} is the effective Young's modulus of the cubic+octet plate-lattice with face holes and the correction function is taken as:

$$C_C = C_1\bar{\rho}^3 + C_2\bar{\rho}^2 - (C_1 + C_2)\bar{\rho} + 1 \tag{D.3}$$

with the fit parameters C_1 and C_2. As the Poisson's ratio of the constituent material does not have a noticeable effect on the Young's modulus of the lattice (Figure C.1), it is not considered in C_C. The correction expression is a cubic polynomial subject to the boundary conditions $C_C = 1$ at $\bar{\rho} = 0$ and $\bar{\rho} = 1$ given that for relative densities of 0% and 100%, e.g., a solid cube, the effective Young's modulus must be 0 and that of the constituent material, respectively. The fitted parameters are therefore found to be $C_1 = 0.92$ and $C_2 = -0.94$. By fitting the following equation with the aforementioned values of C_1 and C_2 and E_s as the only varying fit parameter on the experimentally measured Young's moduli for the plate-nanolattices at $\bar{\rho} \geq 37.5\%$ from Figure 4:

$$E_{CO} = E_s C_{knockdown} \bar{E}_{HSU} \tag{D.4}$$

we extract an effective constituent Young's modulus (E_s) of 62 GPa, in excellent agreement with literature data[51].

Appendix E. Polymeric Cubic+Octet Plate-Microlattices

To investigate the influence of manufacturing-induced plate curvature on the mechanical behavior of low relative density pyrolytic carbon plate-nanolattices, we fabricated and characterized polymeric cubic+octet plate-microlattices with near-ideal, undeformed geometries, complementing our pre-deformed pyrolytic carbon structures (Figure E.1). Low relative density pyrolytic carbon structures ($\bar{\rho} < 37.5\%$) incurred notable surface deformations during pyrolysis, which were consistent with progressive failure behavior. Here we want to understand whether these imperfections are essential for plate-lattices to manifest progressive failure behavior. The writing parameters of the polymeric plate-microlattices were 25 mW *P* for octet walls, 15 mW *P*, 25 hatched lines and 0.05 µm *hd* for vertical cubic walls, and 23.5 mW *P* and 0.05 µm *hd* for horizontal cubic walls.

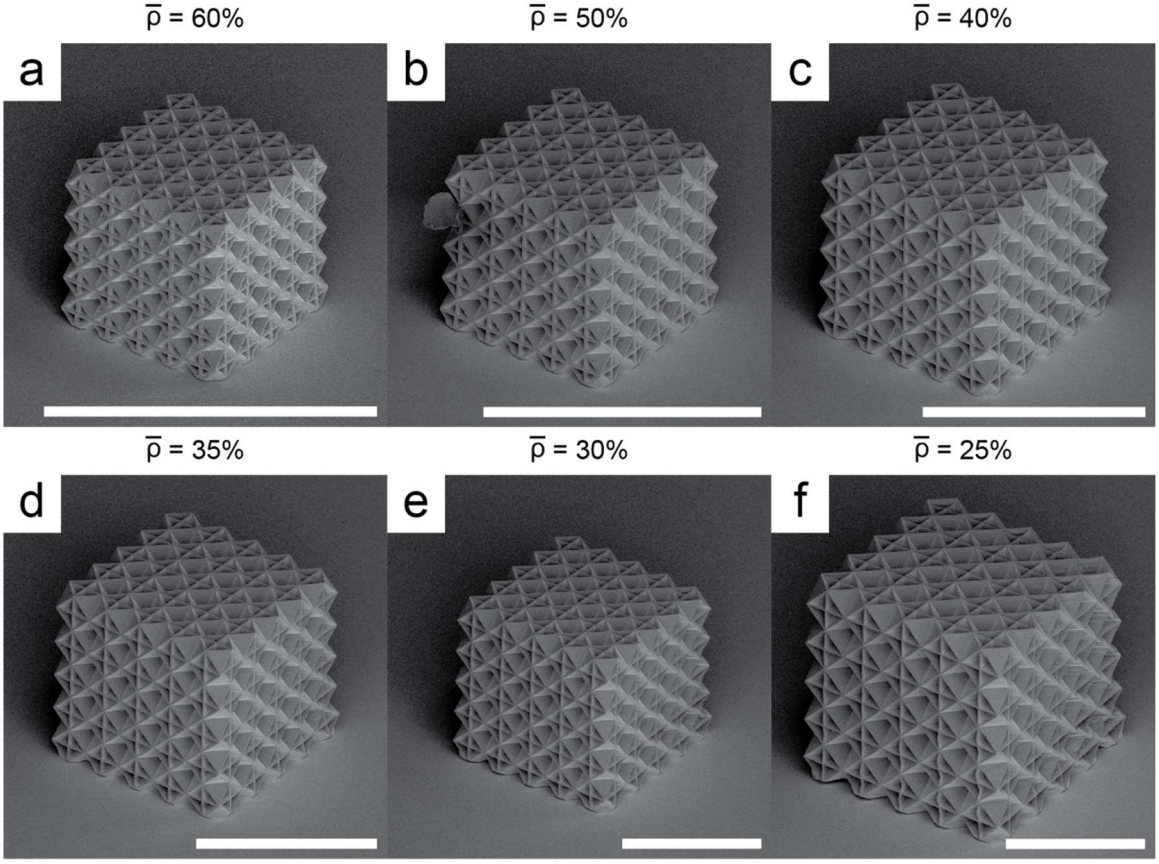

Figure E.1. *Polymeric plate-microlattices fabricated via TPP-DLW with geometric defect free topologies down to relative densities ($\bar{\rho}$) of 25%. Scale bars are 100 µm.*

As in pyrolytic carbon plate-nanolattices, the stress-strain curves of polymer plate-microlattices exhibited a transition from brittle to progressive failure with decreasing relative density (Figure E.2). Failure in the highest relative density polymer structures ($\bar{\rho} > 40\%$) was catastrophic but became progressive at relative densities of 40% and below, where layer-by layer failure was preceded by buckling of vertical wall members. Except for the lowest relative density polymer lattice ($\bar{\rho} < 25\%$,) whose vertical wall members slightly warped during fabrication, buckling was not observed prior to yielding. As for the pyrolytic carbon, polymeric structures were loaded in two cycles where the initial loading and unloading at ~3-4% strain, prior to significant nonlinear behavior, ensured accurate stiffness measurement. Note that the polymeric lattice of relative density 50% was not tested to failure due to an instrument error. These results

show that manufacturing or design-induced pre-curvature of the plate elements is not essential to exhibit progressive failure as long as elastic or plastic buckling can induce sufficient plate curvature preventing catastrophic crack propagation through the entire structure and hence brittle failure[69].

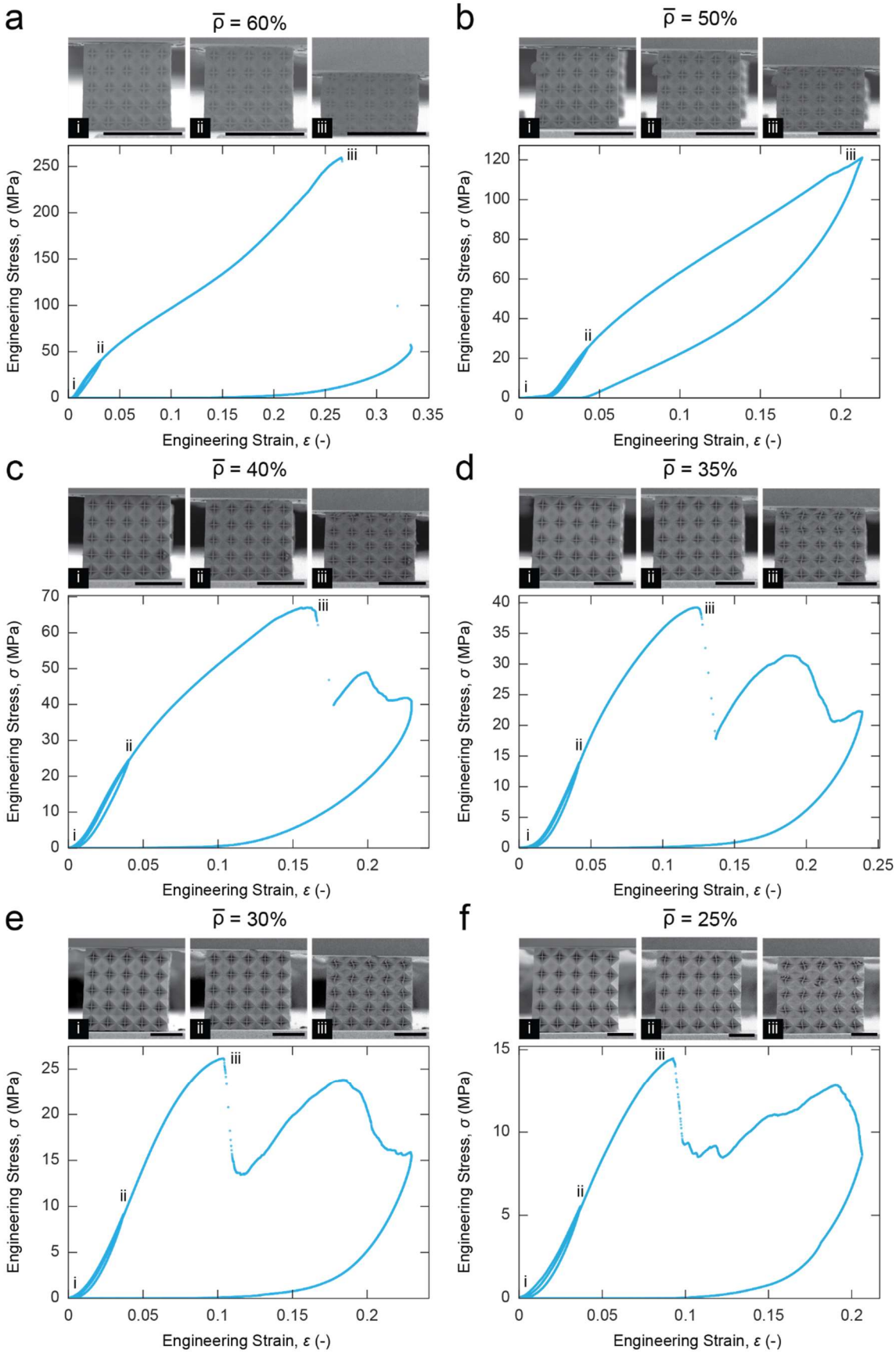
a
$\bar{\rho}$ = 60%
i
ii
iii
Engineering Stress, σ (MPa)
Engineering Strain, ε (-)
b
$\bar{\rho}$ = 50%
c
$\bar{\rho}$ = 40%
d
$\bar{\rho}$ = 35%
e
$\bar{\rho}$ = 30%
f
$\bar{\rho}$ = 25%

Figure E.2. *Compression experiments of polymeric cubic+octet plate-microlattices with different relative densities ($\bar{\rho}$). Stress-strain curves of specimens with $\bar{\rho}$ from 60% to 25% (a-f) accompanied by front facing in situ SEM images at labeled locations (i, ii, and iii), show transitions from brittle fracture to progressive deformation behavior around 40% relative density. Scale bars are 50 μm.*

All polymeric lattices lie at the Suquet upper bound for strength (Figure E.3) except for the lowest relative density sample ($\bar{\rho} = 25\%$), which failed by elastic buckling prior to yielding. Although the constituent polymer material is brittle, measurement challenges related to the viscoelastic nature of the material resulted in drastic knockdowns to the measured stiffness with respect to the Hashin-Shtrikman upper bound[42]. Nonetheless, the stiffness data reflects a clear trend with minimal scatter due to the higher geometric fidelity of the polymer plate-microlattices compared to the pyrolytic carbon ones. Both stiffness and strength did not show a knockdown over the transition from brittle to progressive failure. The shaded regions in Figure E.3 are enclosed by the upper bounds for stiffness and strength of a constituent material with the minimum and maximum constituent material properties of the polymer, as measured from uniaxial compression of five aspect ratio 3 square pillars with a side length of 20 μm and printed using the vertical cubic wall writing parameters. Viscoelastic polymer properties are sensitive to environmental conditions and measurements showed higher variability than found for pyrolytic carbon. The average polymer Young's modulus and 0.2% offset yield strength were 6.0±2.0 GPa and 67±19 MPa, respectively, whereby higher values may be expected to best represent the constituent properties of the structures.

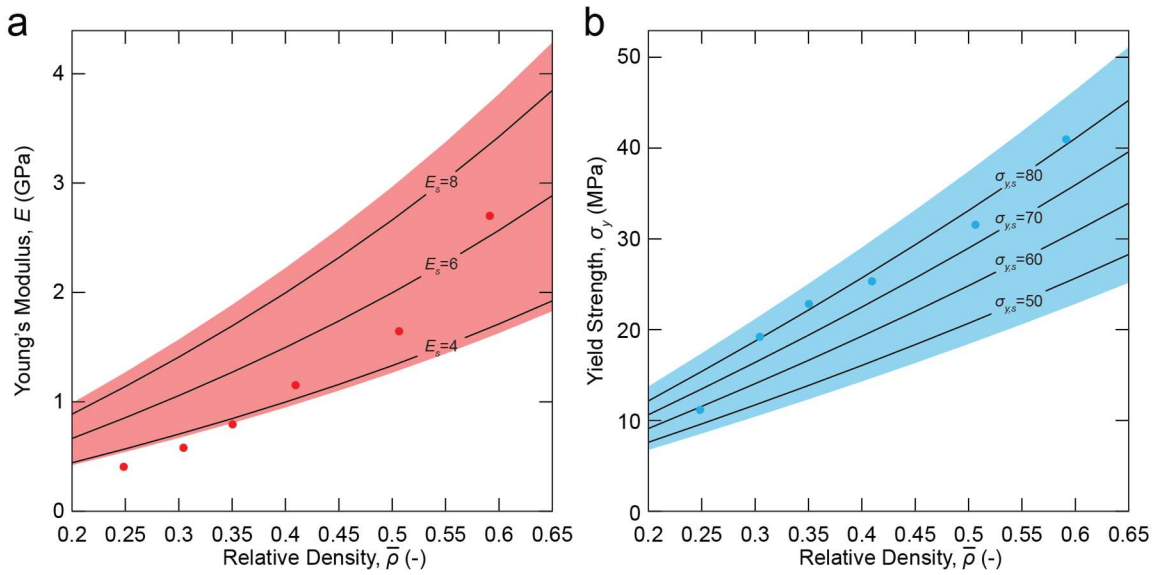

Figure E.3. *Polymeric cubic+octet plate-microlattices reach the Suquet upper bound for strength of an isotropic cellular material. Stiffness (a) and yield strength (b) versus relative density plots show most data points within the shaded upper bound regions, which are given by the constituent property range of the polymer. Lines (black) indicate upper bound functions for various constituent materials properties.*